Perspectives in Adsorptive and Catalytic Mitigations of NOx Using Metal–Organic Frameworks

Karim Adil, Katarzyna Świrk, Abdelali Zaki, Ayalew Assen, Gérard Delahay, Youssef Belmabkhout, Amandine Cadiau

Perspectives in Adsorptive and Catalytic Mitigations of NO_x Using Metal–Organic Frameworks

Karim Adil[ab]*, Katarzyna Świrk[a], Abdelali Zaki[a], Ayalew H. Assen[c], Gérard Delahay[a], Youssef Belmabkhout[c], and Amandine Cadiau[a]

[a] Université de Montpellier, Institut Charles Gerhardt de Montpellier (UMR 5253), 34095 Montpellier, France;

[b]Le Mans Université, Institut des Molécules et des Matériaux du Mans (UMR 6283), 72085 Le Mans, Cedex 09, France; Email: karim.adil@univ-lemans.fr

[c]Technology Development Cell, Mohamed VI Polytechnic University (UM6P), 43150 Ben Guerir, Morocco

ABSTRACT: Because of its high polluting effect, a growing research interest in NO_x monitoring, removal, and control has been noticed in the last years. Motivated by the high degree of functional and structural tunability of metal− organic frameworks (MOFs), researchers explored potential MOF-based adsorbents, sensors, and catalysts for NO_x mitigation/control. However, this area of research is still in its infancy. In addition, the physical−chemical properties of NO_x make this task extremely challenging as some materials suffer relatively weak thermal and/or chemical stability. Nevertheless, some recent encouraging studies have demonstrated superior stability properties that enable MOFs to be considered as alternative benchmark materials for the capture and conversion of NO_x. This review offers an overview on the recent progress made in this field and provides some interesting routes on the uses of MOFs for selective NO_x adsorption, release, and/or catalytic conversion (via selective catalytic reduction or photocatalysis).

1. INTRODUCTION

Nitric oxide (NO) and nitrogen dioxide (NO_2) are ambient trace gases that result from both natural and anthropogenic processes. Thus, above the natural level in air, these gases, even at trace levels, are considered harmful pollutants. The continuous strong increase of these biologically active nitrogen compounds is mainly due to human activities in both industrial and agricultural sectors, thereby disturbing the natural nitrogen cycle. In particular, the major sources of anthropogenic emissions of nitrogen oxides (NO_x) are coming from the combustion processes either from stationary or mobile sources (power generation,

internal combustion engines in vehicles, as well as from biomass burning) where ambient air is used for combustion processes.

Nitrogen-containing air pollutants can affect vegetation, either indirectly via chemical reactions in the atmosphere or directly after being deposited on vegetation, soil, or water, and are harmful for humans. In 2016, more than 550,000 deaths were attributed to outdoor and indoor air pollution in Europe according to the WHO (World Health Organization). It causes growth and pulmonary function slowdown, respiratory infections, and exacerbates asthma in children, while adults are affected by ischemic heart disease and strokes.

Specifically, NO in most ambient situations is rapidly transformed into NO_2 by atmospheric oxidant. This nitrogen dioxide (NO_2) is one of the most concerning pollutants for public health and presents in air at the same level as particles,

ozone, and sulfur dioxide (SO_2). This reddish-brown gas is a strong oxidant that reacts with water to produce nitric acid and nitric oxide. NO_2 has not only a direct negative effect on our health but is also a key precursor of a range of secondary pollutants which influence the global tropospheric chemistry and become the main causes of greenhouse effects, acid rain, photochemical smog, and particle matter.[1]

The effects of nitrogen dioxide on human health are summarized in the second edition of air quality guidelines and include respiratory symptoms such as bronchoconstriction, increased bronchial reactivity, airway inflammation, and decreased immune defense. All these conditions lead to increased susceptibility to respiratory infection. It is worth mentioning that NO_2 emission recommendations are 200 μg/ m_3 at 1 h average and 40 μg/m_3 annual average.

Because of the wide range of side effects due to trace NO_x exposure, governments all around the world took actions with strict legislations and policies to control their emissions. In the last years, the United States decided to regulate NO_x emissions with imposed rate limits of 553.5 and 615 mg/m_3 for tangentially fired boilers and dry bottom wall fired boilers, respectively.[2] China has also applied strict emission standards with

a limit of 100 mg/m3 for new power plants and natural gas-fired boilers and 50 mg/m3 for natural gas-fired turbines.[3] Moreover, the limits of NO_x at 60 and 35 mg/km for light-duty vehicles in China will be implemented in 2020 and 2023, respectively.[4]

Due to the low concentration of NO_x pollutants in air (ppb level) along with the highly toxic potentials, their mitigation is becoming of prime importance. Consequently, the development of materials with adapted sensitivity/selectivity but also fast response toward these pollutants is an intense ongoing research field. Researchers are focusing their efforts on the fabrication of new selective sensing/scrubbing materials with abilities to adsorb these targeted toxic gases onto their surface and then generate a signal for detection/removal. Porous adsorbents are materials of choice for the capture of such molecules based on a physisorption or chemisorption mechanism.[5] It is important to note that the adsorption capacity of a porous adsorbent is affected by its pore volume (physisorption), where the chemical adsorption capacity is mainly dependent on the surface functionality. In fact, the complex interplay of these parameters has a direct relationship with the selective adsorptive/diffusion/ catalytic performances. The signal transduction is correlated to optical (vapochromism, luminescence, interferometry, localized surface plasmon resonance), mechanical (quartz crystal micro- balance (QCM), surface acoustic wave sensors (SAWS), microcantilevers (MCL)), or electrical properties, resulting from the interaction between the surface of the sensors and the pollutant.[6] A few recent papers and reviews are dedicated to the particular sensing of NO_x, so we encourage the reader to refer to them.[1,7–9]

The main challenge associated with the capture and detection of these toxic gases is mainly attributed to their very low concentration in air. Consequently, the looked-for adsorbent has to be highly selective and able to detect them in very low ranges of concentration. Another aspect that is of prime importance is the ability of chemical sensors to be highly robust toward these toxic gases to avoid affecting the materials by the corrosive nature of NO_x. Few literature reports discuss the capture of toxic gases through porous materials from a molecular simulation point of view. The computational approach allows researchers to avoid

the experimental constraints related to security and/or material degradation.[10,11] It is important to note that nitrogen oxide is recognized as a harmful gas, meanwhile its ability to serve in medical applications is well known and discussed in different recent scientific reviews.[12−16]

Finally, once NO_x has been detected and captured, the next challenging step is associated with a process of degradation employing a catalytic conversion to harmless gas. Currently, $DeNO_x$ technologies such as selective noncatalytic reduction (SNCR), nonselective catalytic reduction (NSCR), and selective catalytic reduction (SCR) have been proposed. Other processes such as sulfate radical ($SO_4^{\bullet-}$)-based advanced oxidation technologies (AOTs),[17] liquid oxidation and absorption technologies,[18] and nonthermal plasma remediation technologies[19] may be used. One could refer to the recent review by Yang et al.[20] for discussions on the $DeNO_x$ methods such as SCR, SNCR, adsorption, storage reduction, and especially on direct catalytic decomposition of NO using catalysts involving noble metals, metal oxides, perovskite-type composite oxide, hydrotalcite materials, heteropoly acid, and Cu-ZSM-5. Various NO reduction chemical absorption systems have also been explored by different researchers using absorbents including Fe(II)EDTA,[21,22] Fe(II) thiochelates, and 1,3-dimethylthiour- ea-derived eutectic solvents.[23,24] More specifically, abatement of NO_x using SCR with ammonia is the most developed process because of its cost saving and efficiency in the presence of other competitive gases such as O_2, H_2O, and SO_2.[25−27]

Three types of catalyst have been developed and are commercially used: noble metal-based catalyst, mixed oxides (V_2O_5/TiO_2), and zeolites. Owing to their relatively lower cost and redox property, cerium-based oxides, both as single CeO_x or multimetallic oxides, are among the most explored low- temperature NH_3-SCR catalysts for NO_x.[28] It should be noted that many drawbacks associated with these catalysts were unveiled, such as quick deactivation by poisoning, low selectivity, and low specific surface area. Liquid or dry gas phase homogeneous/heterogeneous Fenton(-like)-based sys- tems such as ultraviolet (UV) light and heat-coactivated oxone (potassium peroxymonosulfate), Fe^{2+}/H_2O_2, in situ Fenton ($Fe^{2+}/H_2O_2/M^{n+}$) (M = Ce^{3+}, Co^{2+}, Cu^{2+}, Mn^{2+}), photo- Fenton ($UV/Fe^{2+}/H_2O_2$), gas-phase heterogeneous Fe/ZSM- $5/H_2O_2$, and

UV/S-doped TiO_2/H_2O_2 are also among the commonly investigated oxidation systems for removal of NO_x.[29−31] However, high deactivation rate and low catalytic activity are the major drawbacks of such systems. Further details on different types of oxidative adsorption systems that have been explored for NO_x removal are also summarized in the recent review by Liu et al.[32] Accordingly, researchers from both academia and industry are devoting important efforts to develop alternative solutions to ammonia using hydrocarbons or carbon monoxide as reducing agents following the reaction $2NO + 2CO \rightarrow N_2 + 4CO_2$. A plausible route to consider is the development of a new eco-friendly SCR catalyst with superior SO_2/water resistance, strong thermal stability, and good chemical tolerance associated with an operational low temperature (<300 °C). Evidently, other processes based on photocatalysis are also considered as an interesting route of exploration. To support these processes (sensing, capture, and NH_3-SCR catalysis), many materials have been tested, such as porous carbon, mixed oxide, or zeolites.[8,33] Nevertheless, poor selectivity, low efficiency combined with high energy consumption for regeneration are observed which strongly limit their practical use.

Metal−organic frameworks (MOFs) are a relatively new class of materials located at the forefront of solid-state materials. Intensive research activity in this field in the last two decades has demonstrated promises in many different areas of application, such as gas storage, gas separation, sensing, catalysis, water harvesting, and proton conduction, among other fields.[34,35] MOFs are defined as the connection using ionocovalent bonds between an inorganic part (isolated metal cation, cluster, or infinite chains) and organic linkers. The considerable diversity of linkers associated with all plausible metal nodes may lead to an almost infinite number of new MOF materials. The resulting MOFs are porous materials with pore sizes ranging from a few to tens of angstroms. It is important to note that investigations from many groups have demonstrated the plausible control of both the structures (topology) and pore sizes of MOFs and also their functionalization using judicious choices of organic linkers or introductions of cations/clusters with open metal sites (OMSs). As an example, fine-tuning the pore aperture size, which is of major interest in gas separation and capture, is now possible contrary to other inorganic solid adsorbents, such as zeolites, inorganic oxides, and porous

carbon-based materials. Overall, the versatile properties of MOFs make them highly competitive materials in many fields and, in particular, to address societal and environmental issues.[36,37,38−45,46−51,]

The use of MOFs as potential adsorbents, sensors, and catalysts for NO_x is still in its infancy because they are a relatively new class of solid-state materials. Some are suffering from drawbacks such as thermal and/or chemical stability, but recently some encouraging studies have demonstrated superior stability properties that enable MOFs to represent an alternative to benchmark materials for the capture and conversion of NO_x. Accordingly, a literature review summarizing the recent results obtained on this specific topic would be of high interest.[52] It is worth noting that some reviews are available for the field of detection and removal of toxic gases including ammonia, SO_2, H_2S, and NO_2,[8,53−56] and some others report the use of MOFs as catalysts.[57] However, to the best of our knowledge, there is no review related specifically to the specific adsorption and catalytic conversion of NO_x using MOFs. In 2015, Rezaei et al.[58] summarized some potential solid adsorbents such as zeolites, activated carbons, and MOFs for capturing SO_x/NO_x from flue gas streams. Since then, lots of research progress have been made in the development of advanced MOFs for NO_x capture as well as in the understanding of the adsorption mechanisms.

The first part of this review deals with MOFs as adsorbents for NO_x capture and more specifically for NO and NO_2 captures. The second part is devoted to MOFs as potential catalysts for NO_x degradation via selective SCR mainly using NH_3 or via photocatalysis. It is important to note that among available reviews dealing with catalysis of NO_x only a few of them mention the exploration of MOFs as potential catalysts.[59−62] Accord- ingly, this review focuses only on the use of MOF materials and eventually MOF composites, but excludes oxide materials prepared from MOFs precursors for applications, in NO_x adsorption and catalysis.[63,64]

2. NO FOR BIOLOGICAL APPLICATIONS

The large majority of investigations carried out on exploiting adsorptive capabilities of MOFs for NO have been performed with the objective of developing biological applications. Two main pathways have been explored. The first option is based either on the physisorption mechanism using porous materials and/or the

chemisorption process resulting from the reaction between NO and accessible open metal sites located on the inorganic part of the compound. The second option is the adsorption of NO onto an amine functional group that is grafted either on an open metal site or located on the ligand following a chemical reaction between the function present (i.e., amine) and the NO molecule to form the so-called NONOates.[65] The NO release in biological media is plausible upon contact with water that can replace NO and consequently offers a feasible control on the desorption process.

2.1. Physisorption/Chemisorption on Open Metal Sites (OMS). 2.1.1. MOFs Adsorbent for NO. To the best of our knowledge, the first investigation related to NO adsorption using MOF was carried out on the copper-benzene tricarbox- ylate (Cu-BTC) MOF, HKUST-1,[66] in 2007.[67] NO adsorption isotherms were collected at 196 and 298 K until 1 bar with capacities of ~9 and 3 mmol g^{-1}, respectively (Figure 1). It is important to note that the obtained gravimetric adsorption capacity of HKUST-1 was higher than any other uptake values reported using porous solids (e.g., zeolite, carbon) in the beginning of the 2000s. The recently published review by Huang et al.[68] on the removal of typical industrial gaseous pollutants (H_2S, NO_x, SO_2, VOCs) by adsorption on zeolite, carbon materials, and MOFs confirms this high ability to adsorb but also to release NO_x at moderate temperature, compared to other materials. We can mention the study of Sun et al., who showed that Cu-BTC was the best adsorbent among 12 representative porous materials, including silicate zeolites.[11] The careful analysis of the NO adsorption isotherm showed a significant gap between adsorption and desorption curves occurring during the desorption step. This behavior indicates a strong irreversible adsorption of some NO molecules located on the open copper sites obtained after dehydrating HKUST-1 and was confirmed by IR spectroscopy (Figure 1).[69]

Dietzel et al. collected NO adsorption isotherms using CPO- 27(Ni) also known as MOF-74(Ni), a 3D honeycomb like Ni- 2,5-dihydroxyterephthalate MOF possessing 1D hexagonal channels.[70] Adsorption tests collected using a microcalorimeter instrument equipped with a calibrated glass gas-volumetric apparatus showed a maximum uptake of 6.1 mmol NO per gram of MOF at 303 K and 42 mbar equilibrium pressure.

The authors used a set of complementary spectroscopic techniques to investigate the adsorption mechanism. They have demonstrated the formation of linear/tilted Ni(II)···NO species, showed that the NO−Ni distance is very short with a distance of 1.85−1.87 Å using EXAFS, and proved the instantaneous behavior of the molecular adsorption process by calorimetry.[71] In the meantime, McKinlay et al. published another study using CPO-27(Ni) and its analogue version CPO-27(Co). Adsorption isotherms display similar values with 7 mmol g^{-1} of NO adsorption for the Ni-based MOF and around 6.5 mmol g^{-1} for the Co version (Figure 2). It is interesting to note that the desorption arms show a hysteresis explained by the presence of NO molecules located on the open metal sites with a ratio of ~1 NO per OMS as proved by Rietveld refinement. Moreover, the authors demonstrated the stability of the frameworks after NO exposure by using PXRD and studied the effect of time. They completed their study by showing the impact of humidity where water molecules can replace coordinated NO after storage from 2 to 20 weeks of the NO-loaded MOF, which makes this material interesting for the controlled release of NO in medical applications.[72] Xiao et al. synthesized and characterized a coordinatively flexible copper sulfoisophthalate MOF ($Cu_2(OH)(C_8H_3O_7S)$-$(H_2O)\cdot 2H_2O$), denoted Cu-SIP-3·$3H_2O$, that has been used for NO adsorption. As evidenced by variable-temperature powder X-ray diffraction measurements, the material was subject to reversible structural transformations on hydration and dehy- dration, with significant changes occurring in the connectivity and coordination of the copper ions. After dehydrating the MOF, an extremely high selectivity to NO at low pressures has been observed opposite of other common gases, which was explained by a coordination-driven gating mechanism. NO storage capacity of Cu-SIP-3 is found to be around 1.1 mmol g^{-1} at 1 bar, equivalent to approximately 0.88 NO molecules per formula unit. Moreover, the NO-loaded material can release NO in a controlled manner by water addition leading to the original hydrated phase (Figure 3).[73]

In 2013, Miller et al.[74] reported a calcium-based MOF, named BioMIL-3, presenting coordinatively unsaturated Ca^{2+} Lewis acid sites that are able to trap and release nitric oxide at a biological level. After a pretreatment at 423 K, NO adsorption isotherms have been collected on the MOF and gave a total NO uptake of 0.8 mmol g^{-1} at 1 bar (Figure 4). As observed for the above-mentioned MOFs, the desorption

curve exhibits a large hysteresis, in agreement with the relatively strong binding of chemisorbed NO onto coordinatively unsaturated calcium sites. This observation is supported by IR spectroscopy where a ν(NO) band at 1890 cm^{-1} indicates the formation of d^0 (here Ca^{2+})−NO complexes. Moreover, the authors claimed that the total amount of NO adsorbed should be much higher to be comparable with the theoretical number of unsaturated sites of Ca^{2+} (4.6 mmol g^{-1}), and they supported this hypothesis by the absence of a plateau in the adsorption curve suggesting a possible higher adsorption at higher pressure.

The flexible isoreticular iron-based MOFs, MIL-88,[75] that have been prepared from linkers of different lengths and functionalities, were also studied by McKinlay et al. for their NO adsorption performances (Figure 5). NO sorption isotherms were performed after pretreatment at 150 °C under primary vacuum (except for the less stable MIL-88B-2OH at 80 °C). The largest amount of NO is adsorbed for MIL-88A(Fe), based on a fumaric acid ligand, with a total uptake of 2.5 mmol g^{-1}, while MIL-88B (Fe-terephthalic acid) and MIL-88Bs (Fe-amino- terephthalic acid or 2,5-dihydroxyterephthalic acid) adsorb ∼1.6 and ∼1 mmol g^{-1}, respectively. As described previously for other MOFs, the desorption arms of the isotherms show a large hysteresis, which would be consistent with the binding of chemisorbed NO onto open iron-accessible metal sites. In situ IR spectroscopy was performed in order to follow the adsorption and desorption of NO, especially the chemisorption on Fe^{3+} and Fe^{2+} open metal sites, exhibiting values equal to 0.2, 0.18, and 0.065 mmol of NO g^{-1} for MIL-88B, MIL-88B-NO_2, and MIL88A, respectively. Synchrotron PXRD has been used to analyze potential changes in the frameworks of MIL-88B-NO_2 and MIL-88B-2OH. The obtained PXRDs are almost identical after NO exposure demonstrating a very limited breathing of the structures. However, significant changes in the relative intensity occur, which is in agreement with the adsorption of NO molecules.[76]

In 2014, Serre and co-workers reported the adsorption of NO using three other reported MOF materials, namely, MIL-100(Fe and Cr)[77] and MIL-127(Fe).[78] All of these MOFs are built up from an inorganic building block defined as a trimer and presenting open metal sites (Figure 6). Adsorption isotherms have been recorded, and the reported values for MIL-100(Fe and Cr) after a pretreatment at 423 K under vacuum are within the 2.7−3.2 mmol g^{-1} range at 1 bar. For MIL-127, in the same conditions, the adsorbed amount is

around 1.2 mmol g^{-1}. It was previously described that an activation step at a higher temperature for iron-based MOFs leads to additional accessible Fe(II) sites thus available for a stronger interaction through a back-donation effect with unsaturated guest molecules, so the authors pretreated MIL-100 and MIL-127 at 523 K. Accordingly, the amounts of NO adsorbed increased to 4.5 and 2.2 mmol g^{-1}. As in the case of MOFs reported earlier, a pronounced hysteresis occurs in the desorption arm, confirming that NO is being retained on the Lewis acid sites.[79]

It is important to note that solid-state NMR techniques have been used by Khan et al. to determine the nature of the interactions occurring between adsorbed NO and open metal sites located in MIL-100 (Al),[80] HKUST-1, and its modified version $Cu_3(NHEtBTC)_2$. ^{15}N, ^{1}H, and ^{13}C NMR spectra together with analysis of the ^{1}H spin−lattice relaxation time (T1) allowed them to conclude that the mechanism of adsorption is following both a physisorption and chemisorption of nitric oxide and also demonstrated the formation of N- diazenium diolate (NONOate) as the primary mode of NO adsorption in the modified HKUST-1.[81] Mendt et al. also used pulsed electron paramagnetic resonance spectroscopy and density functional theory (DFT) simulations to study the NO adsorption of MIL-100 (Al) at low temperatures.[82]

A comparative study of NO sorption and release using UiO- 66, UiO-66-NH_2, TIFSIX-2-Cu-i, TIFSIX-4-Cu-i, TIFSIX-3-Ni (three hybrid ultramicroporous materials (HUMs) with pore aperture <4 Å), and an imidazole-based porous organic polymer (POP) have been conducted by Haikal et al. (Figure 7).[83] It is important to note that UiO-66-NH_2 has been selected for its ability to form N-diazeniumdiolates with NO, while the HUMs offer the opportunity to understand the value of NO−-metal ion coordination versus potential strong physical interactions within the micropores of the solids. Adsorption isotherms of each sample have been collected with a maximum NO uptake of 7.1 mmol g^{-1} for UiO-66-NH_2. An incomplete release of NO was observed as confirmed by the presence of hysteresis in the isotherm. On the contrary, the three HUMs exhibit type-I isotherms in the pressure range of 0−1 bar, demonstrating a fully reversible physisorption of NO molecules within the cavities. As a representative HUM, the heat of adsorption (Q_{st}) for NO in TIFSIX-2-Cu-I has been

evaluated to be in the range of 35−37 kJ mol^{-1}, and the linear shape of the Qst plot over the entire uptake range indicated fairly homogeneous adsorption sites for NO inside the material. The stabilities of the studied MOFs after NO adsorption have been estimated by PXRD. Only UiO-66- NH_2 present a PXRD pattern similar to that of the as- synthesized sample after NO sorption. PXRD of the three HUMs indicated poor crystallinity and/or phase changes after NO sorption as peaks do not match with the parent materials' patterns.[83]

2.1.2. Adsorption Mechanism. Although a few MOF materials were investigated for the adsorption of NO, the different conducted studies revealed an associated chemisorp- tion mechanism each time an open metal site was available after an activation process. Indeed, the literature review shows that only well-known MOFs with OMSs, namely, HKUST, MOF-74, MILs, and UiO-66, have been used for such applications. They were well known to coordinate polar or quadrupole molecules. Therefore, the previous desorption of such molecules, with an adequate activation, releases coordination sites which allow the adsorption of NO molecules through their unpaired electrons forming thus metal nitrosyl complexes. For example, the role of these OMSs has been highlighted by Barth et al.[84] on M-MIL- 100 (M = Al, Fe), by Xiao et al.[67] on HKUST-1, or by Jensen et al.[85] on Ti-MOF-74. The analysis of their adsorption isotherms shows a large gap between the adsorption and desorption curves, in agreement with the relatively strong binding of chemisorbed NO onto open metal sites. This gap has been confirmed using a set of complementary spectroscopic/analytical techniques such as X-ray diffraction, EXAFS, in situ infrared, calorimetry, and solid-state NMR. To the best of our knowledge, only one series of MOFs namely, TiFSIX-x-M (x = 2,3,4 and M = Cu, Ni), with no open metal sites has been evaluated for NO adsorption.[86] The analyses of the adsorption isotherm and the heat of adsorption reveal a fully reversible physisorption of NO molecules within the cavities.

2.1.3. MOF Stability after NO Exposure. Although many investigations have demonstrated the potential of MOFs for NO adsorption, stability after exposure has been rarely studied. It is worth mentioning that this parameter is not of prime importance for biological applications as the main objective is the release of NO within the body. However, if MOFs are envisioned to be used for capturing toxic gas from air or a gas stream, this stability parameter is of extreme importance. Highly stable MOF materials such MIL families have

demonstrated superior chemical stability toward NO species; this behavior has been confirmed by comparing PXRD patterns of the samples before and after NO exposure. It is important to mention that in the case of the TiFSIX family, the analysis of their PXRDs after exposure revealed amorphization of the materials and is supported by the significant changes in the patterns.[86]

2.2. Formation of NONOates Species. 2.2.1. Definition. The MOF community has developed an alternative strategy to selectively capture NO species based on the formation of a N- diazenium diolates unit, which is a well-known organic chemical reaction that results from the combination between an amine function and NO molecules (Figure 8).

2.2.2. Some Examples. To the best of our knowledge, the first report based on this strategy is attributed to Ingleson et al., who have postmodified HKUST-1 by a secondary amine in order to chemically adsorb NO creating N-diazenium diolates species, also called NONOate (Figure 9).[87] This example is interesting because the bifunctional secondary amine, namely, 4- (methylamino)pyridine (4-map), that contains a N sp^2 lone pair which reacts with NO, was introduced on the open metal sites of HKUST-1 by post-synthetic impregnation using vapor- phase diffusion at 413 K. HKUST-1 is defined by two types of cavities, a large and a small, for which only the larger can accept the diffusion of a 4-map. Although the 4-map-impregnated HKUST-1 has been found nonporous to N_2 (77 K), some porosity to small molecules such as water has been demonstrated using TGA and elemental microanalysis. No adsorption isotherms were performed, but the authors exposed the modified-HKUST-1 to 2 bar of NO for 72 h at 293 K, and the formation of N-diazenium diolate functionalities has been unambiguously identified by the appearance of diagnostic stretching bands in the IR spectrum. An amount of NO per Cu atoms of 23% has been quantified via elemental micro- analysis. According to their PXRD analysis, no loss of crystallinity is observed after NO adsorption. Finally, the ability of water molecules to act as efficient triggers for NO release has been demonstrated.[87] It is important to note that significant leaching of 4-map occurred due to $Cu-N_{py}$ bond breakage when the NONOate functionalized HKUST-1 was suspended in water which consequently presents one shortcoming of the noncovalent

approach. The instability of the Cu−N_{py} bond upon H_2O attack restricts the applicability of the material for NO delivery, as reversible NO storage via N-diazenium diolates is incompatible with metal−ligand coordination bond.

To overcome this issue, Cohen et al. decided to modify the strategy by using two different MOFs containing pendant primary amines, namely, IRMOF-3 and UMCM-1-NH_2 (Figure 10). The MOFs were exposed to a NO flux at 100 psi for 24 h. The presence of NONOate species was proved by FTIR and UV−vis spectroscopies. Powder and single crystal X-ray diffractions confirmed that the crystallinities of the bulk materials are preserved with cell parameters identical to those of pristine MOFs.[88] NO release in aqueous media has been investigated and demonstrated for both modified IRMOF-3 and UMCM-1. It is important to note that some instability of the NONOates functionality was observed after 10 days, which is not surprising as NONOates are certainly present in their protonated form as stated by the authors.

Lowe et al. have investigated the use of secondary amines for the formation of NONOates functionalities within MOF materials. Indeed, it is well known that NONOates derived from primary amines are not as stable as secondary amine-based NONOates. To illustrate this behavior, a Cu-TDPAT MOF (H_6TDPAT = 2,4,6-tris(3,5-dicarboxylphenyl-amino)-1,3,5-tri- azine) has been employed for the capture of NO species as mentioned in Figure 11. The NONOate formation has been proved by IR and Raman spectroscopies. XRD measurements after NO loading have been also performed and confirmed the stability of the material. The authors quantified a total amount of NO release at 85% humidity and room temperature of 175 μmol NO per g of Cu-TDPAT.[89] The authors have ascribed the better stability to the presence of secondary amines and also to the spatial conformation for certain NONOates functionalities that are close to open metal sites.

3. MOF ADSORBENT FOR NO_2

3.1. Methodology. As NO_2 is highly corrosive and toxic, very few research groups around the world are equipped to collect such isotherms. Hence, researchers have developed alternatives such as microadsorptive breakthrough experi- ments.[90] This is a dynamic method that consists of analyzing a flow of

diluted NO_2 with dry or humid air passing through a fixed-bed column system. NO_x concentrations in the outlet gas are mostly measured using an electrochemical sensor.

3.2. Impact of MOFs' Water Stability on NO_2 Adsorption Capacity. To the best of our knowledge, the first literature report using a MOF as a potential adsorbent for NO_2 is from 2010. Indeed, the NO_2 adsorption performances of HKUST-1 and HKUST-1/graphene composites (HKUST-1/ GO) have been evaluated in dry and humid conditions using microbreakthrough experiments under dynamic (nonequili- brium) conditions. For the case of HKUST-1, the quantity adsorbed in a dry condition is two times higher than the value obtained in moist conditions (106 and 54 mg g^{-1}, respectively). The stability of the MOF after reactive adsorption has been explored using X-ray diffraction and nitrogen adsorption at −196 °C. Intensities of the peaks in XRD were observed to decrease compared to the patterns of the pristine material, and the BET surface area was reported to drop by 90% after HKUST-1 was exposed to NO_2 in dry conditions, while in humid conditions only a 20% drop was observed in the BET surface area. The authors hypothesized a competition between NO_2 and water.[90] In humid conditions, both water and NO_2 can bind to copper resulting in a reduction in the number of adsorption sites. Furthermore, adsorbed water molecules occluded the small pores of the MOF, making them inaccessible for NO_2. However, the maximum capacity can be attained under dry conditions when all of the copper sites are accessible for binding to NO_2. Besides pure HKUST-1, the MOF/GO composites, made with different amounts of introduced GO, showed very similar NO_2 adsorption performances and trends to those of HKUST-1 in both dry and humid conditions. However, the NO_2 adsorbed amount was observed to be higher for the composites than the unmodified MOF. This is attributed to the additional porosity generated at the interface between the graphene layers and the MOF as a result of interactions between the functional groups of GO and the copper sites of HKUST-1. Because of the dense arrays of atoms in GO, the dispersive forces are predicted to be the highest in those new pores, enhancing adsorption.

In a later time, NO_2 adsorption measurements using UiO-66 and UiO-67 MOF platforms as adsorbents were conducted in dry and moisture conditions at ambient temperatures.[91] The impact of the pore aperture size on

the NO_2 adsorption performance has also been evaluated by using ligands of different sizes. Microadsorptive breakthrough experiments were per- formed to assess the adsorption capacities, and stabilities of the samples were checked after exposure to NO_2. According to the experimental results, the size and chemistry of a ligand were demonstrated to have impacted the adsorption property. UiO- 66 showed a better adsorption capability in dry circumstances (breakthrough capacity of 73 mg/g) than in wet ones (40 mg/ g), suggesting that water has a detrimental influence on NO_2 adsorption. The isoreticular MOF with the longer ligand (UiO- 67), on the other hand, has a greater breakthrough adsorption capacity in wet (118 mg/g) than in dry conditions (79 mg/g). According to the researchers, the existence of large pores in UiO-67 allows for the retention of water molecules and sequential dissolution of NO_2 molecules in a water film, resulting in a high adsorption capacity in humid conditions. Experimental results also showed that the NO release remains almost constant irrespective of the length of the ligand and the experimental conditions (dry or humid). However, the stability of the framework is an important issue due to the structural collapse of UiO-66 and UiO-67 after exposure to NO_2. The porosity of UiO-67 drops by roughly half after being exposed to NO_2 in humid conditions (BET surface area changes from 1372 to 620 m_2/g) but with relatively less change when subjected to NO_2 in a dry condition (BET of 1138 m_2/g). The authors claimed that the presence of water molecules facilitates the formation of nitrous and nitric acids causing the collapse of the framework. On the other hand, the porosity of UiO-66 reduced by around 17% after exposure in a dry condition but with no significant change in porosity in a humid condition. The enhanced reactive adsorption of NO_2 by the smaller pores within UiO-66 facilitating Zr−O bond cleavage under a dry condition and the small amount of NO_2 adsorbed by the MOF under a moist condition with water molecules blocking the access of Zr−O bonds to NO_2 could be attributed to the drastic differences between the impacts of the test conditions on the porosity. It is important to note that a partial loss of crystallinity is observed as confirmed by PXRD analysis.[91]

The effect of Ce^{3+} doping on the NO_2 adsorption performances of UiO-66 and UiO-67 under ambient conditions has also been investigated.[92] According to EDX and ICP results, the amount of cerium is 13.3% and 7.09% in Ce-UiO-66 and Ce- UiO-67, respectively. Owing to the formation of crystal defects, doping

UiO-66 and UiO-67 with Ce^{3+} resulted in a higher BET surface area than the undoped counterparts that is favorable for NO_2 reactive adsorption, with 95 and 86 mg g^{-1} adsorption capacities under a dry condition, respectively, which are superior to the 73 and 79 mg g^{-1} uptakes of the undoped UiO-66 and UiO-67, respectively, under the same conditions. The authors also concluded that the increase in NO_2 adsorption is correlated to the +3/+4 oxidation state of cerium cations, which implies more active centers for NO_2 binding. The impact of dry and humid conditions on the NO_2 adsorption and porosities after exposure were found to follow similar trends to the undoped analogues described above

This UiO-66 platform has also been used as an adsorbent for NO_x capture.[93] The authors translated the strategy applied in industry with liquid amine using either urea or melamine. The researchers used urea and melamine with NH_2 groups to modify UiO-66 and UiO-67 and explored the NO_2 removal efficiency of the modified MOFs in both dry and moist environments. According to the experimental results, the modified adsorbent's adsorption capacity was larger under humid than dry conditions. Moreover, under wet conditions, the adsorption capabilities of both UiO-66 and UiO-67 modified with urea were much higher than those of pure UiO-66 and UiO-67. Melamine, on the other hand, had a negative impact on the adsorption performance of UiO-66 and UiO-67 for NO_2. The differences in the structures of urea and melamine were hypothesized to alter the porosity and chemistry of the final products and hence the reactive adsorption of NO_2. In general, the best adsorption capacities (i.e., 101−154 mg g^{-1}) are obtained with urea, and according to the authors, the competitive adsorption of water is eliminated.[93]

An investigation on a modified version of a UiO-66 platform has also been conducted by using microbreakthrough experiments. The study compared pristine UiO-66 to its missing linker form that possesses vacancies at the terephthalate sites (UiO-66- vac) and to an oxalic acid modified form of UiO-66-vac (UiO- 66-ox) (Figure 12). A substantial increase of the NO_2 adsorption capacities is observed with a total uptake of 8.4 mmol g^{-1} for UiO-66-ox compared to UiO-66 and UiO-66-vac (3.8 and 3.9 mmol g^{-1}, respectively), which could be attributed to the reaction of NO_2 to the freely available carboxylic acids within the pores. Unfortunately, the analysis of the PXRD powder pattern showed structural degradation of the

materials after NO_2 exposure, which is also further confirmed by infrared spectros- copy shown in Figure 12.[94]

In addition to the different NO_2 adsorbent MOFs discussed above, most other well-known MOFs were also shown to be unstable toward NO_2 exposure as demonstrated by the recent report where the effects of dry and humid NO_2 gas on three representative zeolitic imidazole frameworks, ZIF-71, ZIF-72, and ZIF-90, were investigated. The loss of crystallinity and decrease in BET surface area proved the instability of these frameworks under NO_2 exposure.[95]

3.3. Water Stable MOF for NO_2 Adsorption. Later, the application of a UiO-66 platform with a modified ligand for NO_2 removal was reported by Peterson et al. with a record adsorption capacity of 1.4 g g^{-1} of NO_2 (under humid conditions) combined with a limited nitric oxide formation. The obtained uptake is by far higher than the adsorption capacities for the well- known material for such purpose, activated carbon BPL (Calgon Carbon Corporation) (0.72 g g^{-1}) and UiO-66 (0.61 g g^{-1}), under the same experimental conditions. From characterization results obtained from DRIFTS, XPS, and other temperature- dependent data, the plausible mechanism of NO_2 adsorption was suggested to be by the interplay of physical adsorption within the pores and different chemical reactions of the NO_2 with the aminoterephthalate moiety at different sites (Figure 13). In all the cases, the amine group is found to play a significant role, the potential reduction of NO_2 to N_2 via the diazotization route being a particularly interesting feature. PXRD analysis and the BET value also showed that the material is stable after exposure.[96]

As mentioned previously, very few research groups are able to collect NO_2 adsorption isotherms. The first one reported was performed on MFM-300(Al) (also called NOTT-300).[97] Under ambient temperature, the uptake at 1 bar is 14.1 mmol g^{-1} (Figure 14). This NO_2 uptake is fully reversible, and according to PXRD analysis, after five NO_2 adsorption cycles, crystallinity and uptake capacity remain unchanged showing the robustness of MFM-300(Al) under this harsh condition. The authors also demonstrate the high selective removal of low-concentration NO_2 in dry and wet conditions and from gas mixtures (NO_2/ CO_2 or NO_2/SO_2)

via breakthrough experiments (Figure 14).[98] The influence of the synthesis conditions on the adsorption properties was evaluated. Precisely, a microwave-assisted method has been used to produce MFM-300(Al) in 10 min instead of the 3 days required with the classical solvothermal route. A drastic NO_2 adsorption capacity increase by 90% at 298 K/0.01 bar was observed for the MOF prepared by microwave- assisted synthesis with 1.9 mmol g^{-1} uptake compared to the 1 mmol g^{-1} adsorbed amount by the MOF synthesized using the conventional way.[99] More importantly, the possibility to assemble better quality material with shortened reaction times enabled by controlled heating and with no alteration in the porosity attributes and thermal stability is considered to be a significant move in the transition from batch to the industrially important continuous processing. Later, the isostructural redox- active MOF, MFM-300(V), was also investigated for the potential removal of NO_2.[100] As proven by synchrotron X-ray diffraction and different characterization techniques, the adsorption of NO_2 by MFM-300(V) results in the oxidation of V(III) to V(IV) centers, with simultaneous reduction of NO_2 to NO. At 298 K and 1.0 bar, the MOF was found to exhibit a high isothermal NO_2 absorption of 13.0 mmol g^{-1} with a completely reversible behavior for many adsorption/desorption cycles.

It is also interesting to highlight other examples of stable MOFs under humid NO_2 exposure, i.e., rare-earth hexanuclear oxocluster-based MOFs assembled from rare earth cations (Y^{3+}, Yb^{3+}, Tb^{3+}, and Eu^{3+}) and a 2,5-dihydroxyterephthalic acid (DOBDC) linker, with a UiO-66 like topology. Precisely, the samples were exposed to 5 ppm of NO_x stream with 60% relative humidity, and the stability was verified using PXRD and FT-IR analysis.[101] As substantiated by experimental characterizations and density functional theory (DFT) simulations, water molecules are linked to the metallic cluster more strongly than NO_2, while NO_2 molecules are preferentially bound to the DOBDC ligand via hydrogen bonding interactions. Further- more, the modeling study confirmed the absence of differences in the binding energy among the isostructural RE-DOBDC MOFs.

4. CATALYTIC REDUCTION OF NO_x

4.1. Selective Catalytic Reduction Process (SCR). As mentioned in the Introduction, the selective catalytic reduction of NO_x can be performed using different reducing agents. With pure MOF or with modified MOF, only studies using NH_3 or CO or H_2, as the reductant, were reported.

4.1.1. NH_3 as Reducing Agent. 4.1.1.1. MIL-100, MIL-125.

To the best of our knowledge, the first study about MOFs used as catalysts for NH_3-SCR was reported by Wang et al.[102] The ability of MIL-100(Fe) to play the role of catalyst comes from the presence of unsaturated metal sites, the redox properties of Fe^{3+} and the MOF's thermal stability. In the temperature range of 245−300 °C, MIL-100(Fe) exhibits better performance in NH_3-SCR than the conventional V_2O_5−WO_3/TiO_2 catalyst with a NO_x conversion of more than 97% (Figure 15). The researchers also evaluated its durability in the presence of SO_2 and H_2O and demonstrated the full regeneration of the catalyst after cutting off the poisoning. According to XRD, SEM, and IR analyses, the structure of MIL-100(Fe) is retained after SCR below 300 °C.[102]

A few years later, Zhang et al. modified this MIL-100 platform by substituting some of the iron with manganese cations. A maximum NO_x conversion of 96% at 260 °C for the bimetallic MIL-100(Fe−Mn) was observed, while in their conditions only 78% and 53% are reached for MIL-100(Fe) and MIL-100(Mn), respectively. In this study, the three materials maintain good catalytic activity in the presence of 250 ppm of SO_2 and 5% of water. Finally, the authors suggested an Eley−Rideal mechanism, based on their in situ IR experiments in which the absorbed NH_2 species, derived from adsorbed NH_3, react directly with gaseous NO.[103] Theoretical investigations by density functional theory (DFT) have been conducted on MIL-100(Fe) with the Langmuir−Hinshelwood mechanism.[44] The authors proposed a two-step mechanism with NO oxidation followed by a fast SCR reaction. They also confirmed the essential role of Lewis acid sites to adsorb NH_3 species that can further react with adsorbed NO_2.[44]

Wang et al., in order to promote the NH_3-SCR of NO activity at low temperature, studied the effect of the amount of cerium deposited on MIL-100(Fe).[104] Cerium, deposited by impregnation, was in the form of cerium oxide nanoparticles and was positioned in the pores of MIL-100(Fe). The authors clearly showed the benefit of the addition of ceria nanoparticles over MIL-100(Fe) to increase the NO conversion in the temperature range of 50−180 °C (Figure 16). This increase was explained, from XPS and in situ DRIFTS analysis, by the fact that ceria promotes the NO oxidation into NO_2 and therefore favors the fast reaction. This idea of using MOF as a support for an oxide, i.e., manganese oxide, to promote the NH_3-SCR reaction, was taken up by the same group.[105]

MIL-125(Ti) was chosen for its high thermal stability with its large surface area and accessible pore diameters. The catalyst obtained, MnO_x@MIL-125(Ti), exhibited remarkable catalytic activity with NO conversions greater than 90% in the temperature range from 175 to 425 °C under the same conditions as those presented in their previous work.[102,104] The resistance to water addition (5 vol %) at 200 °C is remarkable. However, the addition of 200 ppm of SO_2, in the presence of water, lead to a rapid decline of the conversion from 98% to 60% but remains further constant with time-on-stream studies (Figure 17). This NO reduction performance was attributed to the high dispersion of MnO_x, the high Mn^{4+}/Mn^{3+} ratio, and the significant amount of surface chemical oxygen. The authors proposed a reaction scheme, as a function of temperature, where the SCR reaction proceeds via a Langmuir−Hinshelwood mechanism below 200 °C involving adsorbed NH_4^+ and adsorbed nitrite and nitrate species, as well as an Eley−Rideal mechanism for temperatures above 200 °C.

4.1.1.2. MOF-74. The other MOF tested as a catalyst for low- temperature denitrification was Co-MOF-74. A maximum NO conversion of 68% at 220 °C with 100% N_2 selectivity was reported,[106] while the Mn analogue led to 99% of conversion at 220 °C.[107] The catalytic tests over Mn and Co-MOF-74 catalysts, carried out in the presence of SO_2 and/or H_2O, showed a decrease of NO_x conversion with an almost full recovery after

cutting off the flow of these poisonous reactants. Only the Co-MOF-74 catalyst was not affected by the presence of SO_2 and hence maintained the NO_x conversion around 68%. According to TPD and DRIFTS experiments combined with DFT calculations, the authors suggest that both Langmuir− Hinshelwood and Eley−Rideal mechanisms occur. Moreover, the effect of synthesis conditions of Co-MOF-74 is studied in the low-temperature NH_3-SCR. According to this report, Co-MOF- 74 synthesized in isopropanol shows the highest NO conversion of 97.8% at 230 °C. Full recovery after H_2O poisoning is observed, and SO_2 addition in the inlet flow has only a small influence on the catalytic performance, revealing NO conversion of 85% at the beginning and 93% after 4 h (Figure 18).

As demonstrated by TPD, two kinds of acidic sites are present in this sample, resulting in enhanced NH_3 adsorption leading to an acceleration of high NO_x conversions.[108] In 2018, bimetallic Mn/Co-MOF-74 was fabricated in order to combine the high NO_x conversion of the Mn single phase and the resistance toward SO_2 of the Co version. $Mn_{0.66}Co_{0.34}$-MOF-74 exhibits the best performance with 99.3% of NO conversion at 200 °C. This catalyst is also highly resistant to SO_2 thanks to the presence of Co that instigates attenuation of the SO_2 adsorption strength on the surface (NO conversion is maintained at 96%− 99%).[109] Wang et al.[110] investigated differently modified Mn- MOF-74 for low-temperature NH_3-SCR. The authors assumed the presence of either poly(ethylene oxide)-polypropylene- poly(ethylene oxide) (P123) or polyvinylpyrrolidone (PVP) on the surface of Mn-MOFs. The third studied catalyst was modified by hydrophobic groups ($-CH_3$). Among the tested materials, Mn-MOF-74 archived the highest NO conversion of nearly 100% from 220 to 240 °C in the NH_3-SCR without the presence of water vapor. Unfortunately, the introduction of H_2O in the feed stream generated a huge drop of 44% in NO conversion observed for the studied Mn-MOF-74. The P123- modified version of the Mn analogue (P123-Mn-MOF-74) showed enhanced water resistance, maintaining 92.1% of NO conversion before, after, and during water feeding for 3 h. This synthesis strategy gives a new insight on the way to design novel low-temperature NH_3-SCR catalysts.[110] More recently, Xie et al. have reported an NH_3-SCR study on MOF-74(M) with M = Mn, Co, Ni, Zn, MnCo, MnNi, and MnZn.[111] From the catalyst screening, the best catalytic activity was observed for MOF-74- Mn, which is attributed to

the existence of various valence states of Mn being able to strengthen the redox properties necessary for the NO oxidation step. According to in situ DRIFTS analysis, the authors proposed a possible reaction mechanism for MOF- 74-MnCo and MOF-74-Mn, in which the Eley−Rideal model dominates at low temperatures while the Langmuir−Hinshelwood mechanism controls the reaction at high temperatures.

4.1.1.3. HKUST-1. HKUST-1 or MOF-199 as a famous MOF has been evaluated as a novel catalyst for low-temperature SCR of NO with NH_3. After pretreatment in an inert atmosphere at 230 °C, nearly 100% of NO conversion is reached from 220 to 280 °C following a fast decrease due to structure collapse (Figure 19). In situ FT-IR confirmed the formation of a Cu(II)− NH_3 which is the result of the interaction between NH_3 and the open Lewis acid sites of the framework.[112]

Many investigations were conducted to evaluate the impact of the open metal sites on the catalytic experiments. Remarkable results were obtained by investigating a series of Cu-BTC modulated by acetic acid (AA), and the best catalytic performance was obtained for the 25%-AA-Cu-BTC with 95.5% NO conversion at 280 °C.[113] On the other hand, a series of Mn@Cu-BTC-X (X depending on the Mn^{2+} concentration), obtained after immersion of Cu-BTC in a Mn^{2+} solution for 2 h followed by solvothermal treatment at 90 °C for 24 h, has been studied. After activation at 230 °C for 60 min in a He flow, a remarkable result was obtained for Mn@Cu- BTC-0.05 with a conversion efficiency close to 100% in the temperature range of 220–260 °C and N_2 selectivity near 100%. DRIFTS experiments were performed showing that NH_3 is adsorbed on Lewis sites, and no peaks corresponding to NO were observed. The authors suggest that the combination of proper pore sizes, enhancement of redox activity via incorporation of Mn^{4+} ions, and the synergistic effect between Mn^{2+} and Cu^{2+} results in superior $DeNO_x$ performance.[114] The commercial HKUST-1 (Basolite C300) was examined under NH_3-SCR conditions in the studies of Swirk et al.[115,116] During the pretreatment step carried out in helium from 145 to 250 °C, the authors observed a gradually increasing formation of carbon dioxide with a heating ramp, highlighting the crucial role of the temperature. The temperature of 185 °C is recognized as the highest possible and carbon-free experimental adjustment, allowing the authors to prevent a partial decomposition of the organic framework. The bare

Basolite C300 showed no activity in NH_3-SCR, and the disappearance of NO is ascribed to the adsorption phenomenon. By studying different promoters (V, Nb, and Mn) introduced by the facile impregnation method, it was reported that the manganese modified Basolite C300 (HKUST-1-Mn) can reach the highest NO and NH_3 conversions of 80% and 100%, respectively, at 185 °C.[115]

After stabilizing the activity values, the NO and NH_3 conversions are reported to be 78% and 73%–84%, respectively. Different loadings of Mn (2.5, 3.75, 5.0, 7.5, and 10.0 wt %) were analyzed, and structural and textural modifications were evidenced by the creation of new mesopores.[116] According to the authors, the mesoporosity could promote, to some extent, the diffusion properties, allowing easy access of molecules to enhance the catalytic activity in the NH_3-SCR process. Moreover, for the first time, Swirk et al.[115,116] examined the commercial HKUST-1-supported catalysts in the presence of H_2O (3.5 vol %) and SO_2 (100 ppm) in NH_3-SCR. Both reactants were introduced separately. A rapid decrease was reported for HKUST-1-Mn3.75 after the introduction of water vapor showing the conversions dropping from 68% to 25% and 65% to 30% for NO and NH_3, respectively. Once the H_2O feeding was terminated, the initial conversions are almost fully recovered and stable after 90 min of time-on-stream studies. The influence of SO_2 has a more remarkable effect on catalytic performance, revealing a decrease of NO conversion from 68% to 48% with no recovery when the SO_2 flow is stopped. The conversion of NH_3 increased during the SO_2 feeding, suggesting that either an improvement of acidic properties in contact with SO_2 occurred or ammonia reacted with sulfur dioxide to form NH_4HSO_4 (ammonium bisulfate) and/or $(NH_4)_2SO_4$ (ammo- nium sulfate) blocking the pores of the catalyst. The latter hypothesis may support the behavior of the HKUST-1-Mn3.75 which has been permanently deactivated after the introduction of SO_2.

Recently, Gao et al.[117] fabricated three different HKUST-1 samples with either octahedral, cubic, or tetrakaidekahedral morphologies. The as-synthesized HKUST-1-O, HKUST-1-C, and HKUST-1-T catalysts were tested in the NH_3-SCR process to understand the role of catalyst structure on catalytic behavior. Both cubic and tetrakaidekahedral forms showed abundant Cu(I) defective sites, resulting in the enrichment of

low-strength Lewis acid sites. In the catalytic test, HKUST-1-T revealed the best performance in the temperature range of 200−240 °C with a maximum of 93% NO removal.

4.1.1.4. Other MOFs. A comparative study of manganese− cerium-doped UiO-67-based MOFs was conducted for SCR experiments. These Mn/Ce MOF-based catalysts were prepared via two different synthesis methods: postsynthetic impregnation and one-pot synthesis. The authors found that the MOF prepared by the simple impregnation method resulted in the highest catalytic efficiency with more than 98% of NO conversion from 200 to 300 °C. The authors also investigated the effect of SO_2 and H_2O on the NO conversion. As presented in Figure 20, the MnCe@MOF catalyst still performed with an acceptable tolerance to both reactants under NH_3-SCR conditions.[118]

Using manganese oxide, Zhang et al. examined the effect of MnO_x content, deposited on UiO-66 by an in situ method, on the NH_3-SCR activity.[119] A minimal quantity of MnO_x is required to achieve high NO conversion in the 50−150 °C temperature window. Among the catalysts prepared, the 8.5 wt %-MnO_x/UiO-66 catalyst exhibited the best performance with a 90% NO conversion between 100 and 290 °C. This catalyst showed good resistance in the presence of 100 ppm of SO_2 and 5% H_2O and maintained its high activity during a 24 h stability test performed at 200 °C (Figure 21). Moreover, the used sample retained most of its structure and porosity after differently conducted catalytic tests. These authors stressed the importance of the method of addition of manganese oxide to the material.

Nickel-based MOFs have been studied by Sun et al.[120] and exhibit nearly 92% NO conversion for a sample pretreated at 220 °C with a large operating temperature window from 275 to 440 °C. According to the NH_3-TPD experiments, a combination of physical and chemical adsorption of NH_3 on Bronsted or Lewis acid sites is observed for Ni-MOFs. NH_3 ions are adsorbed on the nickel sites in the form of ionic NH_4^+ and coordinated $-NH_2$. The latter is known to be an important intermediate of the Eley−Rideal mechanism. This allowed the authors to draw the conclusion that Ni-MOF follows the above-mentioned mechanism.[120]

Very recently, cerium-based MOFs, i.e. Ce-UIO-66 and Ce- CAU-24,[121] and mixed cerium/zirconium Ce_x/Zr-CAU-24, were evaluated as NH_3-SCR catalysts (Figure 22). The combination of acidic open zirconium sites with redox-active cerium sites results in a higher SCR activity, despite a partial loss of crystallinity of spent catalysts as supported by PXRD. Ce- UiO-66 was found to be more active in NH_3-SCR compared to Ce-CAU-24. The former achieved ca. 78% NO conversion at 230 °C, whereas the addition of 5 vol % of water vapor caused a reversible activity drop of 30% because of the hydrophilicity of open metal sites.[122]

It should be underlined that most of the low-temperature NH_3-SCR of NO reported in the following table on MOF-based catalyst were performed using weight hourly space velocity (WHSV) equivalent to the tests carried out with mixed oxides or zeolite-based catalysts.[27,123,124] The mechanisms associated with these catalysts are similar to those reported generally for mixed oxide catalysts.[27] The SCR studies carried out on unmodified and modified MOFs, reported so far, clearly show the potential of this type of materials. To facilitate a quick overview of all the work, Table 1 summarizes the catalytic performances using NH_3 as the reducing agent.

4.1.2. CO as Reducing Agent. Only a few examples of SCR using CO as the reducing agent were reported in the literature. To the best of our knowledge, the first evaluation has been conducted with a series of bimetallic MOF-74-Co_{1-x}/Mn_x (where x represents the molar ratio of Co to Mn). The best result was obtained for MOF-74-Co_1Mn_2 with a catalytic reduction of NO with CO close to 100% within a temperature range of 175−275 °C.[125] A few other MOF materials were employed as catalysts for CO-based SCR catalysis. Ag_x-Cu-BTC was made through a preassembled method and tested in CO- SCR for NO reduction. After the assumed pretreatment of $Ag_{0.5}$- Cu-BTC (N_2 flow, 3 h at 240 °C), a full conversion of NO was reported at 238 °C.[126] Alternatively, a cerium-based Cu-BTC MOF showed 91% in NO conversion at 250 °C. In situ DRIFTS experiments have been performed allowing the authors to conclude that the catalytic conversion follows a Langmuir− Hinshelwood mechanism in which adsorbed NO and CO species react to generate N_2 and CO_2 as shown in Figure 23.[127]

Finally, Me-ZIF-67@CuO_x (with Me = Mn, Fe, Al, or Zn) have been studied as low temperature CO-SCR catalysts.[128] MeZIF-67@Cu-BTC was synthesized and treated at 320 °C for 1 h in a microreduction atmosphere to obtain a coated Me-ZIF-67. In this series, Al-ZIF-67@CuO_x exhibited the best performance with a denitrification of 99% at 200 °C, whereas the Mn-doped version showed better resistance in the presence of SO_2. Figure 24 presents a proposed reaction scheme in which the doped elements played a dual-channel synergistic catalytic role with the Co^{2+} from the initial framework. The authors also suggest a Langmuir−Hinshelwood mechanism.

Recently, bimetallic $Ni_{1-x}Mn_x$-MOF-74 (x = 0.1, 0.2, 0.35, and 0.5) catalysts were investigated in CO-SCR by Shi et al.[129] $Ni_{0.65}Mn_{0.35}$-MOF-74 was found to be the most active material, achieving NO conversion of ca. 100% in the temperature range from 175 to 300 °C (Figure 25). This fact was assigned to the formation of more active Ni^{3+} and Mn^{4+} components, being beneficial for the formation of more oxygen vacancies and metal active sites. The results of in situ FT-IR allowed the authors to assume a Langmuir−Hinshelwood mechanism, as the acceleration of CO/NO adsorption and activation ability were demonstrated.

The SCR studies carried out on unmodified and modified MOFs, reported so far, clearly show the potential of this type of material. To facilitate a quick overview of all the work, Table 2 summarizes the catalytic performances using CO as the reducing agent.

4.1.3. H_2 as Reducing Agent. Xue et al. proposed an original study dealing with the H_2-SCR process over Pt/MIL-96(Al) MOF catalysts.[130] The authors showed that Pt particles can be uniformly dispersed on MIL-96 via a simple hydrothermal method. Additionally, the catalysts were evenly sprayed on the carbon paper (CP), and the so-prepared specimens were tested and compared in H_2-SCR conditions. The role of carbon paper is to provide a mechanical support layer. The resulting materials are very efficient in NO removal using a simulated flue gas carried out in a gas diffusion reactor with a short residence time. The experiments were conducted in a very narrow temperature window, i.e., between 20 and 90 °C. Figure 26A shows the reported catalytic performance, and Pt_5MIL-96/CP was found to be the best performing catalyst sprayed on hydrophobic carbon paper. The high removal efficiency is related to the Pt content, the control of Pt

deposition, and the synergistic effect between Pt particles and MIL-96. This synergy was explained by the fact that the MIL-96 support, with a high surface area, is wildly recognized as H_2 storage material. Furthermore, the authors analyzed differently supported Pt-containing catalysts (Figure 26B). Only Pt_5MIL-96 (NO conversion of 100% at 60 °C) and Pt/TiO_2 (NO conversion of 100% at 80 °C) can completely remove NO in the inlet gas under the studied conditions.

4.2. Photocatalysis. Photocatalysis is the last strategy that researchers have considered for conversion of NO_x species. Two investigations were reported in the literature using MIL series materials: MIL-88B, MIL-53, and MIL-101.[131,132] Sample dishes were coated by MOFs, placed in a reactor, and then submitted to an inlet gas flow of NO and air with a NO concentration of 350−400 ppb and relative humidity about 50%.

Experiments were performed at room temperature with solar light source simulated by a xenon arc lamp, while the outlet gases were detected by a NO_x analyzer. The best photocatalytic activity for NO_x removal under solar irradiation was found for MIL-101 with a total conversion of 76% (Figure 27). According to the authors, this high efficiency of $DeNO_x$ performance is due to the rigidity of the framework, the large specific surface area, the presence of open metal sites, and nanosized clusters in the network inhibiting the recombination of light-driven charges.

ZIF-8 was also tested for photocatalytic removal of NO[133] and compared with its composites containing carbon quantum dots (CQDs). The CQDs were found to be effective to boost the visible-light photocatalytic activity of ZIF-8 (Figure 28), improving the visible light utilization and carrier separation efficiency. The best performing catalyst was 0.5-CQDs/ZIF-8 with 18.3% NO conversion at the testing conditions used by the authors. The authors reported only 7.1% of NO removal for ZIF- 8 under 365 nm UV light irradiation. Surprisingly, pristine ZIF-8 showed negligible or almost no activity under visible monochromatic light irradiation of 365, 500, 550, 600, and 700 nm.

Recently, Chen et al.[134] examined NH_2-UiO-66(Zr) for NO conversion by photocatalysis. The authors introduced Cu^{I}/Cu^{II} species on NH_2-UiO-66 (Zr) via in situ partial reduction of copper during its coordination with $-NH_2$ groups and oxygen donors in MOFs. Upon the introduction of copper species, a ligand to linker

metal charge transfer (LLMCT) pathway was formed, allowing the electron transfer from organic linkers to Cu centers (Figure 29). The LLMCT pathway effectively promoted the electron transfer rate, inhibiting the recombination of photogenerated electron-hole pairs. The Cu^{I}/Cu^{II}-modified MOFs presented significant photocatalytic behavior with 88% of NO removal under visible light irradiation ($\lambda > 420$ nm). Such high activity was complemented by good stability (up to 24 h) and selectivity (almost no NO_2 side product was formed).

5. CHALLENGES AND PERSPECTIVES

Metal−organic frameworks are appealing candidates for NO_x adsorption, separation, and conversion. An increasing number of reports on this topic became available in recent years. In addition to excellent textural properties, including high specific surface area, pore size, pore volume, and chemical tunability, MOF materials still face the problem of thermal stability at temperatures higher than 250−300 °C. Moreover, the lack of enhanced resistance in the presence of H_2O and SO_2 may prevent the use of MOFs in industrial applications for conversion of exhaust gases. However, in the absence of water and sulfur oxide, the catalytic performance is very promising. Because dehydration and desulfurization are costly processes, several research groups are currently working on the develop- ment of highly stable MOF materials. The efforts to develop these types of catalysts and adsorbers for NO_x removal should continue. An important effort must be devoted to fabricate ultrahigh stable MOFs. Practically, material chemists should take into consideration a large panel of parameters that are found to impact thermal and chemical stability properties such as the coordination environment, metal composition, oxidation state, nature of the organic linker, interpenetration, flexibility, and framework dimensionality. Another challenge with the use of MOFs is the lack of knowledge about the toxicology of the used materials after exposure to gaseous NO_x. Accordingly, researchers should dedicate important investigations to this area. Nevertheless, the effectiveness of MOFs in air purification, such as NO_x adsorption, selective catalytic reduction with a reducing agent, or in photocatalysis, is very attractive and promising. The development of eco-friendly, thermal, and chemical MOF materials will pave the way for a new generation of catalysts for NO_x removal.

6. CONCLUSION

This review offers an overview on the recent progress made in the NO_x field and provides interesting routes on the use of MOFs for their selective adsorption, release, and/or catalytic conversion. Indeed, MOF materials are interesting platforms for capturing NO_x molecules using mainly the chemisorption mechanism due to the presence of open metal sites. It should be mentioned that chemical stability to H_2O or SO_2 is an important parameter to consider before assessing any MOF candidate. Although high selectivity was obtained with some well-known platforms, such as HKUST-1, MIL-101, or MOF-74, it would be of particular interest to consider MOFs with small pores for selective capture of NO_x using a physisorption mechanism to reduce the temperature of regeneration. On the other hand, MOF materials can act as catalysts using photocatalytic or selective catalytic reactions in the presence of NH_3, CO, or H_2. It is to highlight high selectivity (>99%) and conversion (>95%) results obtained in the range of 200−300 °C by judiciously selecting/combining appropriate metallic cations, such as Mn^{2+}, Co^{2+}, Ni^{2+}, and even Ce^{4+}. This temperature can be further lowered if the MOF platform is optimized by adding nanoparticles within their porosity. Among the reviewed studies, the most promising MOFs tested in NH_3-SCR are MIL-100, MOF-74, and HKUST-1(Cu-BTC). On the other hand, good working materials in CO-SCR were based on MOF-74, Cu- BTC, or ZIF-67. A direct comparison of their catalytic performance is impossible as the test conditions are different. In summary, the MOF platform is a key choice for capturing and converting harmful NO_x. The development of new metal− organic frameworks, associated with systematic structure− property relationships assisting with theoretical calculations, would pave the way for efficient adsorbents.

ACKNOWLEDGMENTS

The authors acknowledge the Programme d'investissements d'avenir (PIA) in France for funding with Grant ANR-18- ■MOPGA-0009 and the Occitanie Region.

REFERENCES

(1) Kumar, P.; Kim, K. H.; Rarotra, S.; Ge, L.; Lisak, G. The Advanced Sensing Systems for NO_x Based on Metal-Organic Frameworks: Applications and Future Opportunities. TrAC - Trends Anal. Chem. 2020, 122 (2), 115730.

(2) Clean Air Act, Section 407, USA, 2004, https://www.govinfo.gov/ content/pkg/USCODE-2011-title42/html/USCODE-2011-title42- chap85-subchapIV-A-sec7651f.htm.

(3) GB 13223-2011, China, 2011, https://www.chinesestandard.net/ PDF.aspx/GB13223-2011.

(4) GB 18352.6-2016, https://www.chinesestandard.net/PDF.aspx/ GB18352.6-2016.

(5) Wen, M.; Li, G.; Liu, H.; Chen, J.; An, T.; Yamashita, H. Metal- Organic Framework-Based Nanomaterials for Adsorption and Photo- catalytic Degradation of Gaseous Pollutants: Recent Progress and Challenges. Environ. Sci. Nano 2019, 6 (4), 1006−1025.

(6) Li, Y.; Xiao, A.-S.; Zou, B.; Zhang, H.-X.; Yan, K.-L.; Lin, Y. Advances of Metal−Organic Frameworks for Gas Sensing. Polyhedron 2018, 154, 83−97.

(7) Khan, M. A. H.; Rao, M. V.; Li, Q. Recent Advances in Electrochemical Sensors for Detecting Toxic Gases: NO2, SO2 and H2S. Sensors (Switzerland) 2019, 19 (4), 905.

(8) Wales, D. J.; Grand, J.; Ting, V. P.; Burke, R. D.; Edler, K. J.; Bowen, C. R.; Mintova, S.; Burrows, A. D. Gas Sensing Using Porous Materials for Automotive Applications. Chem. Soc. Rev. 2015, 44 (13), 4290−4321.

(9) Schulz, M.; Gehl, A.; Schlenkrich, J.; Schulze, H. A.; Zimmermann, S.; Schaate, A. A Calixarene-Based Metal−Organic Framework for Highly Selective NO2 Detection. Angew. Chemie - Int. Ed. 2018, 57 (39), 12961−12965.

(10) Zhou, X.; Su, Z.; Chen, H.; Xiao, X.; Qin, Y.; Yang, L.; Yan, Z.; Sun, W. Capture of Pure Toxic Gases through Porous Materials from Molecular Simulations. Mol. Phys. 2018, 116 (15−16), 2095−2107.

(11) Sun, W.; Lin, L.-C.; Peng, X.; Smit, B. Computational Screening of Porous Metal-Organic Frameworks and Zeolites for the Removal of SO2 and NO_x from Flue Gases. AIChE J. 2014, 60 (6), 2314−2323.

(12) Zafirova, Z.; Sheehan, C.; Hosseinian, L. Update on Nitrous Oxide and Its Use in Anesthesia Practice. Best Pract. Res. Clin. Anaesthesiol. 2018, 32 (2), 113−123.

(13) Buhre, W.; Disma, N.; Hendrickx, J.; DeHert, S.; Hollmann, M. W.; Huhn, R.; Jakobsson, J.; Nagele, P.; Peyton, P.; Vutskits, L. European Society of Anaesthesiology Task Force on Nitrous Oxide: A Narrative Review of Its Role in Clinical Practice. Br. J. Anaesth. 2019, 122 (5), 587−604.

(14) Gopalakrishna, A.; Bole, R.; Lipworth, R.; Jimbo, M.; Helo, S.; Kohler, T.; Ziegelmann, M. Use of Nitrous Oxide in Office-Based Urologic Procedures: A Review. Urology 2020, 143, 33−41.

(15) Denisova, K. O.; Ilyin, A. A.; Rumyantsev, R. N.; Ilyin, A. P.; Volkova, A. V. Nitrous Oxide: Production, Application, and Protection of the Environment. Russ. J. Gen. Chem. 2019, 89 (6), 1338−1346.

(16) Lew, V.; McKay, E.; Maze, M. Past, Present, and Future of Nitrous Oxide. Br. Med. Bull. 2018, 125 (1), 103−119.

(17) Liu, Y.; Liu, L.; Wang, Y. A Critical Review on Removal of Gaseous Pollutants Using Sulfate Radical-Based Advanced Oxidation Technologies. Environ. Sci. Technol. 2021, 55 (14), 9691−9710.

(18) Yan, J.; Zhou, F.; Zhou, Y.; Wu, X.; Zhu, Q.; Liu, H.; Lu, H. Wet Oxidation and Absorption Procedure for NO_x Removal. Environ. Technol. Innov. 2018, 11 (x), 41−48.

(19) Palma, V.; Cortese, M.; Renda, S.; Ruocco, C.; Martino, M.; Meloni, E. A Review about the Recent Advances in Selected Nonthermal Plasma Assisted Solid−Gas Phase Chemical Processes. Nanomaterials 2020, 10 (8), 1596.

(20) Zhang, Y.; Cao, G.; Yang, X. Advances in De-NO_x Methods and Catalysts for Direct Catalytic Decomposition of NO: A Review. Energy Fuels 2021, 35 (8), 6443−6464.

(21) Zhang, C.; Zhao, J.; Sun, C.; Li, S.; Zhang, D.; Guo, T.; Li, W. Two-Stage Chemical Absorption−Biological Reduction System for NO Removal: System Start-up and Optimal Operation Mode. Energy Fuels 2018, 32 (7), 7701−7707.

(22) Zhang, D.; Ren, L.; Yao, Z.; Wan, X.; Lu, P.; Zhang, X. Removal of Nitrogen Oxide Based on Anammox through Fe(II)EDTA Absorption. Energy Fuels 2017, 31 (7), 7247−7255.

(23) Cheon, S.; Kim, S. H.; Yoon, H. C.; Han, J.-I. Resistive Oxidation Kinetics of Iron(II) Thiochelate Used as a Nitric Oxide Absorbent in Flue Gas. Energy Fuels 2020, 34 (8), 9940−9947.

(24) Sun, Y.; Wei, G.; Tantai, X.; Huang, Z.; Yang, H.; Zhang, L. Highly Efficient Nitric Oxide Absorption by Environmentally Friendly Deep Eutectic Solvents Based on 1,3-Dimethylthiourea. Energy Fuels 2017, 31 (11), 12439−12445.

(25) Granger, P. Challenges and Breakthroughs in Post-Combustion Catalysis: How to Match Future Stringent Regulations. Catal. Sci. Technol. 2017, 7 (22), 5195−5211.

(26) Arfaoui, J.; Ghorbel, A.; Petitto, C.; Delahay, G. Novel V2O5- CeO2-TiO2-SO42- Nanostructured Aerogel Catalyst for the Low Temperature Selective Catalytic Reduction of NO by NH3 in Excess O2. Appl. Catal. B Environ. 2018, 224, 264−275.

(27) Damma, D.; Ettireddy, P. R.; Reddy, B. M.; Smirniotis, P. G. A Review of Low Temperature NH3 -SCR for Removal of NOx. Catalysts 2019, 9, 349.

(28) Zhou, J.; Guo, R.; Zhang, X.; Liu, Y.; Duan, C.; Wu, G.; Pan, W. Cerium Oxide-Based Catalysts for Low-Temperature Selective Catalytic Reduction of NO_x with NH3: A Review. Energy Fuels 2021, 35 (4), 2981−2998.

(29) Liu, Y.; Zhang, J.; Pan, J.; Tang, A. Investigation on the Removal of NO from SO2-Containing Simulated Flue Gas by an Ultraviolet/ Fenton-Like Reaction. Energy Fuels 2012, 26 (9), 5430−5436.

(30) Liu, Y.; Wang, Y.; Yin, Y.; Pan, J.; Zhang, J. Oxidation Removal of Nitric Oxide from Flue Gas Using an Ultraviolet Light and Heat Coactivated Oxone System. Energy Fuels 2018, 32 (2), 1999−2008.

(31) Liu, Y.; Shi, S.; Wang, Y. Removal of Pollutants from Gas Streams Using Fenton (-like)-Based Oxidation Systems: A Review. J. Hazard. Mater. 2021, 416, 125927.

(32) Wang, Y.; Wang, Z.; Liu, Y. Review on Removal of SO2, NO_x, Mercury, and Arsenic from Flue Gas Using Green Oxidation Absorption Technology. Energy Fuels 2021, 35 (12), 9775−9794.

(33) Akhtar, F.; Andersson, L.; Ogunwumi, S.; Hedin, N.; Bergström, L. Structuring Adsorbents and Catalysts by Processing of Porous Powders. J. Eur. Ceram. Soc. 2014, 34 (7), 1643−1666.

(34) Zhou, H.-C.; Kitagawa, S. Metal−Organic Frameworks (MOFs). Chem. Soc. Rev. 2014, 43 (16), 5415−5418.

(35) Adil, K.; Belmabkhout, Y.; Pillai, R. S.; Cadiau, A.; Bhatt, P. M.; Assen, A. H.; Maurin, G.; Eddaoudi, M. Gas/Vapour Separation Using Ultra-Microporous Metal-Organic Frameworks: Insights into the Structure/Separation Relationship. Chem. Soc. Rev. 2017, 46 (11), 3402−3430.

(36) Furukawa, H.; Cordova, K. E.; O'Keeffe, M.; Yaghi, O. M. The Chemistry and Applications of Metal-Organic Frameworks. Science (80-.). 2013, 341, 6149 DOI: 10.1126/science.1230444.

(37) Zhang, T.; Lin, W. Metal-Organic Frameworks for Artificial Photosynthesis and Photocatalysis. Chem. Soc. Rev. 2014, 43 (16), 5982−5993.

(38) Antypov, D.; Shkurenko, A.; Bhatt, P. M.; Belmabkhout, Y.; Adil, K.; Cadiau, A.; Suyetin, M.; Eddaoudi, M.; Rosseinsky, M. J.; Dyer, M. S. Differential Guest Location by Host Dynamics Enhances Propylene/ Propane Separation in a Metal-Organic Framework. Nat. Commun. 2020, 11 (1), 1−8.

(39) Xu, Y.; Li, Q.; Xue, H.; Pang, H. Metal-Organic Frameworks for Direct Electrochemical Applications. Coord. Chem. Rev. 2018, 376, 292−318.

(40) Mason, J. A.; Oktawiec, J.; Taylor, M. K.; Hudson, M. R.; Rodriguez, J.; Bachman, J. E.; Gonzalez, M. I.; Cervellino, A.; Guagliardi, A.; Brown, C. M.; et al. Methane Storage in Flexible Metal-Organic Frameworks with Intrinsic Thermal Management. Nature 2015, 527 (7578), 357−361.

(41) Chen, Z.; Thiam, Z.; Shkurenko, A.; Weselinski, L. J.; Adil, K.; Jiang, H.; Alezi, D.; Assen, A. H.; O'Keeffe, M.; Eddaoudi, M. Enriching the Reticular Chemistry Repertoire with Minimal Edge-Transitive Related Nets: Access to Highly Coordinated Metal-Organic Frame- works Based on Double Six-Membered Rings as Net-Coded Building Units. J. Am. Chem. Soc. 2019, 141 (51), 20480−20489.

(42) Hu, Z.; Deibert, B. J.; Li, J. Luminescent Metal-Organic Frameworks for Chemical Sensing and Explosive Detection. Chem. Soc. Rev. 2014, 43 (16), 5815−5840.

(43) Moumen, E.; Assen, A. H.; Adil, K.; Belmabkhout, Y. Versatility vs Stability. Are the Assets of Metal−Organic Frameworks Deployable in Aqueous Acidic and Basic Media? Coord. Chem. Rev. 2021, 443, 214020.

(44) Zhang, M.; Wang, W.; Chen, Y. Theoretical Investigation of Selective Catalytic Reduction of NO on MIL-100-Fe. Phys. Chem. Chem. Phys. 2018, 20 (4), 2211−2219.

(45) Mileo, P. G. M.; Adil, K.; Davis, L.; Cadiau, A.; Belmabkhout, Y.; Aggarwal, H.; Maurin, G.; Eddaoudi, M.; Devautour-Vinot, S. Achieving Superprotonic Conduction with a 2D Fluorinated Metal- Organic Framework. J. Am. Chem. Soc. 2018, 140 (41), 13156−13160.

(46) Mondloch, J. E.; Katz, M. J.; Isley, W. C.; Ghosh, P.; Liao, P.; Bury, W.; Wagner, G. W.; Hall, M. G.; Decoste, J. B.; Peterson, G. W.; et al. Destruction of Chemical Warfare Agents Using Metal-Organic Frameworks. Nat. Mater. 2015, 14 (5), 512−516.

(47) Belmabkhout, Y.; Zhang, Z.; Adil, K.; Bhatt, P. M.; Cadiau, A.; Solovyeva, V.; Xing, H.; Eddaoudi, M. Hydrocarbon Recovery Using Ultra-Microporous Fluorinated MOF Platform with and without Uncoordinated Metal Sites: I- Structure Properties Relationships for C2H2/C2H4 and CO2/C2H2 Separation. Chem. Eng. J. 2019, 359, 32−36.

(48) Yang, D.; Gates, B. C. Catalysis by Metal Organic Frameworks: Perspective and Suggestions for Future Research. ACS Catal. 2019, 9 (3), 1779−1798.

(49)Xue,D.X.;Cadiau,A.;Weselinski,Ł.J.;Jiang,H.;Bhatt,P.M.; Shkurenko, A.; Wojtas, L.; Zhijie, C.; Belmabkhout, Y.; Adil, K.; et al. Topology Meets MOF Chemistry for Pore-Aperture Fine Tuning: Ftw -MOF Platform for Energy-Efficient Separations: Via Adsorption Kinetics or Molecular Sieving. Chem. Commun. 2018, 54 (49), 6404− 6407.

(50) Campbell, M. G.; Liu, S. F.; Swager, T. M.; Dincă, M. Chemiresistive Sensor Arrays from Conductive 2D Metal-Organic Frameworks. J. Am. Chem. Soc. 2015, 137 (43), 13780−13783.

(51) Mohideen, M. I. H.; Belmabkhout, Y.; Bhatt, P. M.; Shkurenko, A.; Chen, Z.; Adil, K.; Eddaoudi, M. Upgrading Gasoline to High Octane Numbers Using a Zeolite-like Metal-Organic Framework Molecular Sieve with Ana -Topology. Chem. Commun. 2018, 54 (68), 9414−9417.

(52) Woellner, M.; Hausdorf, S.; Klein, N.; Mueller, P.; Smith, M. W.; Kaskel, S. Adsorption and Detection of Hazardous Trace Gases by Metal−Organic Frameworks. Adv. Mater. 2018, 30 (37), 1704679.

(53) Bobbitt, N. S.; Mendonca, M. L.; Howarth, A. J.; Islamoglu, T.; Hupp, J. T.; Farha, O. K.; Snurr, R. Q. Metal-Organic Frameworks for the Removal of Toxic Industrial Chemicals and Chemical Warfare Agents. Chem. Soc. Rev. 2017, 46 (11), 3357−3385.

(54) Barea, E.; Montoro, C.; Navarro, J. A. R. Toxic Gas Removal- Metal-Organic Frameworks for the Capture and Degradation of Toxic Gases and Vapours. Chem. Soc. Rev. 2014, 43 (16), 5419−5430.

(55) Decoste, J. B.; Peterson, G. W. Metal-Organic Frameworks for Air Purification of Toxic Chemicals. Chem. Rev. 2014, 114 (11), 5695− 5727.

(56) Britt, D.; Tranchemontagne, D.; Yaghi, O. M. Metal-Organic Frameworks with High Capacity and Selectivity for Harmful Gases. Proc. Natl. Acad. Sci. U. S. A. 2008, 105 (33), 11623−11627.

(57) Bavykina, A.; Kolobov, N.; Khan, I. S.; Bau, J. A.; Ramirez, A.; Gascon, J. Metal-Organic Frameworks in Heterogeneous Catalysis: Recent Progress, New Trends, and Future Perspectives. Chem. Rev. 2020, 120 (16), 8468−8535.

(58) Rezaei, F. A.; Rownaghi, A.; Monjezi, S. P.; Lively, R. W.; Jones, C. SOx/NO_x Removal from Flue Gas Streams by Solid Adsorbents: A Review of Current Challenges and Future Directions. Energy Fuels 2015, 29 (9), 5467−5486.

(59) Han, L.; Cai, S.; Gao, M.; Hasegawa, J. Y.; Wang, P.; Zhang, J.; Shi, L.; Zhang, D. Selective Catalytic Reduction of NO_x with NH3 by Using Novel Catalysts: State of the Art and Future Prospects. Chem. Rev. 2019, 119 (19), 10916−10976.

(60) Hu, M. M.; Zhang, Z.; Atkinson, J. D.; Rood, M. J.; Song, L.; Zhang, Z. Porous Materials for Steady-State NO Conversion: Comparisons of Activated Carbon Fiber Cloths, Zeolites and Metal- Organic Frameworks. Chem. Eng. J. 2019, 360, 89−96.

(61) Liu, Y.; Zhao, J.; Lee, J. M. Conventional and New Materials for Selective Catalytic Reduction (SCR) of NO_x. ChemCatChem. 2018, 10 (7), 1499−1511.

(62) Tang, F.; Zhao, J. C.-G.; Chen, B. Porous Coordination Polymers for Heterogeneous Catalysis. Curr. Org. Chem. 2018, 22 (18), 1773− 1791.

(63) Gong, Z.; Niu, S.-L.; Zhang, Y.-j.; Lu, C.-m. Facile Synthesis of Porous α-Fe2O3 Nanostructures from MIL-100(Fe) via Sacrificial Templating Method, as Efficient Catalysts for NH3-SCR Reaction. Mater. Res. Bull. 2020, 123, 110693.

(64) Lee, J.; Kwak, S. Y. Mn-Doped Maghemite (γ-Fe2O3) from Metal-Organic Framework Accompanying Redox Reaction in a Bimetallic System: The Structural Phase Transitions and Catalytic Activity toward NO_x Removal. ACS Omega 2018, 3 (3), 2634−2640.

(65) Keefer, L. K. Fifty Years of Diazeniumdiolate Research. from Laboratory Curiosity to Broad-Spectrum Biomedical Advances. ACS Chem. Biol. 2011, 6 (11), 1147−1155.

(66) Chui, S. S. Y.; Lo, S. M. F.; Charmant, J. P. H.; Orpen, A. G.; Williams, I. D. A Chemically Functionalizable Nanoporous Material [Cu3(TMA)2 (H2O)3](N). Science (80-.). 1999, 283 (5405), 1148− 1150.

(67) Xiao, B.; Wheatley, P. S.; Zhao, X.; Fletcher, A. J.; Fox, S.; Rossi, A. G.; Megson, I. L.; Bordiga, S.; Regli, L.; Thomas, K. M.; et al. High- CapacityHydrogenandNitricOxideAdsorptionandStorageina Metal-Organic Framework. J. Am. Chem. Soc. 2007, 129 (5), 1203− 1209.

(68) Huang, Y.; Su, W.; Wang, R.; Zhao, T. Removal of Typical Industrial Gaseous Pollutants: From Carbon, Zeolite, and Metal- Organic Frameworks to Molecularly Imprinted Adsorbents. Aerosol Air Qual. Res. 2019, 19 (9), 2130−2150.

(69) Bordiga, S.; Regli, L.; Bonino, F.; Groppo, E.; Lamberti, C.; Xiao, B.; Wheatley, P. S.; Morris, R. E.; Zecchina, A. Adsorption Properties of HKUST-1 toward Hydrogen and Other Small Molecules Monitored by IR. Phys. Chem. Chem. Phys. 2007, 9 (21), 2676−2685.

(70) Dietzel, P. D. C.; Panella, B.; Hirscher, M.; Blom, R.; Fjellvåg, H. Hydrogen Adsorption in a Nickel Based Coordination Polymer with Open Metal Sites in the Cylindrical Cavities of the Desolvated Framework. Chem. Commun. 2006, 1 (9), 959−961.

(71) Bonino, F.; Chavan, S.; Vitillo, J. G.; Groppo, E.; Agostini, G.; Lamberti, C.; Dietzel, P. D. C.; Prestipino, C.; Bordiga, S. Local Structure of CPO-27-Ni Metallorganic Framework upon Dehydration and Coordination of NO. Chem. Mater. 2008, 20 (15), 4957−4968.

(72) McKinlay, A. C.; Xiao, B.; Wragg, D. S.; Wheatley, P. S.; Megson, I. L.; Morris, R. E. Exceptional Behavior over the Whole Adsorption- Storage-Delivery Cycle for NO in Porous Metal Organic Frameworks. J. Am. Chem. Soc. 2008, 130 (31), 10440−10444.

(73) Xiao, B.; Byrne, P. J.; Wheatley, P. S.; Wragg, D. S.; Zhao, X.; Fletcher, A. J.; Thomas, K. M.; Peters, L.; Evans, J. S. O.; Warren, J. E.; et al. Chemically Blockable Transformation and Ultraselective Low- Pressure Gas Adsorption in a Non-Porous Metal Organic Framework. Nat. Chem. 2009, 1 (4), 289−294.

(74) Miller, S. R.; Alvarez, E.; Fradcourt, L.; Devic, T.; Wuttke, S.; Wheatley, P. S.; Steunou, N.; Bonhomme, C.; Gervais, C.; Laurencin, D.; et al. A Rare Example of a Porous Ca-MOF for the Controlled Release of Biologically Active NO. Chem. Commun. 2013, 49 (71), 7773−7775.

(75) Mellot-Draznieks, C.; Serre, C.; Surblé, S.; Audebrand, N.; Férey, G. Very Large Swelling in Hybrid Frameworks: A Combined Computational and Powder Diffraction Study. J. Am. Chem. Soc. 2005, 127 (46), 16273−16278.

(76) McKinlay, A. C.; Eubank, J. F.; Wuttke, S.; Xiao, B.; Wheatley, P. S.; Bazin, P.; Lavalley, J. C.; Daturi, M.; Vimont, A.; De Weireld, G.; et al. Nitric Oxide Adsorption and Delivery in Flexible MIL-88(Fe) Metal-Organic Frameworks. Chem. Mater. 2013, 25 (9), 1592−1599.

(77) Latroche, M.; Surble, S.; Serre, C.; Mellot-Draznieks, C.; Llewellyn, P. L.; Lee, J.-H.; Chang, J.-S.; Jhung, S. H.; Ferey, G. Hydrogen Storage in the Giant-Pore Metal-Organic Frameworks MIL- 100 and MIL-101. Angew. Chemie - Int. Ed. 2006, 45 (48), 8227−8231.

(78) Chevreau, H.; Permyakova, A.; Nouar, F.; Fabry, P.; Livage, C.; Ragon, F.; Garcia-Marquez, A.; Devic, T.; Steunou, N.; Serre, C.; et al. Synthesis of the Biocompatible and Highly Stable MIL-127(Fe): From Large Scale Synthesis to Particle Size Control. CrystEngComm 2016, 18 (22), 4094−4101.

(79) Eubank, J. F.; Wheatley, P. S.; Lebars, G.; McKinlay, A. C.; Leclerc, H.; Horcajada, P.; Daturi, M.; Vimont, A.; Morris, R. E.; Serre, C. Porous, Rigid Metal(III)-Carboxylate Metal-Organic Frameworks for the Delivery of Nitric Oxide. APL Mater. 2014, 2 (12), 124112.

(80) Khan, A. H.; Barth, B.; Hartmann, M.; Haase, J.; Bertmer, M. Nitric Oxide Adsorption in MIL-100(Al) MOF Studied by Solid-State NMR. J. Phys. Chem. C 2018, 122 (24), 12723−12730.

(81) Khan, A. H.; Peikert, K.; Hoffmann, F.; Fröba, M.; Bertmer, M. Nitric Oxide Adsorption in Cu 3 Btc 2 -Type MOFs - Physisorption and Chemisorption as NONOates. J. Phys. Chem. C 2019, 123 (7), 4299− 4307.

(82) Mendt, M.; Barth, B.; Hartmann, M.; Pöppl, A. Lowerature Binding of NO Adsorbed on MIL-100(Al) - A Case Study for the Application of High Resolution Pulsed EPR Methods and DFT Calculations. J. Chem. Phys. 2017, 147 (22), 224701.

(83) Haikal, R. R.; Hua, C.; Perry, J. J.; O'Nolan, D.; Syed, I.; Kumar, A.; Chester, A. H.; Zaworotko, M. J.; Yacoub, M. H.; Alkordi, M. H. Controlling the Uptake and Regulating the Release of Nitric Oxide in Microporous Solids. ACS Appl. Mater. Interfaces 2017, 9 (50), 43520− 43528.

(84) Barth, B.; Mendt, M.; Pöppl, A.; Hartmann, M. Adsorption of Nitric Oxide in Metal-Organic Frameworks: Low Temperature IR and EPR Spectroscopic Evaluation of the Role of Open Metal Sites. Microporous Mesoporous Mater. 2015, 216, 97−110.

(85) Jensen, S.; Tan, K.; Feng, L.; Li, J.; Zhou, H. C.; Thonhauser, T. Porous Ti-MOF-74 Framework as a Strong-Binding Nitric Oxide Scavenger. J. Am. Chem. Soc. 2020, 142 (39), 16562−16568.

(86) Chen, K. J.; Yang, Q. Y.; Sen, S.; Madden, D. G.; Kumar, A.; Pham, T.; Forrest, K. A.; Hosono, N.; Space, B.; Kitagawa, S.; et al. Efficient CO2 Removal for Ultra-Pure CO Production by Two Hybrid Ultramicroporous Materials. Angew. Chemie - Int. Ed. 2018, 57 (13), 3332−3336.

(87) Ingleson, M. J.; Heck, R.; Gould, J. A.; Rosseinsky, M. J. Nitric Oxide Chemisorption in a Postsynthetically Modified Metal-Organic Framework. Inorg. Chem. 2009, 48 (21), 9986−9988.

(88) Nguyen, J. G.; Tanabe, K. K.; Cohen, S. M. Postsynthetic Diazeniumdiolate Formation and NO Release from MOFs. CrystEng- Comm 2010, 12 (8), 2335−2338.

(89) Lowe, A.; Chittajallu, P.; Gong, Q.; Li, J.; Balkus, K. J. Storage and Delivery of Nitric Oxide via Diazeniumdiolated Metal Organic Framework. Microporous Mesoporous Mater. 2013, 181, 17−22.

(90) Levasseur, B.; Petit, C.; Bandosz, T. J. Reactive Adsorption of NO2 on Copper-Based Metal-Organic Framework and Graphite Oxide/Metal-Organic Framework Composites. ACS Appl. Mater. Interfaces 2010, 2 (12), 3606−3613.

(91) Ebrahim, A. M.; Levasseur, B.; Bandosz, T. J. Interactions of NO2 with Zr-Based MOF: Effects of the Size of Organic Linkers on NO2 Adsorption at Ambient Conditions. Langmuir 2013, 29 (1), 168−174.

(92) Ebrahim, A. M.; Bandosz, T. J. Ce(III) Doped Zr-Based MOFs as Excellent NO2 Adsorbents at Ambient Conditions. ACS Appl. Mater. Interfaces 2013, 5 (21), 10565−10573.

(93) Ebrahim, A. M.; Bandosz, T. J. Effect of Amine Modification on the Properties of Zirconium-Carboxylic Acid Based Materials and Their Applications as NO2 Adsorbents at Ambient Conditions. Microporous Mesoporous Mater. 2014, 188 (2), 149−162.

(94) DeCoste, J. B.; Demasky, T. J.; Katz, M. J.; Farha, O. K.; Hupp, J. T. A UiO-66 Analogue with Uncoordinated Carboxylic Acids for the Broad-Spectrum Removal of Toxic Chemicals. New J. Chem. 2015, 39 (4), 2396−2399.

(95) Bhattacharyya, S.; Han, R.; Joshi, J. N.; Zhu, G.; Lively, R. P.; Walton, K. S.; Sholl, D. S.; Nair, S. Stability of Zeolitic Imidazolate Frameworks in NO 2. J. Phys. Chem. C 2019, 123 (4), 2336−2346.

(96) Peterson, G. W.; Mahle, J. J.; Decoste, J. B.; Gordon, W. O.; Rossin, J. A. Extraordinary NO2 Removal by the Metal-Organic Framework UiO-66-NH2. Angew. Chemie - Int. Ed. 2016, 55 (21), 6235−6238.

(97) Yang, S.; Sun, J.; Ramirez-Cuesta, A. J.; Callear, S. K.; David, W. I. F.; Anderson, D. P.; Newby, R.; Blake, A. J.; Parker, J. E.; Tang, C. C.; et al. Selectivity and Direct Visualization of Carbon Dioxide and Sulfur Dioxide in a Decorated Porous Host. Nat. Chem. 2012, 4 (11), 887− 894.

(98) Han, X.; Godfrey, H. G. W.; Briggs, L.; Davies, A. J.; Cheng, Y.; Daemen, L. L.; Sheveleva, A. M.; Tuna, F.; McInnes, E. J. L.; Sun, J.; et al. Reversible Adsorption of Nitrogen Dioxide within a Robust Porous Metal−Organic Framework. Nat. Mater. 2018, 17 (8), 691− 696.

(99) Thomas-Hillman, I.; Stevens, L. A.; Lange, M.; Möllmer, J.; Lewis, W.; Dodds, C.; Kingman, S. W.; Laybourn, A. Developing a Sustainable Route to Environmentally Relevant Metal-Organic Frame- works: Ultra-Rapid Synthesis of MFM-300(Al) Using Microwave Heating. Green Chem. 2019, 21 (18), 5039−5045.

(100) Han, X.; Hong, Y.; Ma, Y.; Lu, W.; Li, J.; Lin, L.; Sheveleva, A. M.; Tuna, F.; McInnes, E. J. L.; Dejoie, C.; et al. Adsorption of Nitrogen Dioxide in a Redox-Active Vanadium Metal-Organic Framework Material. J. Am. Chem. Soc. 2020, 142 (36), 15235−15239.

(101) Sava Gallis, D. F.; Vogel, D. J.; Vincent, G. A.; Rimsza, J. M.; Nenoff, T. M. NO_x Adsorption and Optical Detection in Rare Earth Metal-Organic Frameworks. ACS Appl. Mater. Interfaces 2019, 11 (46), 43270−43277.

(102) Wang, P.; Zhao, H.; Sun, H.; Yu, H.; Chen, S.; Quan, X. Porous Metal-Organic Framework MIL-100(Fe) as an Efficient Catalyst for the Selective Catalytic Reduction of NO_x with NH3. RSC Adv. 2014, 4 (90), 48912−48919.

(103) Zhang, W.; Shi, Y.; Li, C.; Zhao, Q.; Li, X. Synthesis of Bimetallic MOFs MIL-100(Fe-Mn) as an Efficient Catalyst for Selective Catalytic Reduction of $NO_x$with NH3. Catal. Lett. 2016, 146 (10), 1956−1964.

(104) Wang, P.; Sun, H.; Quan, X.; Chen, S. Enhanced Catalytic Activity over MIL-100(Fe) Loaded Ceria Catalysts for the Selective Catalytic Reduction of NO_x with NH3 at Low Temperature. J. Hazard. Mater. 2016, 301 (2), 512−521.

(105) Sun, H.; Liu, Z.; Wang, Y.; Quan, X.; Zhao, G. Novel Metal- Organic Framework Supported Manganese Oxides for the Selective Catalytic Reduction of NO_x with NH3: Promotional Role of the Support. J. Hazard. Mater. 2019, 380 (June), 120800.

(106) Jiang, H.; Wang, Q.; Wang, H.; Chen, Y.; Zhang, M. Temperature Effect on the Morphology and Catalytic Performance of Co-MOF-74 in Low-Temperature NH3-SCR Process. Catal. Commun. 2016, 80 (x), 24−27.

(107) Jiang, H.; Wang, Q.; Wang, H.; Chen, Y.; Zhang, M. MOF-74 as an Efficient Catalyst for the Low-Temperature Selective Catalytic Reduction of NO_x with NH3. ACS Appl. Mater. Interfaces 2016, 8 (40), 26817−26826.

(108) Jiang, H.; Zhou, J.; Wang, C.; Li, Y.; Chen, Y.; Zhang, M. Effect of Cosolvent and Temperature on the Structures and Properties of Cu- MOF-74 in Low-Temperature NH3-SCR. Ind. Eng. Chem. Res. 2017, 56 (13), 3542−3550.

(109) Jiang, H.; Niu, Y.; Wang, Q.; Chen, Y.; Zhang, M. Single-Phase SO2-Resistant to Poisoning Co/Mn-MOF-74 Catalysts for NH3-SCR. Catal. Commun. 2018, 113 (May), 46−50.

(110) Wang, S.; Gao, Q.; Dong, X.; Wang, Q.; Niu, Y.; Chen, Y.; Jiang, H. Enhancing the Water Resistance of Mn-MOF-74 by Modification in Low Temperature NH3-SCR. Catalysts 2019, 9 (12), 1004.

(111) Xie, S.; Qin, Q.; Liu, H.; Jin, L.; Wei, X.; Liu, J.; Liu, X.; Yao, Y.; Dong, L.; Li, B. MOF-74-M (M = Mn, Co, Ni, Zn, MnCo, MnNI, and MnZn) for Low-Temperature NH3-SCR and in Situ Drifts Study Reaction Mechanism. ACS Appl. Mater. Interfaces 2020, 12 (43), 48476−48485.

(112) Li, C.; Shi, Y.; Zhang, H.; Zhao, Q.; Xue, F.; Li, X. Cu-BTC Metal-Organic Framework as a Novel Catalyst for Low Temperature Selective Catalytic Reduction (SCR) of NO by NH3: Promotional Effect of Activation Temperature. Integr. Ferroelectr. 2016, 172 (1), 169−179.

(113) Jiang, H.; Wang, S.; Wang, C.; Chen, Y.; Zhang, M. Selective Catalytic Reduction of NO_x with NH3 on Cu-BTC-Derived Catalysts: Influence of Modulation and Thermal Treatment. Catal. Surv. from Asia 2018, 22 (2), 95−104.

(114) Yao, Z.; Qu, D.; Guo, Y.; Yang, Y.; Huang, H. Fabrication and Characteristics of Mn@ $Cu_3(BTC)_2$ for Low-Temperature Catalytic Reduction of NOx with NH_3. Adv. Mater. Sci. Eng. 2019, 2019, 1−10.

(115) Świrk, K.; Delahay, G.; Zaki, A.; Adil, K.; Cadiau, A. Facile Modifications of HKUST-1 by V, Nb and Mn for Low-Temperature Selective Catalytic Reduction of Nitrogen Oxides by NH3. Catal. Today 2022, 384-386, 25−32.

(116) Świrk, K.; Delahay, G.; Zaki, A.; Adil, K.; Cadiau, A. Investigation of Mn Promotion on HKUST-1 Metal-Organic Frame- works for Low-Temperature Selective Catalytic Reduction of NO with NH3. ChemCatChem. 2021, 13 (18), 4029−4037.

(117) Gao, R.; Zhang, G.; Ru, X.; Xu, C.; Li, M.; Lin, R.; Wang, Z. Morphology Control of Metal-Organic Frameworks by Co-Compet- itive Coordination Strategy for Low-Temperature Selective Catalytic Reduction of NO with NH3. J. Solid State Chem. 2021, 297, 122031.

(118) Zhang, X.; Shen, B.; Zhang, X.; Wang, F.; Chi, G.; Si, M. A Comparative Study of Manganese-Cerium Doped Metal-Organic Frameworks Prepared: Via Impregnation and in Situ Methods in the Selective Catalytic Reduction of NO. RSC Adv. 2017, 7 (10), 5928− 5936.

(119) Zhang, M.; Huang, B.; Jiang, H.; Chen, Y. Metal-Organic Framework Loaded Manganese Oxides as Efficient Catalysts for Low- Temperature Selective Catalytic Reduction of NO with NH3. Front. Chem. Sci. Eng. 2017, 11 (4), 594−602.

(120) Sun, X.; Shi, Y.; Zhang, W.; Li, C.; Zhao, Q.; Gao, J.; Li, X. A New Type Ni-MOF Catalyst with High Stability for Selective Catalytic Reduction of NO_x with NH3. Catal. Commun. 2018, 114 (June), 104− 108.

(121) Smolders, S.; Struyf, A.; Reinsch, H.; Bueken, B.; Rhauderwiek, T.; Mintrop, L.; Kurz, P.; Stock, N.; De Vos, D. E. A Precursor Method for the Synthesis of New Ce(Iv) MOFs with Reactive Tetracarboxylate Linkers. Chem. Commun. 2018, 54 (8), 876−879.

(122) Smolders, S.; Jacobsen, J.; Stock, N.; De Vos, D. Selective Catalytic Reduction of NO by Cerium-Based Metal-Organic Frame- works. Catal. Sci. Technol. 2020, 10 (2), 337−341.

(123) Xiao, X.; Wang, J.; Jia, X.; Ma, C.; Qiao, W.; Ling, L. Low- Temperature Selective Catalytic Reduction of $NO_x$with NH3over Mn- Ce Composites Synthesized by Polymer-Assisted Deposition. ACS Omega 2021, 6 (19), 12801−12812.

(124) Mohan, S.; Dinesha, P.; Kumar, S. NO_x Reduction Behaviour in Copper Zeolite Catalysts for Ammonia SCR Systems: A Review. Chem. Eng. J. 2020, 384, 123253.

(125) Wu, Z.; Shi, Y.; Li, C.; Niu, D.; Chu, Q.; Xiong, W.; Li, X. Synthesis of Bimetallic MOF-74-CoMn Catalyst and Its Application in Selective Catalytic Reduction of NO with CO. Acta Chim. Sin. 2019, 77 (8), 758−764.

(126) Qin, Y. H.; Huang, L.; Zhang, L.; He, H. One-Step Synthesis of Confined Ion Ag x -Cu-BTC for Selective Catalytic Reduction of NO with CO. Inorg. Chem. Commun. 2019, 102, 130−133.

(127) Zhang, Y.; Zhao, L.; Duan, J.; Bi, S. Insights into DeNO_x Processing over Ce-Modified Cu-BTC Catalysts for the CO-SCR Reaction at Low Temperature by in Situ DRIFTS. Sep. Purif. Technol. 2020, 234, 116081.

(128) Wang, Y.; Zhang, L.; Li, R.; He, H.; Wang, H.; Huang, L. MOFs- Based Coating Derived Me-ZIF-67@CuOx Materials as Low-Temper- ature NO-CO Catalysts. Chem. Eng. J. 2020, 381, 122757.

(129) Shi, Y.; Chu, Q.; Xiong, W.; Gao, J.; Huang, L.; Zhang, Y.; Ding, Y. A New Type Bimetallic NiMn-MOF-74 as an Efficient Low- Temperatures Catalyst for Selective Catalytic Reduction of NO by CO. Chem. Eng. Process. - Process Intensif. 2021, 159, 108232.

(130) Xue, Y.; Sun, W.; Wang, Q.; Cao, L.; Yang, J. Sparsely Loaded Pt/MIL-96(Al) MOFs Catalyst with Enhanced Activity for H2-SCR in a Gas Diffusion Reactor under 80°C. Chem. Eng. J. 2018, 335, 612−620.

(131) Nguyen, H. P.; Kim, T. H.; Lee, S. W. Influence of Operational Parameters on the Photocatalytic Performance of DE-NO_x Process Via MIL-101(Fe). Prog. Nat. Sci. Mater. Int. 2018, 28 (6), 689−695.

(132) Nguyen, H. P.; Matsuoka, M.; Kim, T. H.; Lee, S. W. Iron(III)- Based Metal-Organic Frameworks as Potential Visible Light-Driven Catalysts for the Removal of NO_x: A Solution for Urban Air Purification. J. Photochem. Photobiol. A Chem. 2018, 367 (July), 429− 437.

(133) Wei, X.; Wang, Y.; Huang, Y.; Fan, C. Composite ZIF-8 with CQDs for Boosting Visible-Light-Driven Photocatalytic Removal of NO. J. Alloys Compd. 2019, 802, 467−476.

(134) Chen, X.; Cai, Y.; Liang, R.; Tao, Y.; Wang, W.; Zhao, J.; Chen, X.; Li, H.; Zhang, D. NH2-UiO-66(Zr) with Fast Electron Transfer Routes for Breaking down Nitric Oxide via Photocatalysis. Appl. Catal. B Environ. 2020, 267, 118687.

Table 1. Catalytic Performance of Various MOF Catalysts Analysed in Selective Catalytic Reduction Using NH3

	NH_3 as reducing agent		
Best performing catalyst	**Reaction conditions**	**Catalytic performance**	**Ref**
MIL-100(Fe)	NO]=500ppm,[NH3]=500ppm,O2 =4vol%,totalflowrate=315 mL min−1, GHSV = 30,000 h−1	NO_x conversion above 97% from 245 to 300 °C	102
MIL-100(Fe-Mn)	[NO]=500ppm,[NH3]=500ppm,O2 =5vol%,totalflowrate=100 mL min−1, GHSV = 15,000 h−1	Max NO_x conversion of 96% at 260 °C	103
0.08IM-CeO2/MIL-100(Fe)	[NO]=500ppm,[NH3]=500ppm,O2 =4vol%,totalflowrate=315 mL min−1, GHSV = 30,000 h−1	NO_x conversion above 90% from 196 to 300 °C	104
20 wt %-MnOx@MIL-125(Ti)	[NO]=500ppm,[NH3]=500ppm,O2 =3vol%,totalflowrate=no information, GHSV = 30,000 h−1	NO_x conversion above 90% from 175 to 425 °C	105
Co-MOF-74 (dried in N2 at 300 °C)	[NO] = 1000 ppm, [NH3] = 1000 ppm, O2 = 2 vol %, total flow rate = 100 mL min−1, GHSV = 50,000 h−1	Max NO conversion of 68% at 220 °C	107
Co-MOF-74 (synthesized in isopropanol)	[NO] = 1000 ppm, [NH3] = 1000 ppm, O2 = 2 vol %, total flow rate = 100 mL min−1, GHSV = 50,000 h−1	Max NO conversion of 97.8% at 230 °C	108
Mn0.66Co0.34-MOF-74	[NO]=500ppm,[NH3]=500ppm,O2 =5vol%,totalflowrate=100 mL min−1, GHSV = 50,000 h−1	Max NO conversion of 99.3% at 200 °C	109
Mn-MOF-74	[NO] = [NH3] = 500 ppm, [O2] = 5 vol %, total flow rate = 100 mL min−1, GHSV = 50,000 h−1	NO conversion of ca. 100% from 220 to 240 °C	110
MOF-74-Mn	[NO] = [NH3] = 500 ppm, [O2] = 5 vol %, total flow rate = 100 mL min−1, WHSV = 60,000 mL h−1 g−1	Max NO conversion of 95% at 250 °	111
HKUST-1 (pretreated at 230 °C)	[NO] = [NH3] = 500 ppm, [O2] = 5 vol %, total flow rate = 100 mL min−1, GHSV = 30,000 h−1	Max NO conversion of 100% from 220 to 280°C	112
25%-AA-Cu-BTC	[NO]=[NH3]=1000ppm,[O2]=2vol%,totalflowrate=100mL min−1, GHSV = 50,000 h−1	Max NO conversion of 95.5% at 280 °C	113
Mn@Cu-BTC-0.05	[NO]=[NH3]=500ppm,[O2]=5vol%,totalflowrate=no information, GHSV = 30,000 h−1	Max NO conversion of 100% from 220 to 260 °C	114
HKUST-1-Mn	[NO]=[NH3]=1000ppm,[O2]=8vol%,totalflowrate=100mL min−1, WHSV = 80,000 mL h−1 g−1	Max NO conversion of 80% and NH_3 conversion of 100% at 185 °C	115
HKUST-1-Mn3.75	[NO]=[NH3]=1000ppm,[O2]=8vol%,totalflowrate=100mL min−1, WHSV = 96,000 mL h−1 g−1	NO conversion of 68% and NH_3 conversion of 65% at 185 °C	116
HKUST-1-T	[NO] = [NH3] = 0.1%, [O2] = 5 vol %, total flow rate = 1250 mL min−1, WHSV = 50,000 mL h−1 g−1	NO conversion of 93% at 240 °C	117
MnCe@MOF (Mn-Ce-UiO-67)	[NO] = [NH3] = 500 ppm, [O2] = 5 vol %, total flow rate = 450 mL min−1, GHSV = 45,000 h−1	NO conversion of 98% from 200 to 300 °C	118
Mn-UiO-66	[NO]=500ppm,[NH3]=500ppm,O2 =5vol%,totalflowrate=100 mL min−1, GHSV = 50,000 h−1	NO conversion 90% from 100 and 290 °C	80
Ni-MOF (pretreated at 220 °C)	[NO]=500ppm,[NH3]=500ppm,O2 =5vol%,totalflowrate=100 mL min−1, GHSV = 15,000 h−1	NO conversion of 92% from 275 to 440 °C	120
Ce-UiO-66	[NO]=500ppm,[NH3]=500ppm,O2 =10vol%,totalflowrate=30 mL min−1, GHSV = 9000 h−1	Max NO conversion of ca. 78% at 230 °C	122

Table 2. Catalytic Performance of Various MOF Catalysts Analysed in Selective Catalytic Reduction Using CO

CO as reducing agent

Best performing catalyst	Reaction conditions	Catalytic performance	Ref
MOF-74-Co1Mn2	[NO] = 500 ppm, [CO] = 1000 ppm, total flow rate = 200 mL min^{-1}, GHSV = 30,000 h^{-1}	NO conversion 100% from 175 to 275 °C	125
Ag0.5-Cu-BTC		NO conversion of 100% from 238 to 280 °C	126
Ce-Cu-BTC	[NO] = 1000 ppm, [CO] = 1000 ppm, [O_2] = 5 vol %, total flow rate = no information, GHSV = no information	NO conversion of 91% at 250 °C	127
Al-ZIF-67@CuOx	[NO] = 300 ppm, [CO] = 900 ppm, total flow rate = no information, GHSV = no information	NO conversion of 99% at 200 °C	128
Ni0.65Mn0.35-MOF-74	[NO] = 500 ppm, [CO] = 1000 ppm, O_2 = 10 vol %, total flow rate = no information, GHSV = 30,000 h^{-1}	Max. NO conversion of ca. 100% from 175 to 300 °C	129

Figure Caption

Figure 1. Crystal structure representation of HKUST-1 (A). Adsorption (filled symbols) and desorption (open symbols) isotherms at 196 K (squares) and 298 K (circles) for nitric oxide on HKUST-1 (B). Interaction with NO monitored by IR spectroscopy (C). Red curve: HKUST-1 outgassed at 180 °C. Blue curve: effect of 30 Torr of NO. Black curves: effect of increasing pumping, residual pressure 10−3 Torr. (Inset) Background-subtracted spectra in the region of NO stretching (same color code). In the upper part of the inset (blue dashed curve), the spectrum of NO adsorbed at room temperature on a Cu-ZSM-5 zeolite is reported for comparison. Reproduced with permission from ref 69. Copyright 2007, American Chemical Society.

Figure 2. Crystal structure of NO-loaded Co-MOF from Rietveld refinement of X-ray diffraction data. (A) Binding of NO to the CUSs in Co-MOF. The nitrogen and oxygen atoms of NO were located from difference Fourier maps. (B) Enlarged view of NO bound to the cobalt atoms in NO-loaded Co-MOF showing the bent mode of NO binding. (C) Adsorption/desorption isotherms at 25 °C for NO on Co-MOF and Ni-MOF. The hysteresis in the isotherms is typical of materials in which the NO binds relatively strongly to the metals. Reproduced with permission from ref 72. Copyright 2008, American Chemical Society.

Figure 3. Crystal structure of Cu-SIP-3.3H2O (left). Only NO (298 K) is adsorbed below ambient pressure and then only significantly above the gate- opening pressure of ~275 mbar. The desorption isotherm for NO shows the large hysteresis that indicates strong coordination of NO with metals in the framework. No adsorption is seen for CO2 (273 K), CO (298 K), H2 (77 K), and N2 (77 K) up to 10 bar (right). Reproduced with permission from ref 73. Copyright 2009, Springer Nature.

Figure 4. Crystal structure of BioMIL-3 (left). NO isotherms of BioMIL-3 at 298 K (right). Reproduced with permission from ref 74. Copyright 2013, The Royal Society of Chemistry.

Figure 5. (Top) View of the trimers from MIL-88s (left) and the constitutive linkers (middle). (Bottom) View of the structure of MIL-88B, along the c-axis, in its dried form (left), and MIL-88B in its open form (middle). NO adsorption−desorption isotherms at 303 K of selected MIL-88 samples (right). Reproduced with permission from ref 76. Copyright 2013, American Chemical Society.

Figure 6. Representation of the assembly of the rigid, porous, three-periodic MIL-100(Fe) and MIL-127(Fe). NO adsorption/desorption isotherms at 298 K of MIL-100(Cr) (top, right) and MIL-100(Fe) (bottom, right), activated at ~423 K (adsorption, open symbols; desorption, closed symbols). Reproduced with permission from ref 79. Copyright 2014, AIP Publishing.

Figure 7. (Top) Crystal structure of UiO-66-NH2 (left), crystal structure of TIFSIX-2-Cu-i (middle), and a geometrically optimized model for a tentative repeat unit in the imidazole-POP (right). (Bottom) NO sorption isotherms for the compounds studied herein (A) and the variable temperature sorption isotherms for TIFSIX-2-Cu-I (B). Reproduced with permission from ref 83. Copyright 2017, American Chemical Society.

Figure 8. Reversible NONOate formation on a secondary amine. Reproduced with permission from ref 89. Copyright 2013, Elsevier B.V.

Figure 9. (A) Space-filling diagram of the HKUST-1 framework showing the larger pore windows. (B) Cuboctahedron pore, a sphere of 15 Å inserted to emphasize the pore space. (C) Approximate dimensions of 4-map. (D) PXRD before and after each functionalization (2θ range = 5−25). (E) Scheme summarizing the adsorption protocol. Reproduced with permission from ref 87. Copyright 2009 American Chemical Society.

Figure 10. Synthesis of IRMOF-3-NONO (left) and UMCM-1- NONO (right). Reproduced with permission from ref 88. Copyright 2010, The Royal Society of Chemistry.

Figure 11. (A) Cu-TDPAT framework calculated using the crystallographic data. (B) H6TDPAT NONOate formation. (C, D) Release profile of NO from Cu-TDPAT at 85% RH vs 37 °C shown in (left) hours and (right) days. Reproduced with permission from ref 89. Copyright 2013, Elsevier B.V.

Figure 12. Synthesis of UiO-66, UiO-66-vacuum, and UiO-66-oxalate (top). ATR-FTIR spectra of UiO-66-ox exposed to SO2 and NO2 from 2000 to 600 cm−1, compared to the UiO-66-ox spectrum (bottom). Reproduced with permission from ref 94. Copyright 2015, The Royal Society of Chemistry.

Figure 13. (A) Structure of UiO-66 analogues, (B) nitration of the benzene ring, (C) diazonium ion formation, and (D) DRIFTS spectra for UiO-66- NH2 exposed to NO2 as a function of time. Reproduced with permission from ref 96. Copyright 2016, John Wiley and Sons.

Figure 14. (A, B) Views of the structural model for MFM-300(Al)·(NO2)2·(N2O)2 determined by high resolution synchrotron X-ray powder diffraction data at 298 K. (C) Adsorption isotherms of NO2 in MFM-300(Al) at 298 K. (D) Variation of the thermodynamic parameters of isosteric heat of adsorption (Qst) and entropy (ΔS) for NO2 uptakes in MFM-300(Al). Overall, ΔS decreases slowly with increasing surface coverage. Reproduced with permission from ref 98. Copyright 2018, Springer Nature.

Figure 15. (A) Stability tests of SCR reaction at 250 °C over MIL-100(Fe). Reaction conditions: 500 ppm of NO, 500 ppm of NH3, 500 ppm of SO2 (when used), 5% H2O (when used), 4% O2 and N2 balance, GHSV = 30,000 h−1 and (B) NOx conversions over

MIL-100(Fe) and V2O5−WO3/TiO2. Reaction conditions: 500 ppm of NO, 500 ppm of NH3, 4% O2 and N2 balance, GHSV = 30,000 h−1. Reproduced with permission from ref 102. Copyright 2014, The Royal Society of Chemistry.

Figure 16. (A) NO conversion to NO2 over 0.08 IM-CeO2/MIL-100(Fe), SG-CeO2/MIL-100(Fe), and MIL-100(Fe) catalysts. Reaction conditions: [NO] = 500 ppm, [O2] = 4% and N2 balance, GHSV = 30,000 h−1 and (B) NH3 oxidation over 0.08 IM-CeO2/MIL-100(Fe), SG-CeO2/MIL- 100(Fe), and MIL-100(Fe) catalysts. Reaction conditions: [NH3] = 500 ppm, [O2] = 4% and N2 balance, GHSV = 30,000 h−1. Reproduced with permission from ref 104. Copyright 2016, Elsevier B.V.

Figure 17. (A) NOx conversion as a function of temperature in the NH3-SCR reaction over MnOx@MIL-125(Ti) and MnOx/TiO2. Reaction conditions: [NH3] = 500 ppm, [NO] = 500 ppm, [O2] = 3% and N2 balance, GHSV = 30,000 h−1. (B) SO2 tolerance and 5 vol % H2O resistance over MnOx@MIL-125(Ti) at 200 °C. Reaction conditions: [NH3] = 500 ppm, [NO] = 500 ppm, [SO2] = 100 ppm (when used), [H2O] = 5% (when used), [O2] = 3% and N2 balance, GHSV= 30,000 h−1. Reproduced with permission from ref 105. Copyright 2019, Elsevier B.V.

Figure 18. (A) Stability test of SCR reaction at (a) 220 °C over Mn-MOF-74 and (B) 200 °C over Co-MOF-74. Reaction conditions: 1000 ppm of NO, 1000 ppm of NH3, 100 ppm of SO2 (when used), 5 vol % H2O (when used), 2% O2, and Ar balance. Reproduced with permission from ref 107. Copyright 2016, American Chemical Society.

Figure 19. (A) Schematic of framework dehydration for Cu-BTC (Cu, orange; O, red; C, gray; H, white; N, blue). (B) NO conversions for various Cu-BTC samples pretreated at different temperatures. Reaction conditions: [NO]□[NH3] = 500 ppm, [O2] = 5 vol %, N2 as balance gas, total gas flow rate 100 mL/min, and GHSV = 30,000 h−1.

Figure 20. (A) NO conversion measured for the MnCeMOF and MnCe@MOF catalysts. (B) Effect of SO2 and H2O on NO conversion reported for MnCe@MOF. Reproduced with permission from ref 61. Copyright 2018, John Wiley and Sons.

Figure 21. Stability tests at 200 °C over the 8.5 wt %-MnOx/UiO-66-DP catalyst. Reaction conditions: 500 ppm of NO, 500 ppm of NH3, 5.0 vol % O2, 100 ppm of SO2 (when used), 5 vol % H2O (when used), and Ar balance. Reproduced with permission from ref 119. Copyright 2017, Springer Nature.

Figure 22. Comparison of Ce10/Zr-MOFs with physical Ce-MOF/Zr-MOF mixtures: NO conversion (left) and NH3 adsorption (right). The MOFs are tested up to their thermal stability limit. The NH3 adsorption of all-Ce catalysts is also displayed as a reference. Reaction conditions: [NO] = [NH3] = 500 ppm, [O2] = 10%; 30 mL min−1 (GHSV ≈ 9000

h−1). Adsorption conditions: [NH3] = 500 ppm. Reproduced with permission from ref 122. Copyright 2020, The Royal Society of Chemistry.

Figure 23. Sparsely loaded Pt/MIL-96(Al) MOFs catalyst with enhanced activity for H2-SCR in a gas diffusion reactor under 80 °C. Reproduced with permission from ref 127. Copyright 2020, Elsevier B.V.

Figure 24. The catalytic process of Me-ZIF-67@CuO. Reproduced with permission from ref 128. Copyright 2020, Elsevier B.V.

Figure 25. (A) NO conversion over Ni1−xMnx-MOF-74 catalysts (x = 0, 0.1, 0.2, 0.35, 0.5, and 1). (B) Effects of H2O or/and SO2 on NOx conversion of Ni0.65Mn0.35-MOF-74 at 225 °C. Reproduced with permission from ref 129. Copyright 2021, Elsevier B.V.

Figure 26. (a) NO removal efficiency of MIL-96/CP and PtxMIL-96/CP. (b) NO removal efficiency of Pt5MIL-96, Pt/TiO2, Pt/SiO2, Pt/Si, and Pt/ Al2O3. Reaction conditions: [NO] = 0.1%, [H2] = 2%, [O2] = 2%, use N2 as gas. CP represents carbon paper. Reproduced with permission from ref 130. Copyright 2018, Elsevier B.V.

Figure 27. NO decrease, NOx conversion, and NO2 selectivity after 1 h photocatalytic test in the presence of MILs (Fe) under solar light (A) and UV cutoff light (B) irradiation. Reproduced with permission from ref 132. Copyright 2018, Elsevier B.V.

Figure 28. (a) Photocatalytic NO degradation efficiency of ZIF-8, P25, CQDs, and CQDs/ZIF-8 composites under visible light irradiation (l > 420 nm). (b) The corresponding NO2 yield. Reproduced with permission from ref 133. Copyright 2019, Elsevier B.V.

Figure 29. Proposed mechanism for photocatalytic NO oxidation in gas phase and hydrogen evolution in liquid phase. Reproduced with permission from ref 134. Copyright 2020, Elsevier B.V.

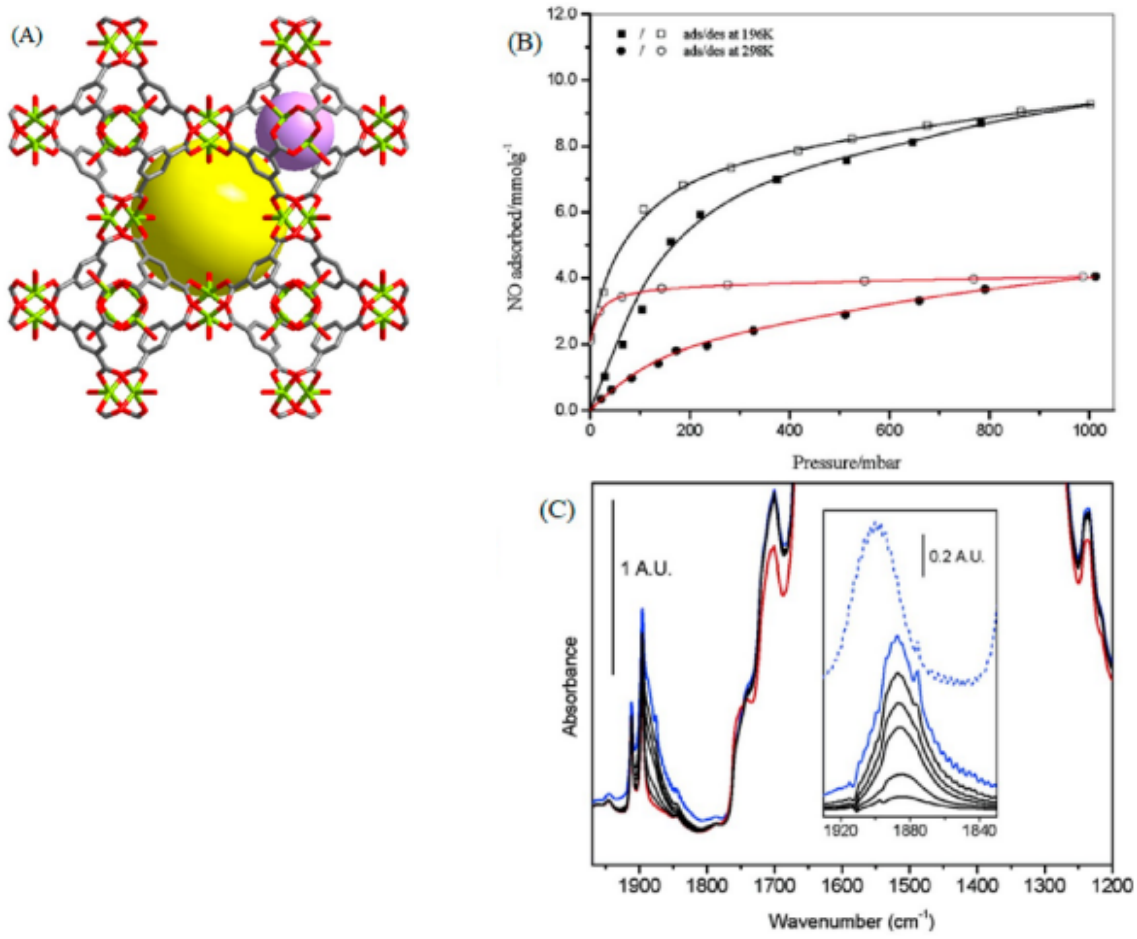
(A)
(B)
ads/des at 196K
ads/des at 298K
NO adsorbed/mmolg-1
Pressure/mbar
(C)
1 A.U.
0.2 A.U.
Absorbance
Wavenumber (cm-1)

Figure 1.

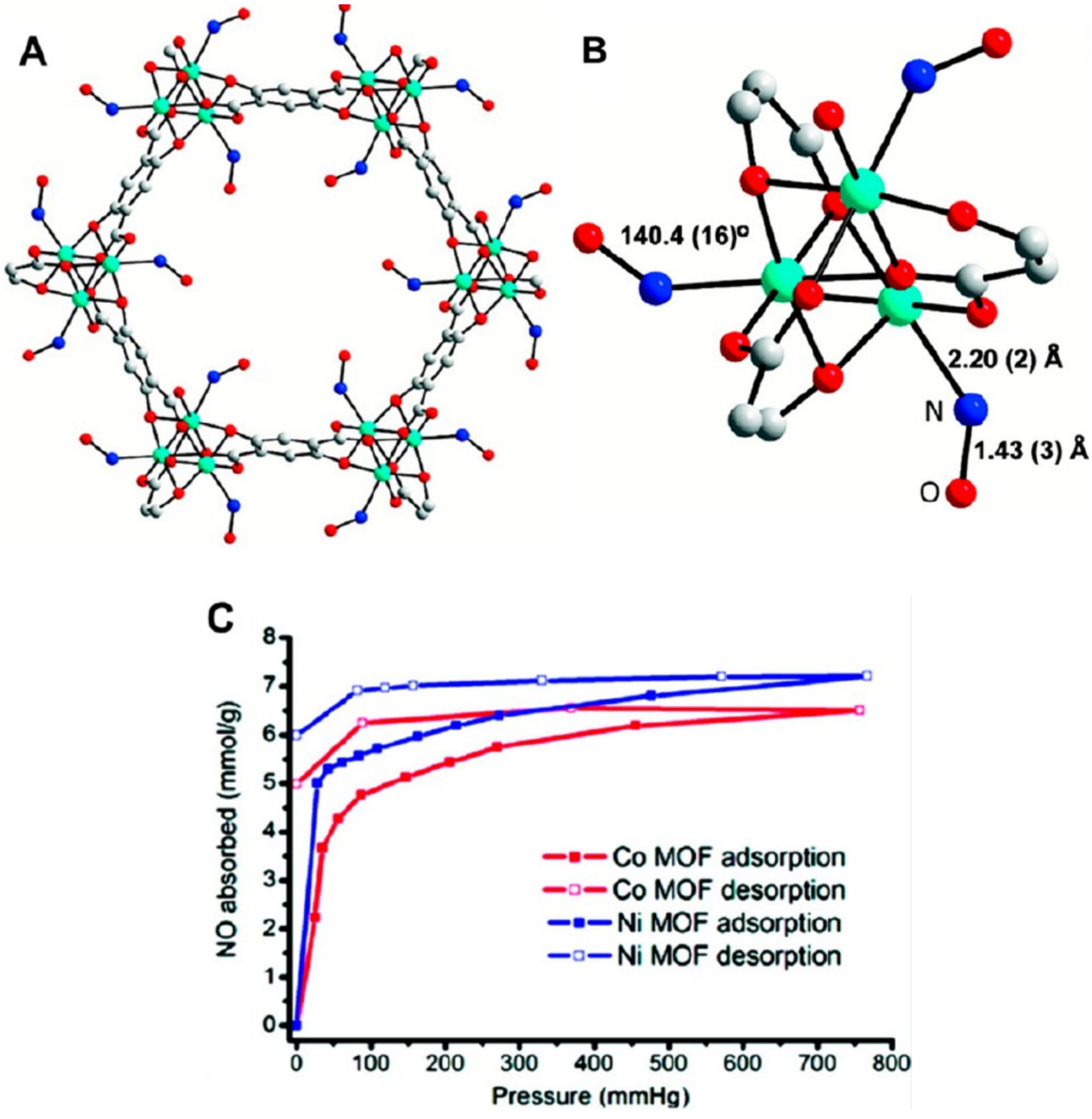
A
B
140.4 (16)°
2.20 (2) Å
N
1.43 (3) Å
O
C
NO absorbed (mmol/g)
Pressure (mmHg)
Co MOF adsorption
Co MOF desorption
Ni MOF adsorption
Ni MOF desorption

Figure 2.

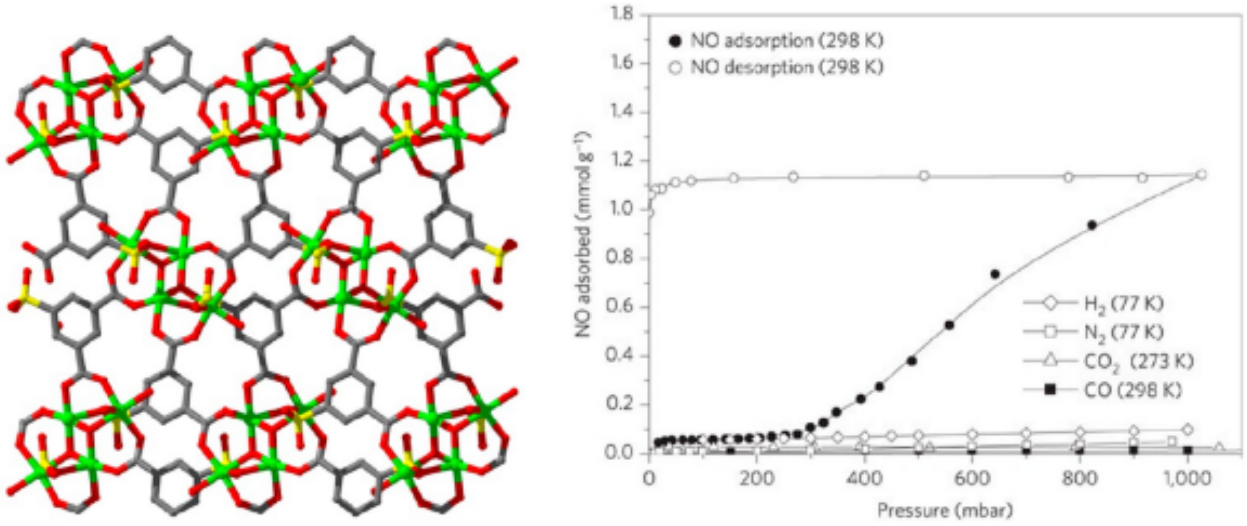
NO adsorption (298 K)
NO desorption (298 K)
NO adsorbed (mmol g⁻¹)
Pressure (mbar)
H2 (77 K)
N2 (77 K)
CO2 (273 K)
CO (298 K)
0.0
0.2
0.4
0.6
0.8
1.0
1.2
1.4
1.6
1.8
0
200
400
600
800
1,000

Figure 3.

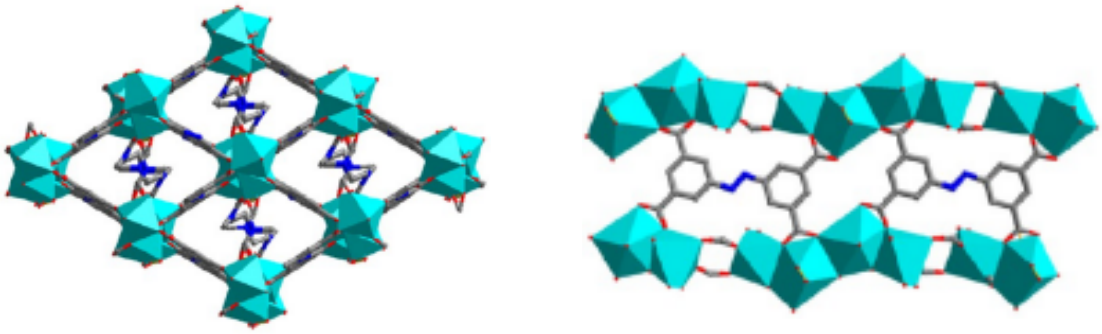

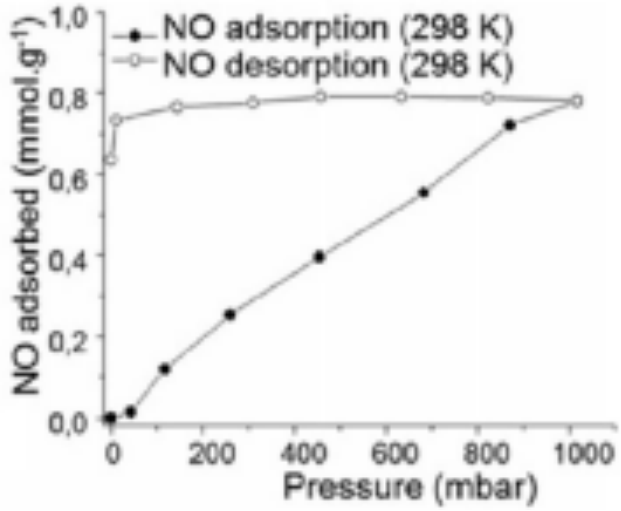
NO adsorption (298 K)
NO desorption (298 K)
NO adsorbed (mmol.g-1)
1,0
0,8
0,6
0,4
0,2
0,0
0
200
400
600
800
1000
Pressure (mbar)

Figure 4.

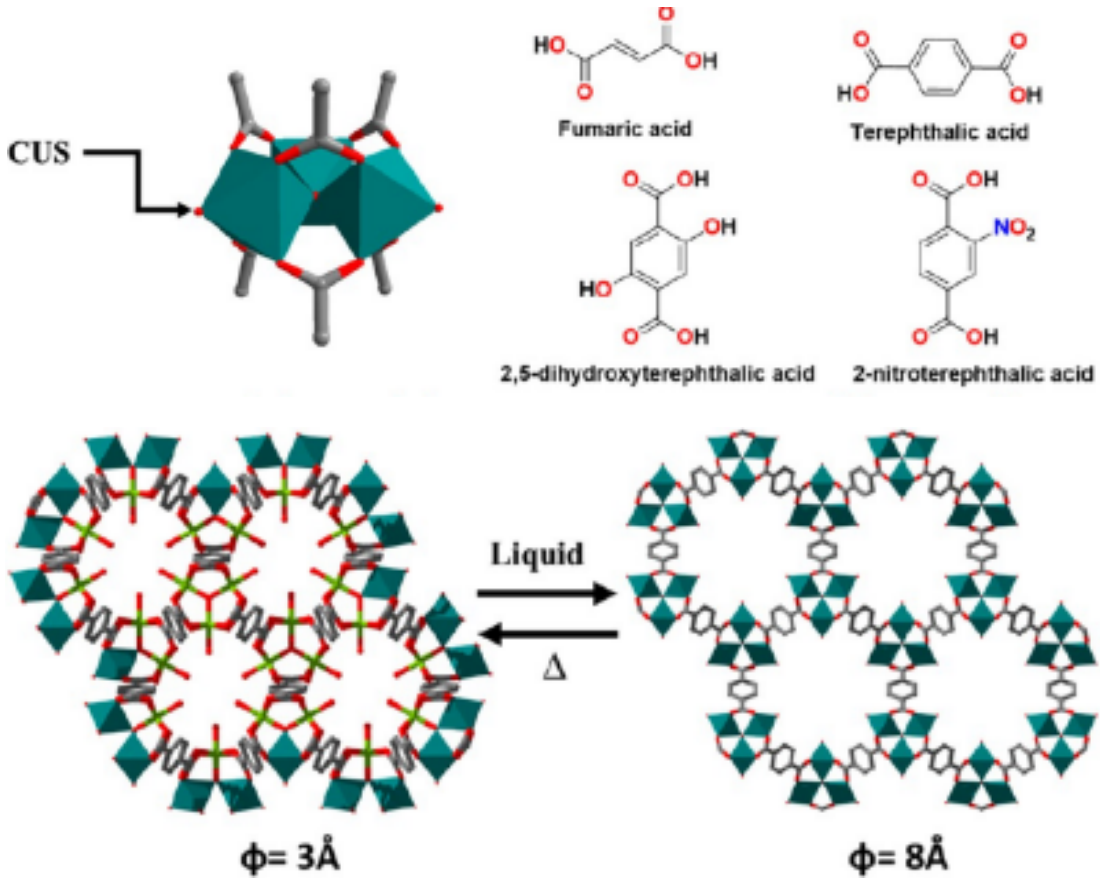
CUS
Fumaric acid
Terephthalic acid
2,5-dihydroxyterephthalic acid
2-nitroterephthalic acid
Liquid
Δ
ϕ= 3Å
ϕ= 8Å

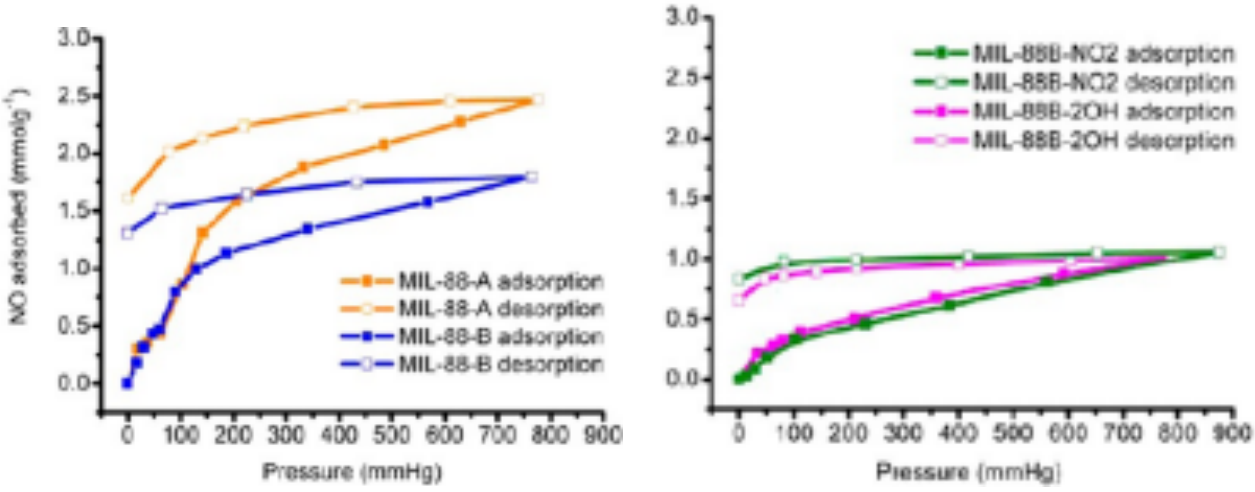
NO adsorbed (mmol/g⁻¹)
Pressure (mmHg)
MIL-88-A adsorption
MIL-88-A desorption
MIL-88-B adsorption
MIL-88-B desorption
MIL-88B-NO2 adsorption
MIL-88B-NO2 desorption
MIL-88B-2OH adsorption
MIL-88B-2OH desorption

Figure 5.

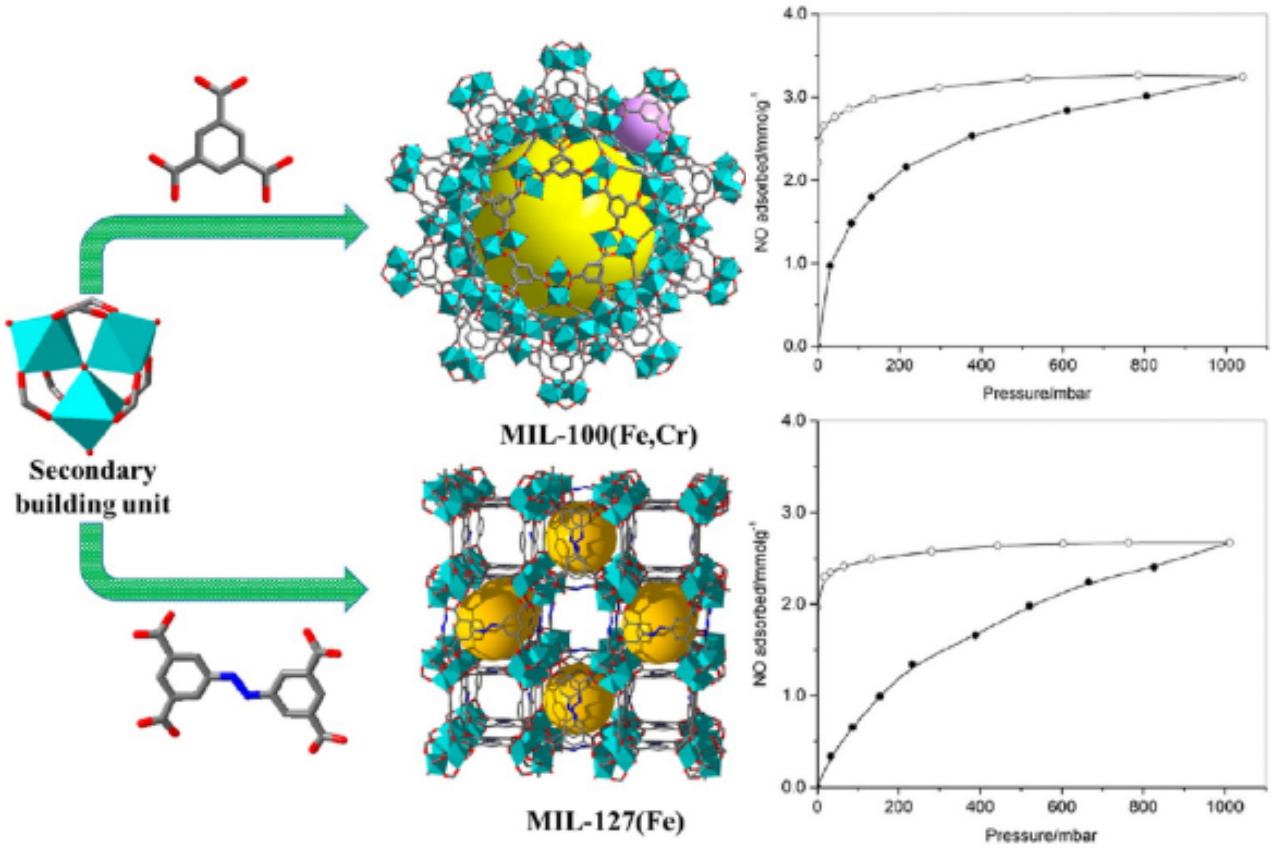
Secondary
building unit
MIL-100(Fe,Cr)
MIL-127(Fe)
NO adsorbed/mmol/g
Pressure/mbar
0.0
1.0
2.0
3.0
4.0
0
200
400
600
800
1000

Figure 6.

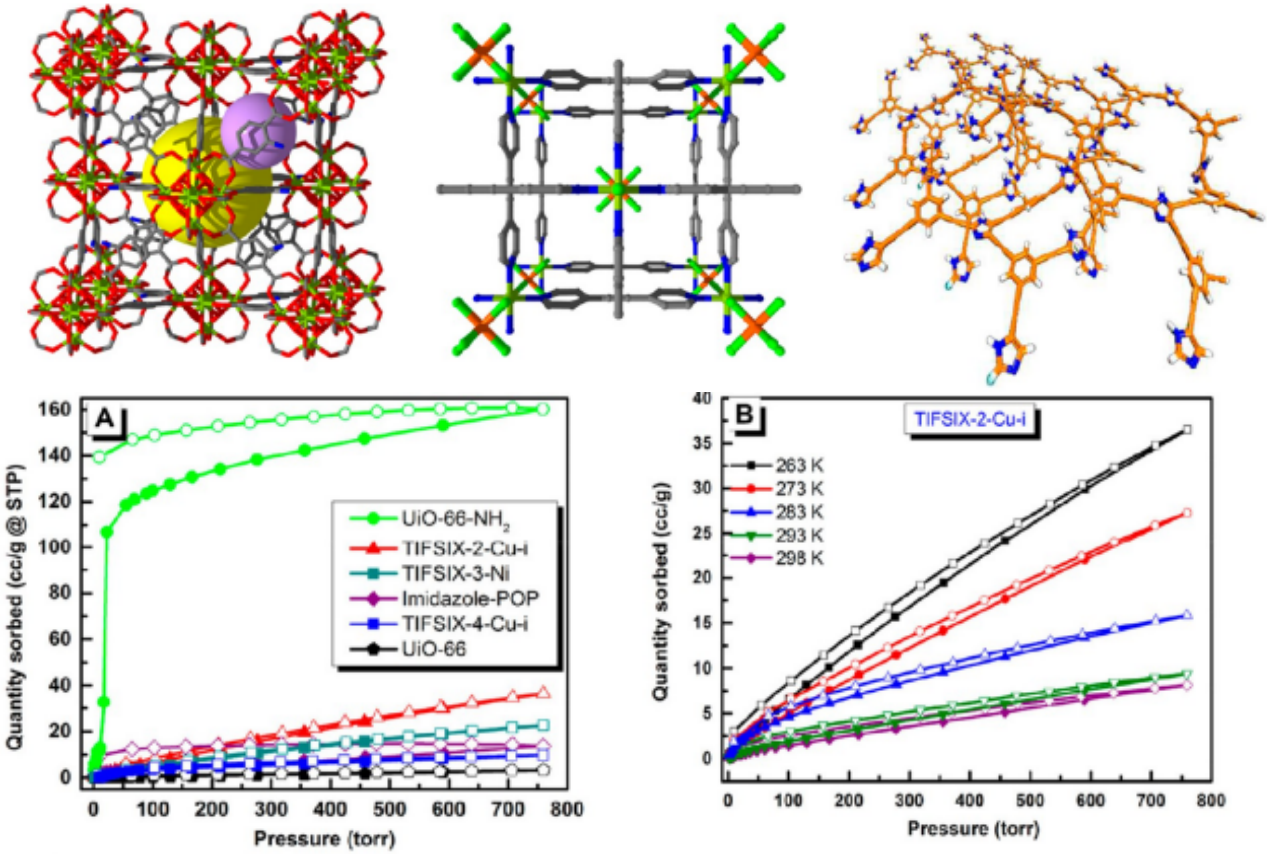
A
Quantity sorbed (cc/g @ STP)
Pressure (torr)
UiO-66-NH2
TIFSIX-2-Cu-i
TIFSIX-3-Ni
Imidazole-POP
TIFSIX-4-Cu-i
UiO-66
B
TIFSIX-2-Cu-i
263 K
273 K
283 K
293 K
298 K
Quantity sorbed (cc/g)
Pressure (torr)

Figure 7.

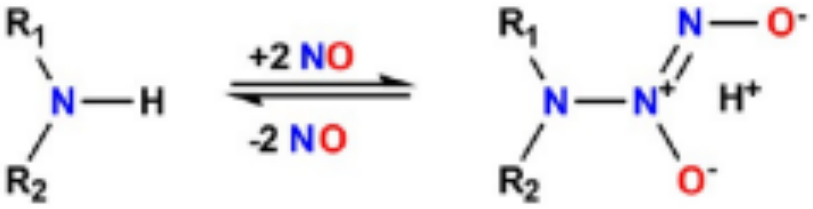

Figure 8.

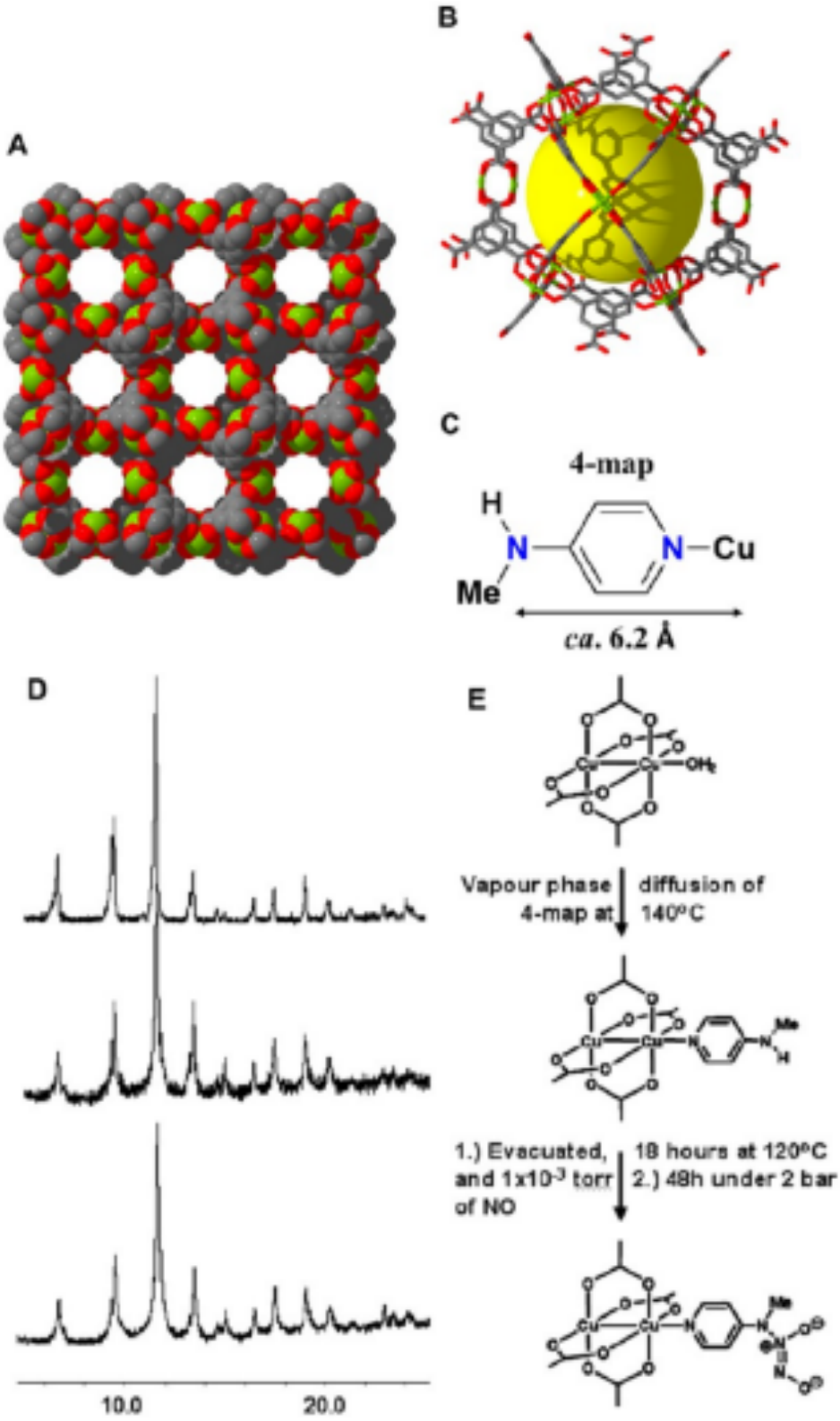
A
B
C
4-map
H
N
N
Cu
Me
ca. 6.2 Å
D
E
Vapour phase diffusion of
4-map at 140°C
1.) Evacuated,
and 1x10-3 torr
of NO
18 hours at 120°C
2.) 48h under 2 bar
10.0
20.0

Figure 9.

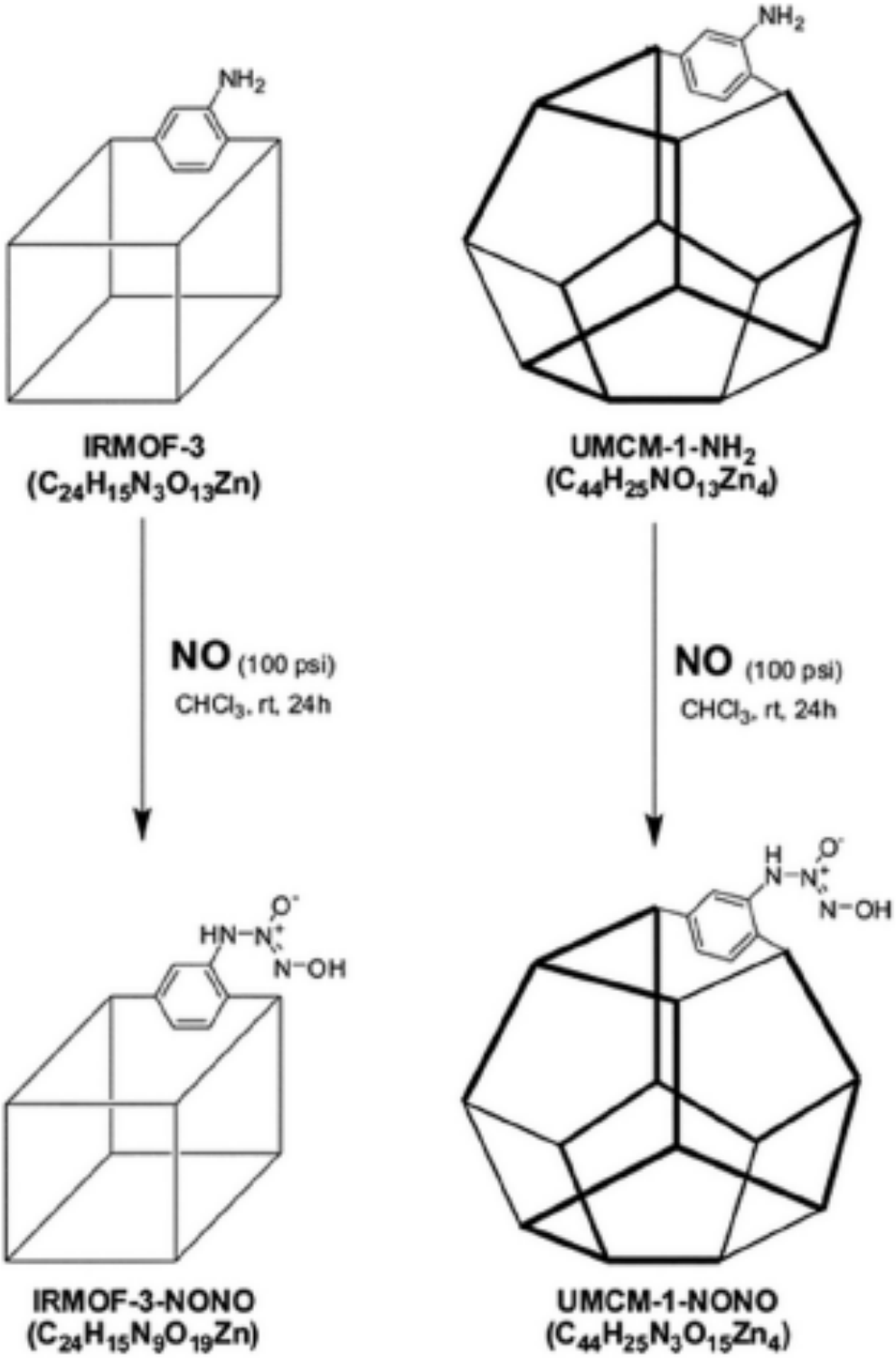
NH2
IRMOF-3
(C24H15N3O13Zn)
NO (100 psi)
CHCl3, rt, 24h
HN–N
O
N–OH
IRMOF-3-NONO
(C24H15N9O19Zn)
NH2
UMCM-1-NH2
(C44H25NO13Zn4)
NO (100 psi)
CHCl3, rt, 24h
H
N–N
O
N–OH
UMCM-1-NONO
(C44H25N3O15Zn4)

Figure 10.

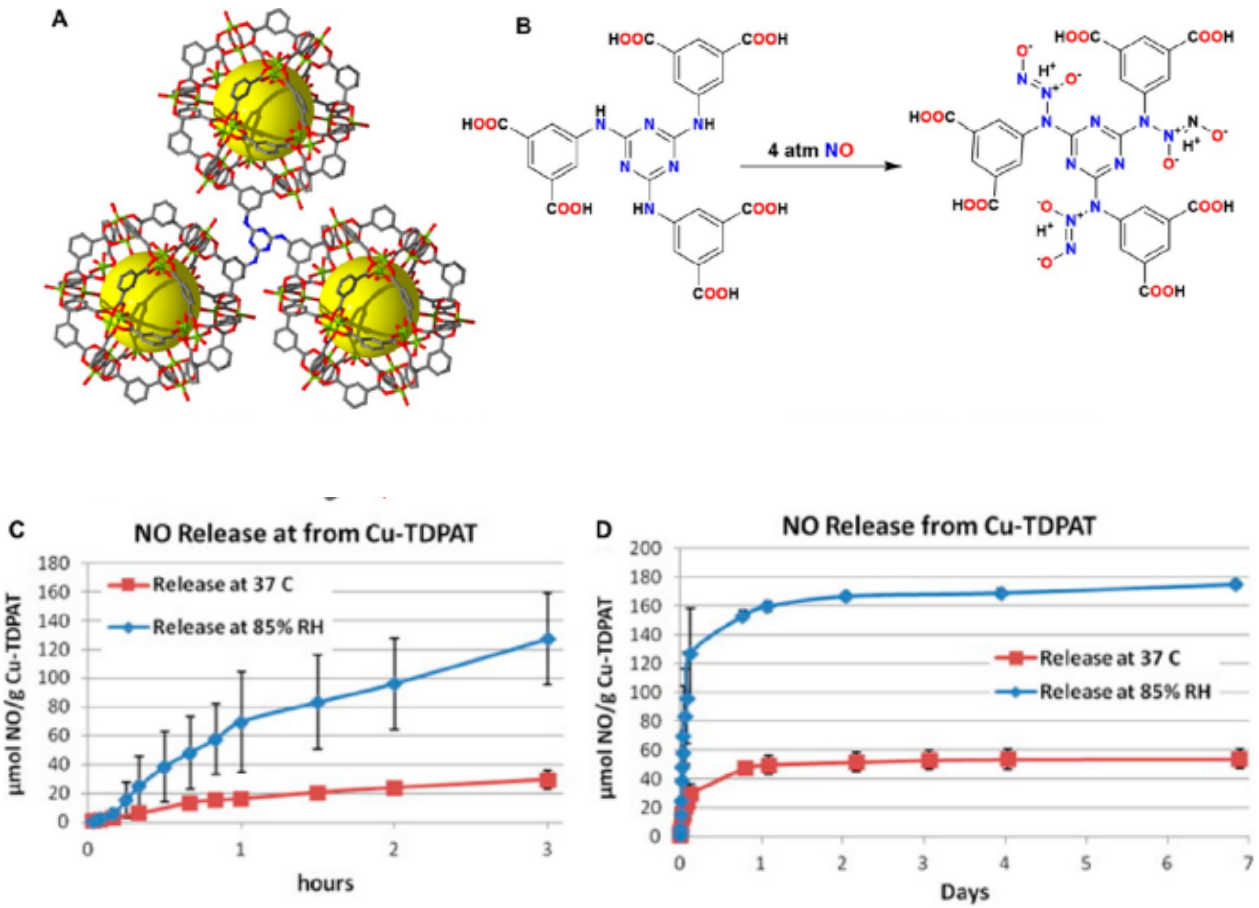
A
B
HOOC
COOH
NH
HN
4 atm NO
C
NO Release at from Cu-TDPAT
Release at 37 C
Release at 85% RH
µmol NO/g Cu-TDPAT
hours
D
NO Release from Cu-TDPAT
Release at 37 C
Release at 85% RH
µmol NO/g Cu-TDPAT
Days

Figure 11.

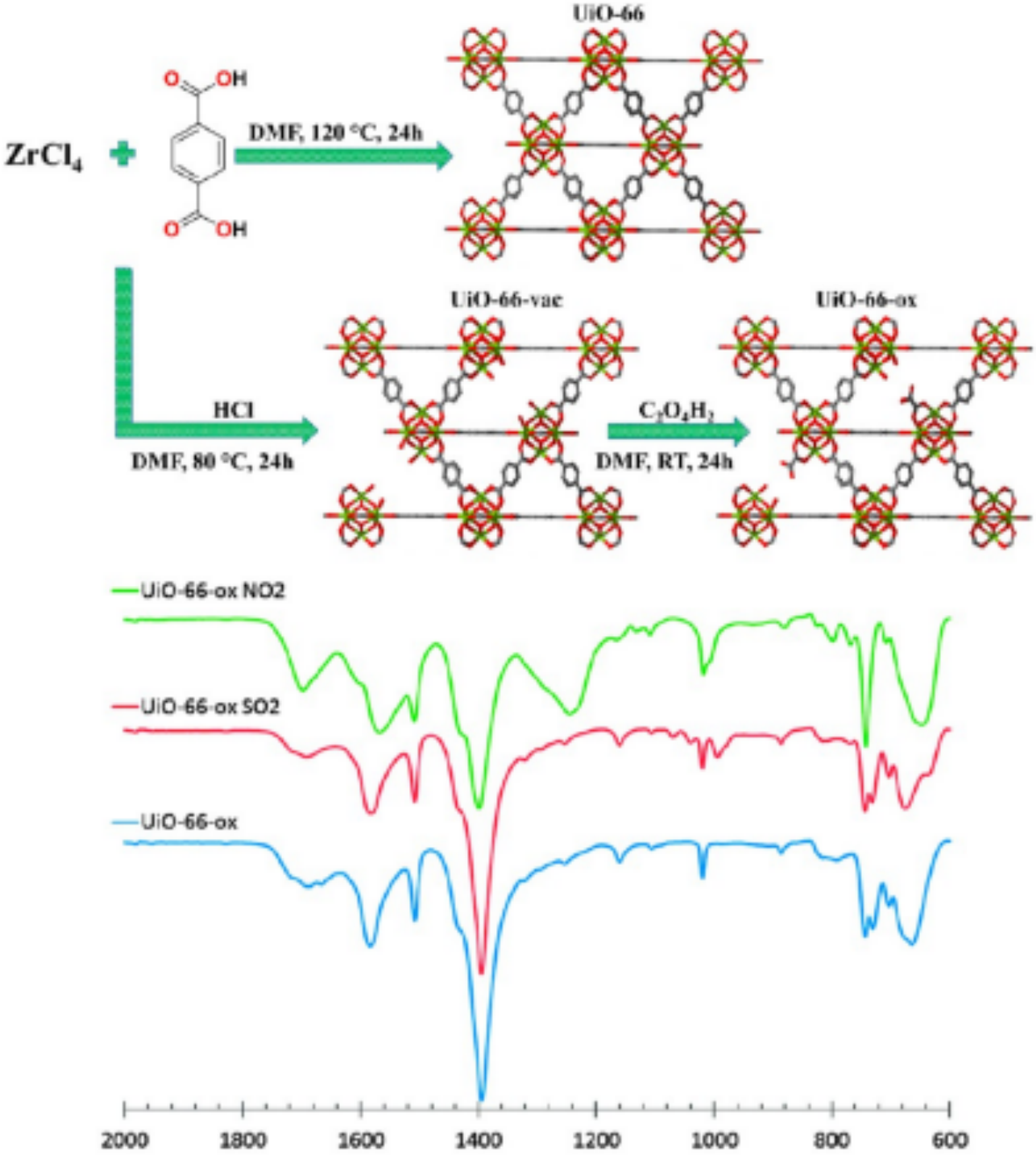
UiO-66
ZrCl4
DMF, 120 °C, 24h
UiO-66-vac
UiO-66-ox
HCl
DMF, 80 °C, 24h
C7O4H2
DMF, RT, 24h
UiO-66-ox NO2
UiO-66-ox SO2
UiO-66-ox
2000
1800
1600
1400
1200
1000
800
600

Figure 12.

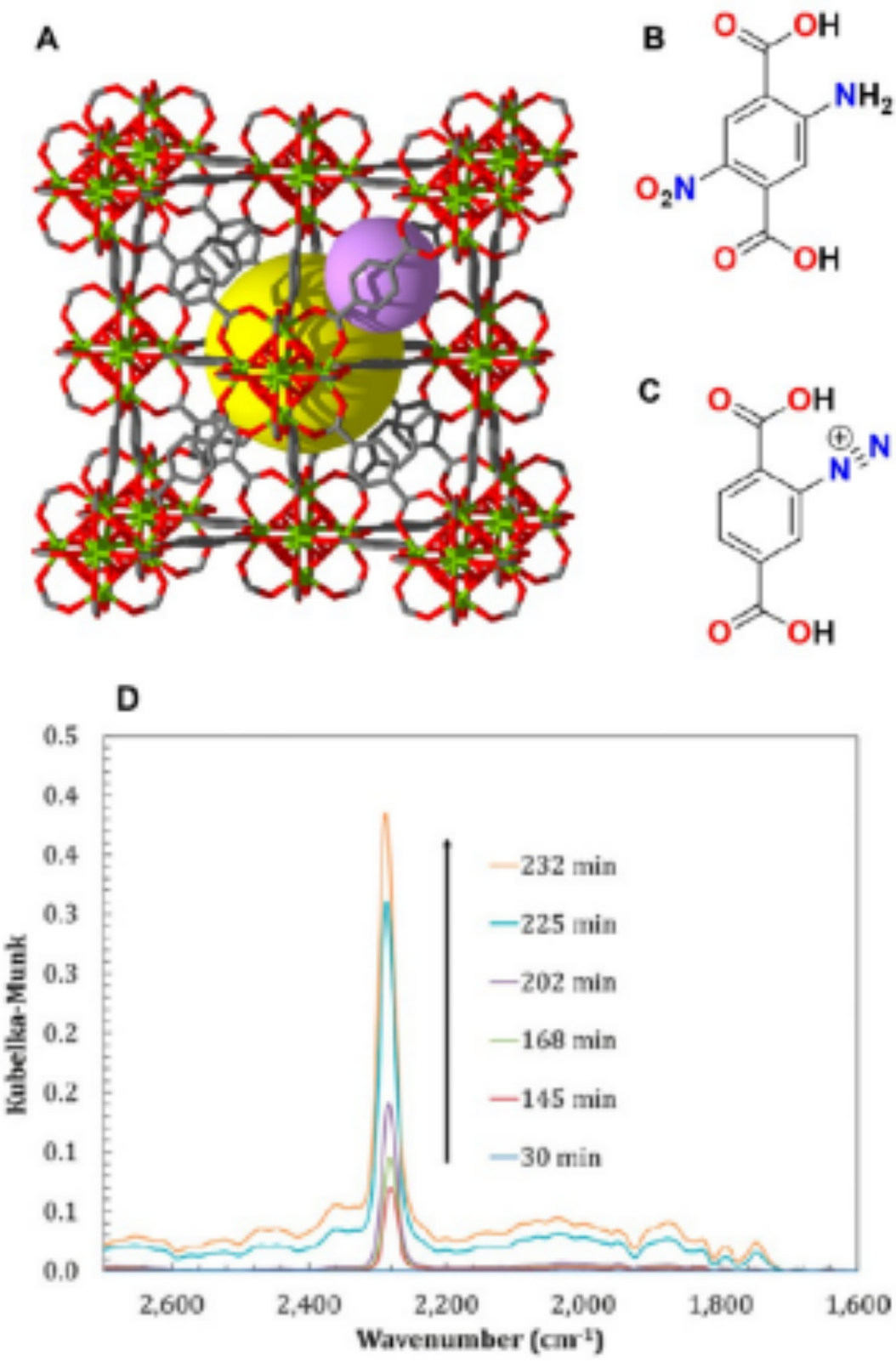
A
B
C
D
O
OH
NH2
O2N
N
Kubelka-Munk
0.5
0.4
0.4
0.3
0.3
0.2
0.2
0.1
0.1
0.0
232 min
225 min
202 min
168 min
145 min
30 min
2,600
2,400
2,200
2,000
1,800
1,600
Wavenumber (cm-1)

Figure 13.

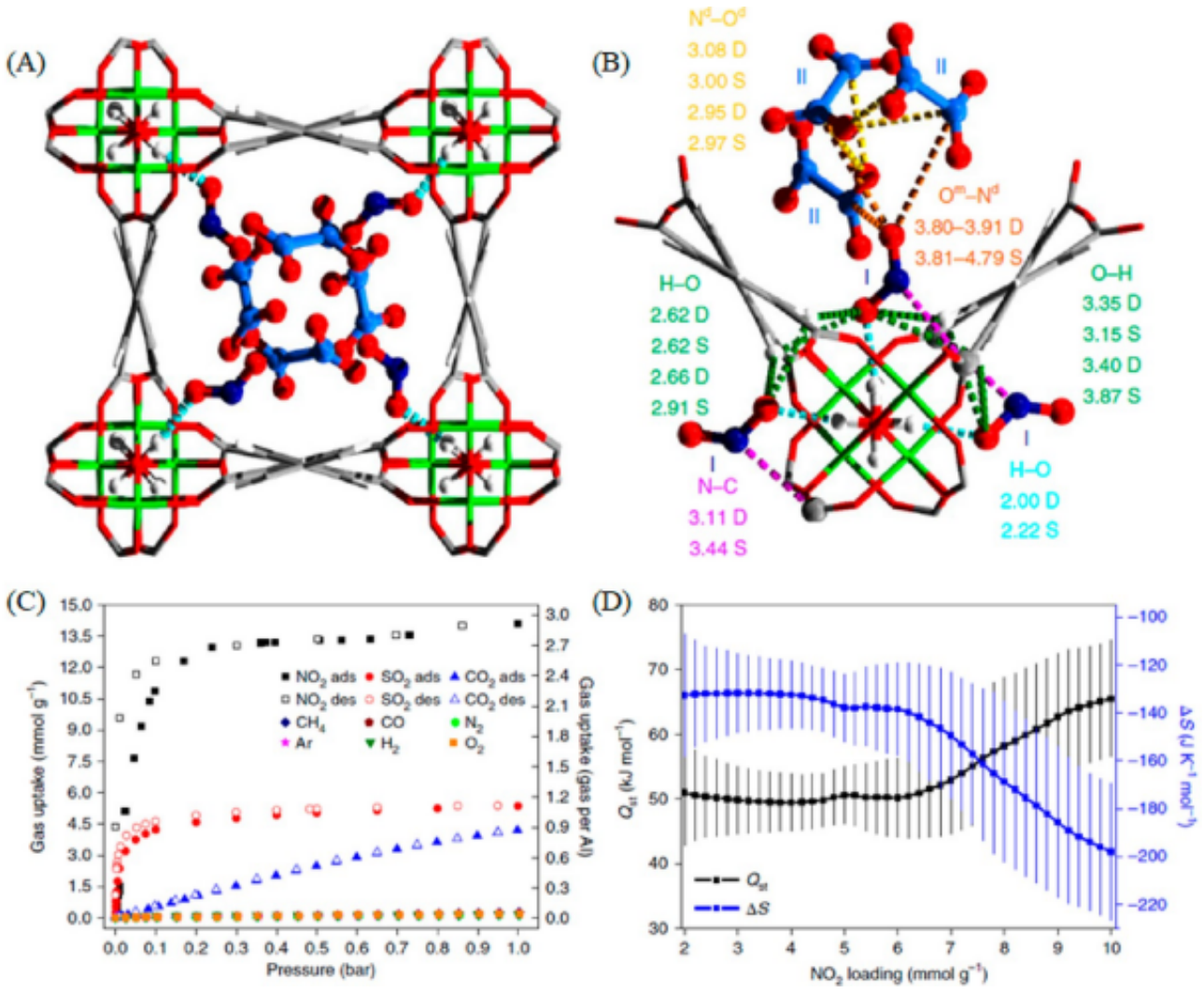
(A)
(B)
Nd–Od
3.08 D
3.00 S
2.95 D
2.97 S
Om–Nd
3.80–3.91 D
3.81–4.79 S
H–O
2.62 D
2.62 S
2.66 D
2.91 S
O–H
3.35 D
3.15 S
3.40 D
3.87 S
N–C
3.11 D
3.44 S
H–O
2.00 D
2.22 S
(C)
Gas uptake (mmol g−1)
Gas uptake (gas per Al)
Pressure (bar)
NO2 ads
NO2 des
SO2 ads
SO2 des
CO2 ads
CO2 des
CH4
CO
N2
Ar
H2
O2
(D)
Qst (kJ mol−1)
ΔS (J K−1 mol−1)
Qst
ΔS
NO2 loading (mmol g−1)

Figure 14.

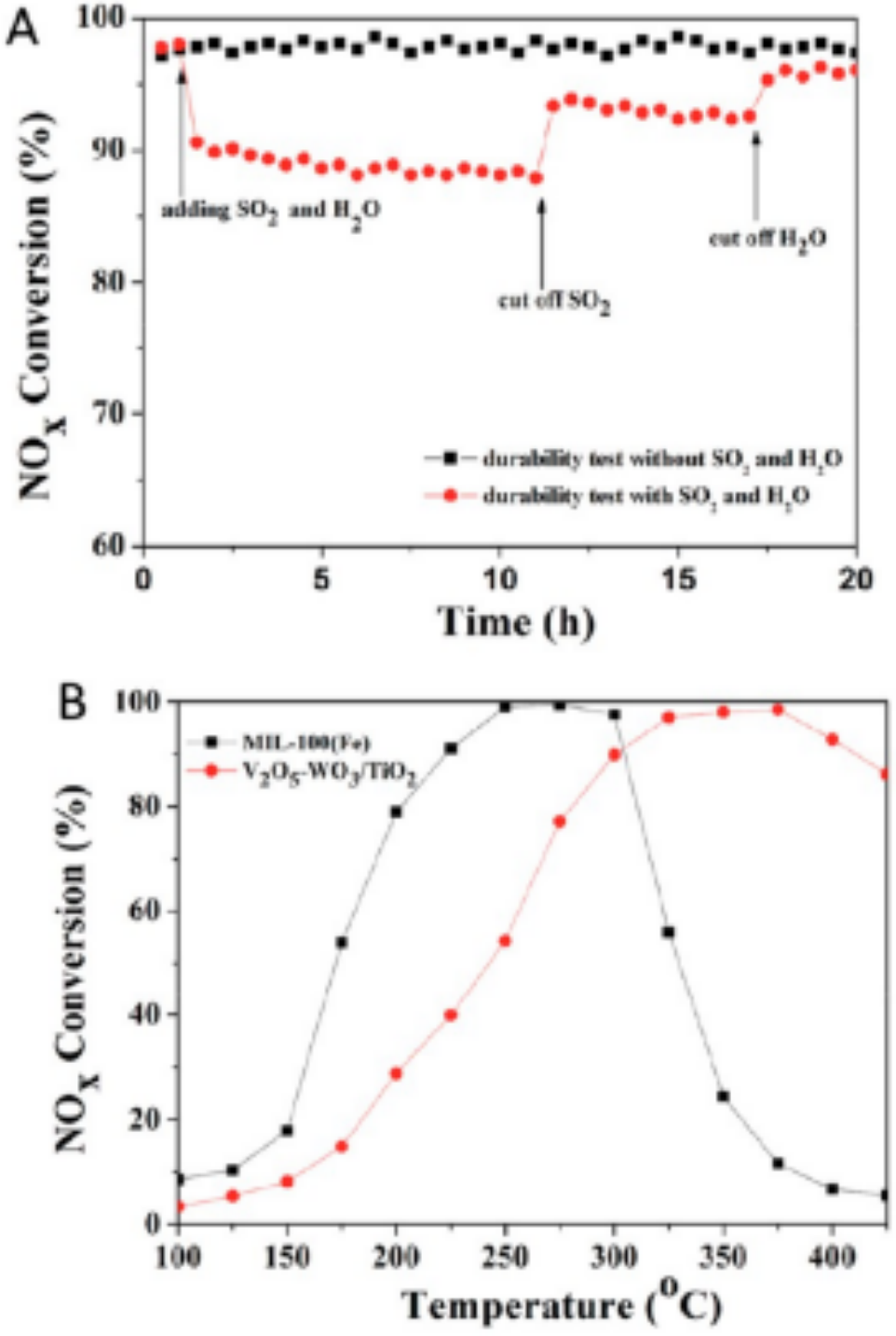
A
100
90
80
70
60
NO_x Conversion (%)
adding SO_2 and H_2O
cut off SO_2
cut off H_2O
durability test without SO_2 and H_2O
durability test with SO_2 and H_2O
0
5
10
15
20
Time (h)
B
100
80
60
40
20
0
NO_x Conversion (%)
MIL-100(Fe)
V_2O_5-WO_3/TiO_2
100
150
200
250
300
350
400
Temperature (^{0}C)

Figure 15.

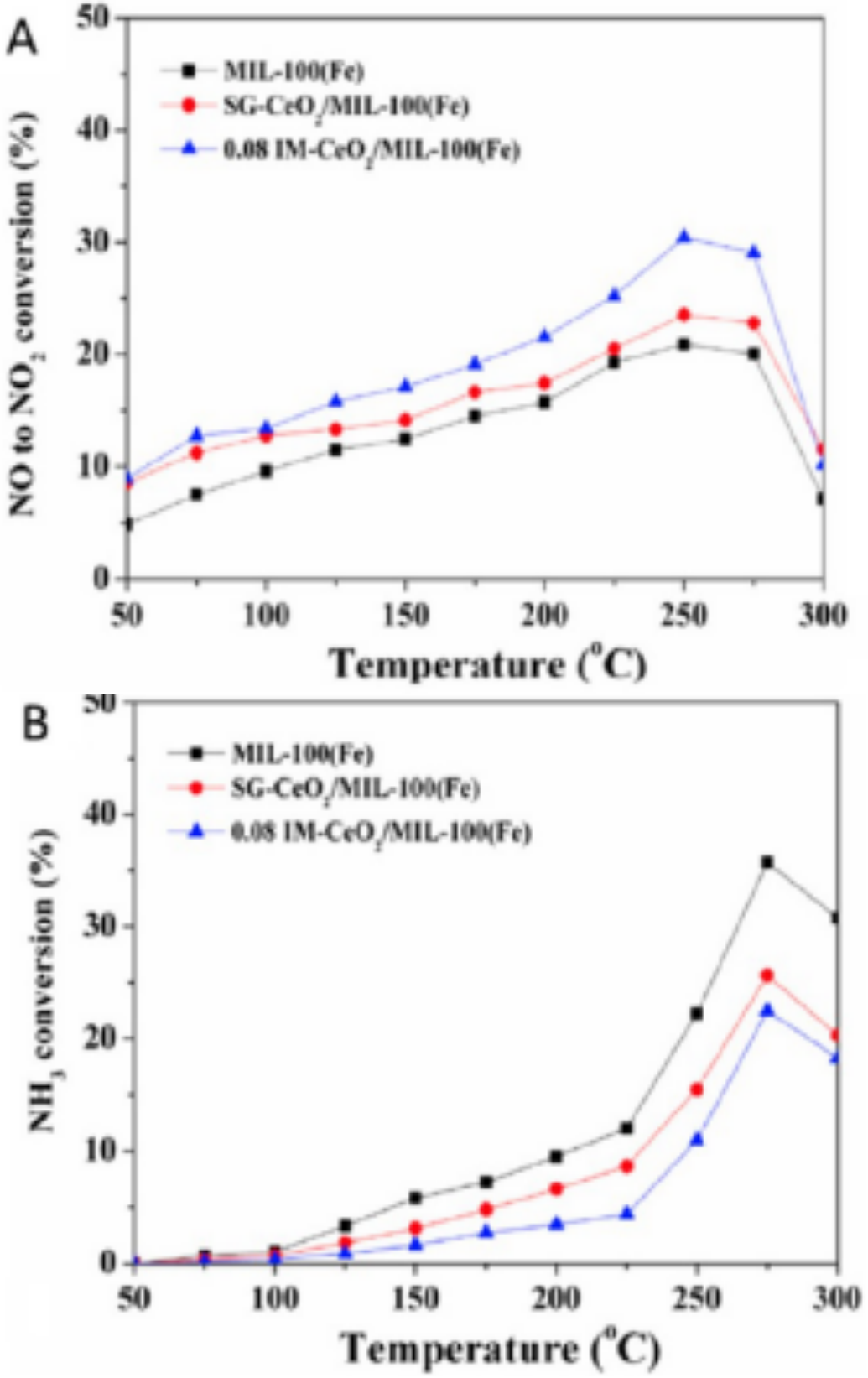
A
MIL-100(Fe)
SG-CeO2/MIL-100(Fe)
0.08 IM-CeO2/MIL-100(Fe)
NO to NO2 conversion (%)
Temperature (°C)
B
MIL-100(Fe)
SG-CeO2/MIL-100(Fe)
0.08 IM-CeO2/MIL-100(Fe)
NH3 conversion (%)
Temperature (°C)

Figure 16.

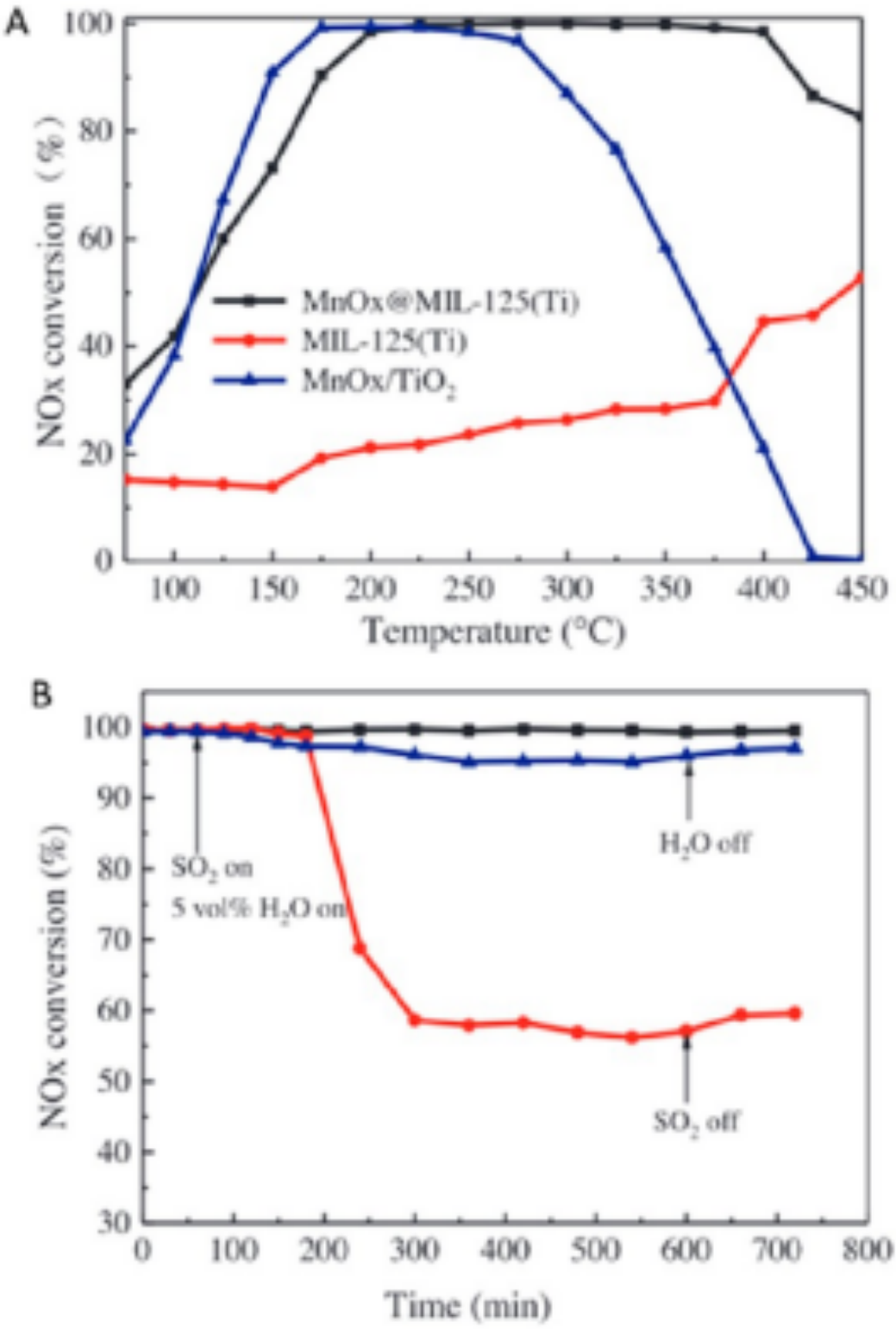
A
NOx conversion (%)
Temperature (°C)
MnOx@MIL-125(Ti)
MIL-125(Ti)
MnOx/TiO2
B
NOx conversion (%)
Time (min)
SO2 on
5 vol% H2O on
H2O off
SO2 off

Figure 17.

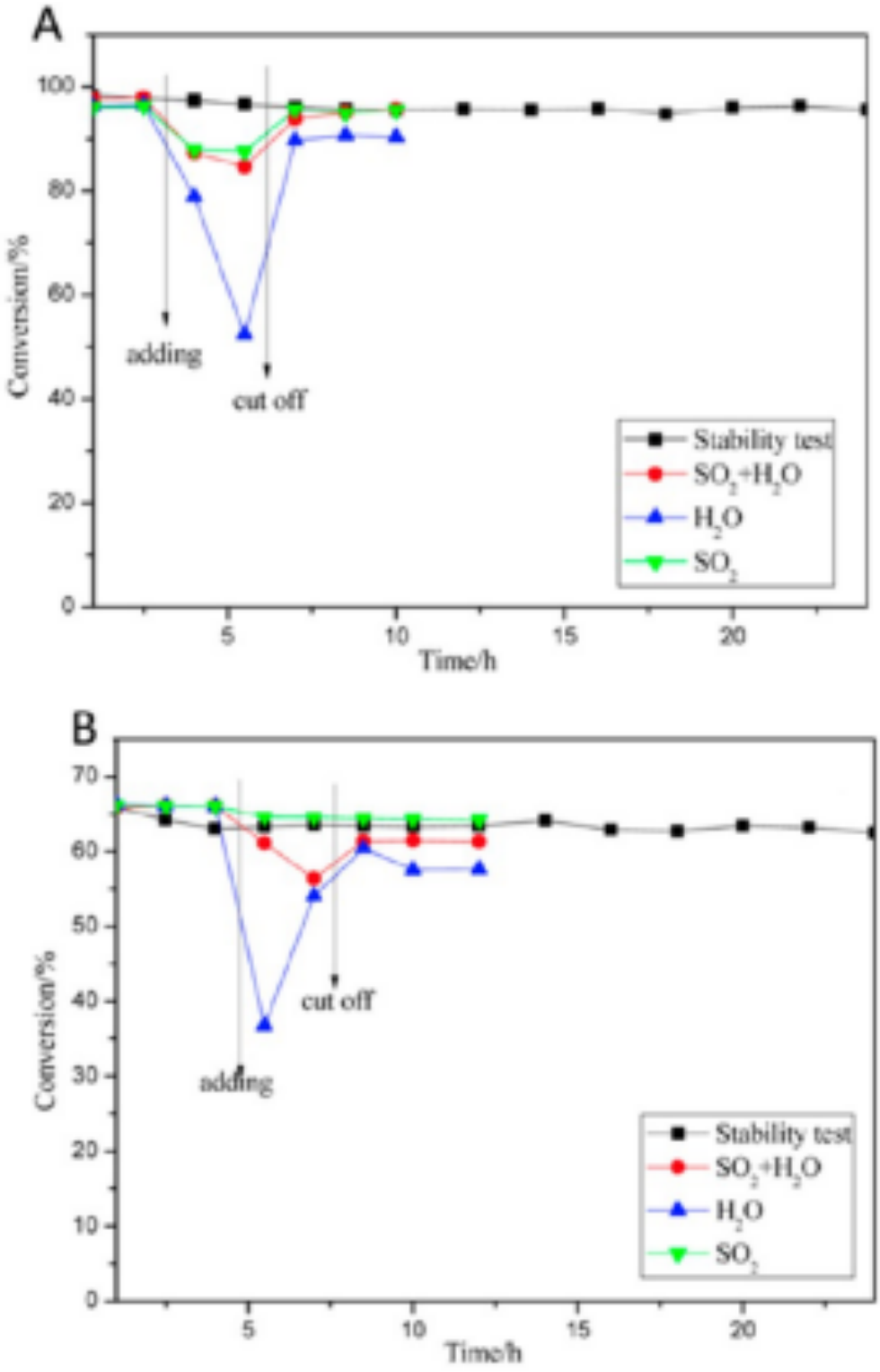
A
Conversion/%
Time/h
adding
cut off
Stability test
SO2+H2O
H2O
SO2
B
Conversion/%
Time/h
adding
cut off
Stability test
SO2+H2O
H2O
SO2

Figure 18.

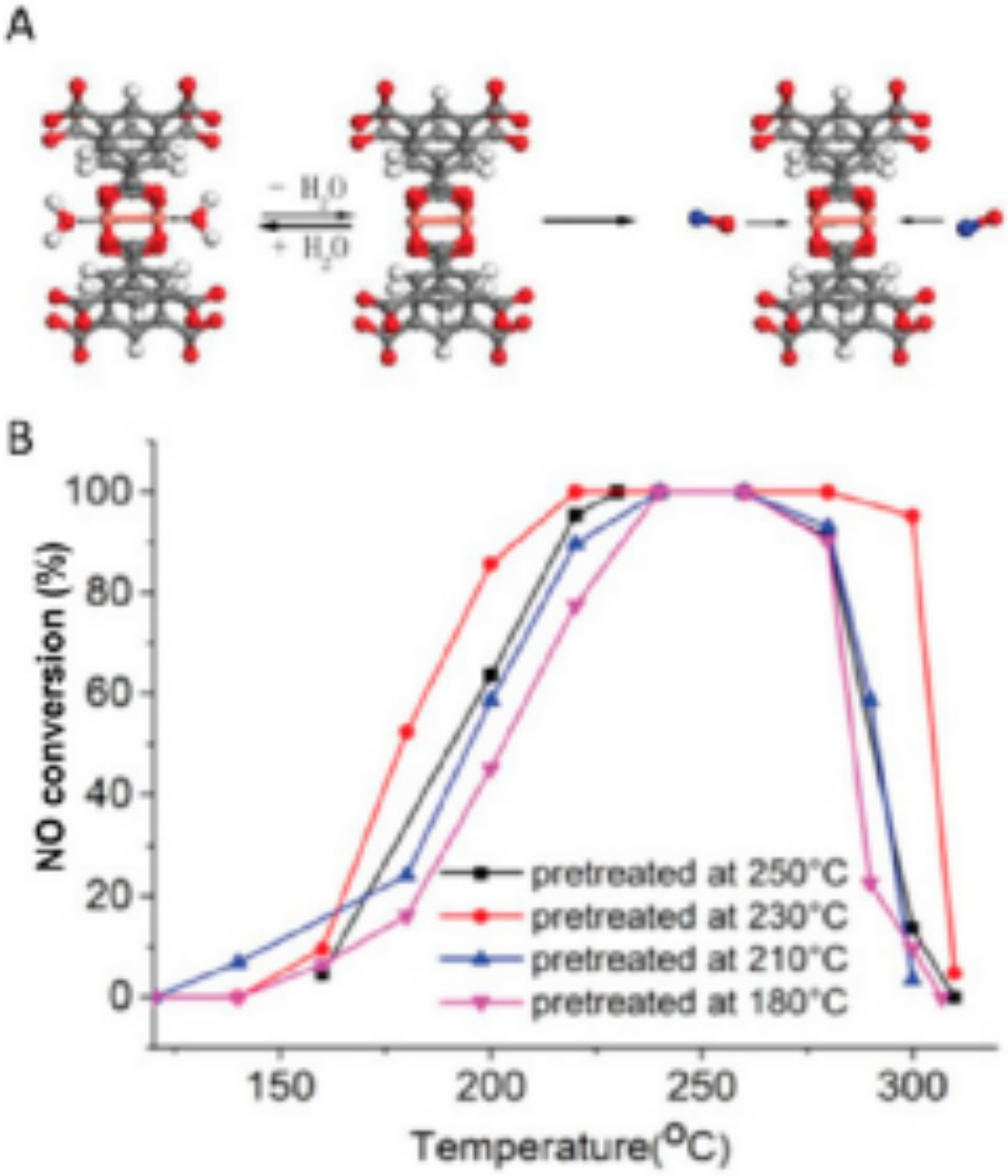
A
- H2O
+ H2O
B
NO conversion (%)
100
80
60
40
20
0
150
200
250
300
Temperature(°C)
pretreated at 250°C
pretreated at 230°C
pretreated at 210°C
pretreated at 180°C

Figure 19.

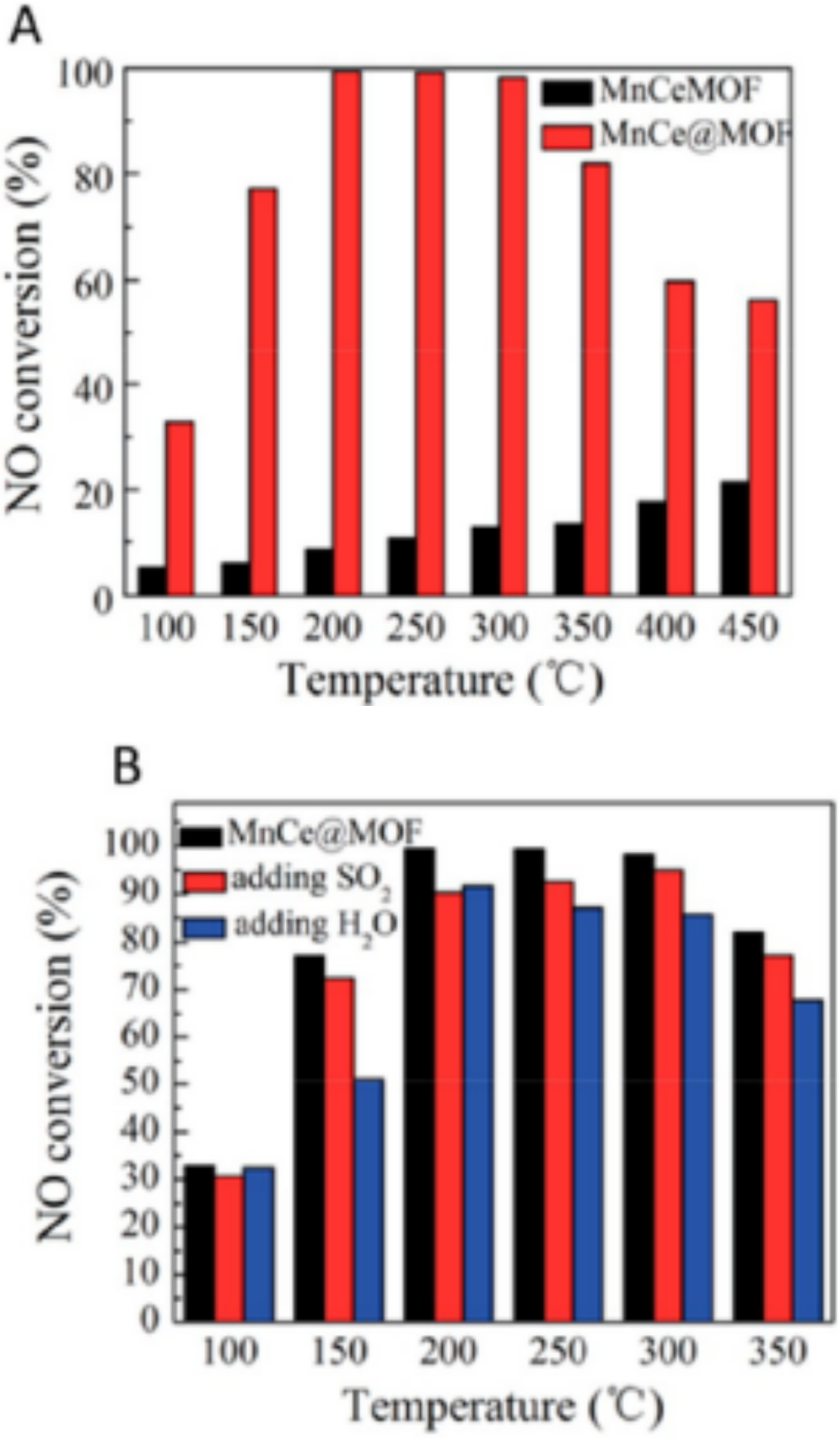
A
NO conversion (%)
100
80
60
40
20
0
MnCeMOF
MnCe@MOF
100 150 200 250 300 350 400 450
Temperature (℃)
B
NO conversion (%)
100
90
80
70
60
50
40
30
20
10
0
MnCe@MOF
adding SO2
adding H2O
100 150 200 250 300 350
Temperature (℃)

Figure 20.

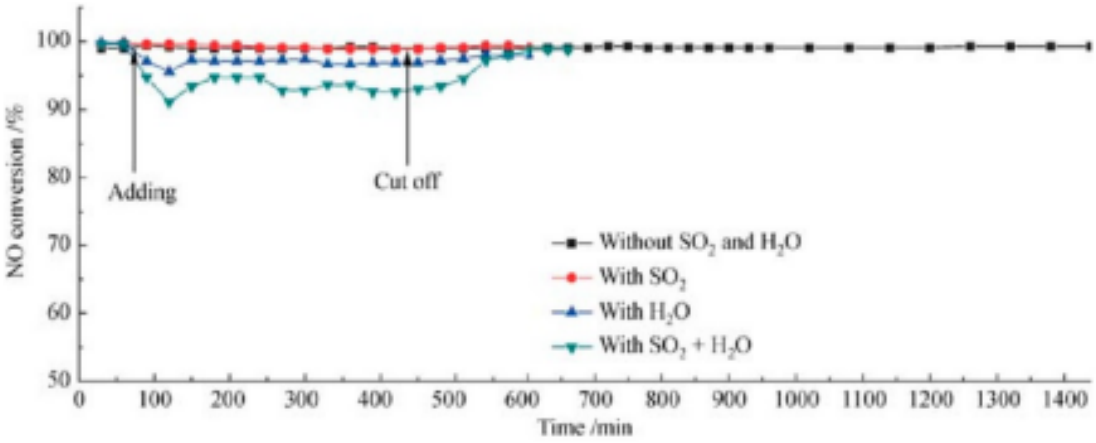
NO conversion /%
100
90
80
70
60
50
0
100
200
300
400
500
600
700
800
900
1000
1100
1200
1300
1400
Time /min
Adding
Cut off
Without SO_2 and H_2O
With SO_2
With H_2O
With SO_2 + H_2O

Figure 21.

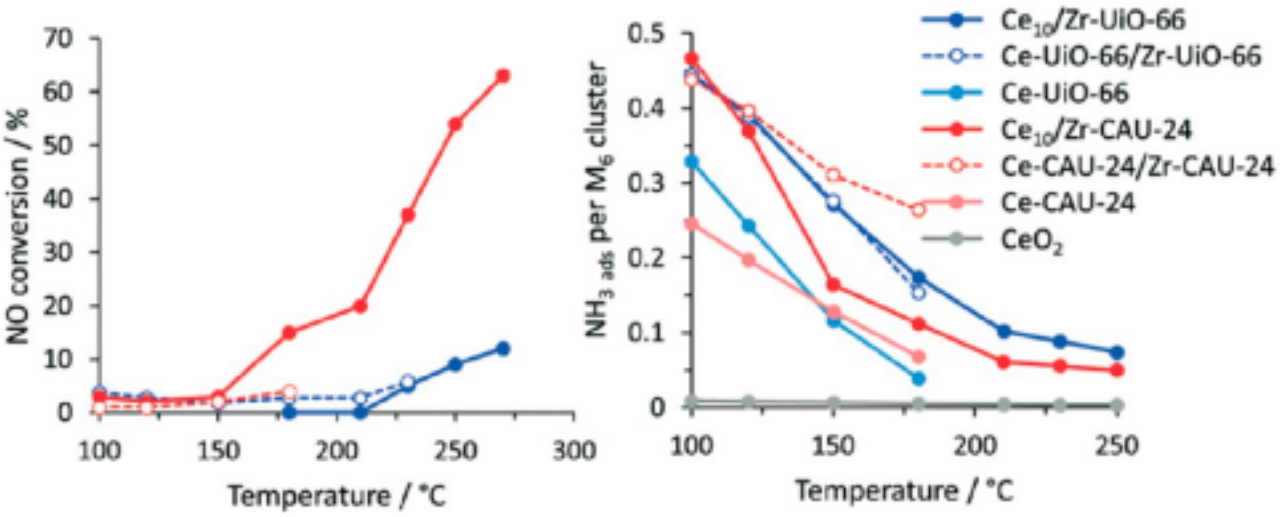
NO conversion / %
70
60
50
40
30
20
10
0
100
150
200
250
300
Temperature / °C
$NH_{3\ ads}$ per M_6 cluster
0.5
0.4
0.3
0.2
0.1
0
100
150
200
250
Temperature / °C
Ce_{10}/Zr-UiO-66
Ce-UiO-66/Zr-UiO-66
Ce-UiO-66
Ce_{10}/Zr-CAU-24
Ce-CAU-24/Zr-CAU-24
Ce-CAU-24
CeO_2

Figure 22.

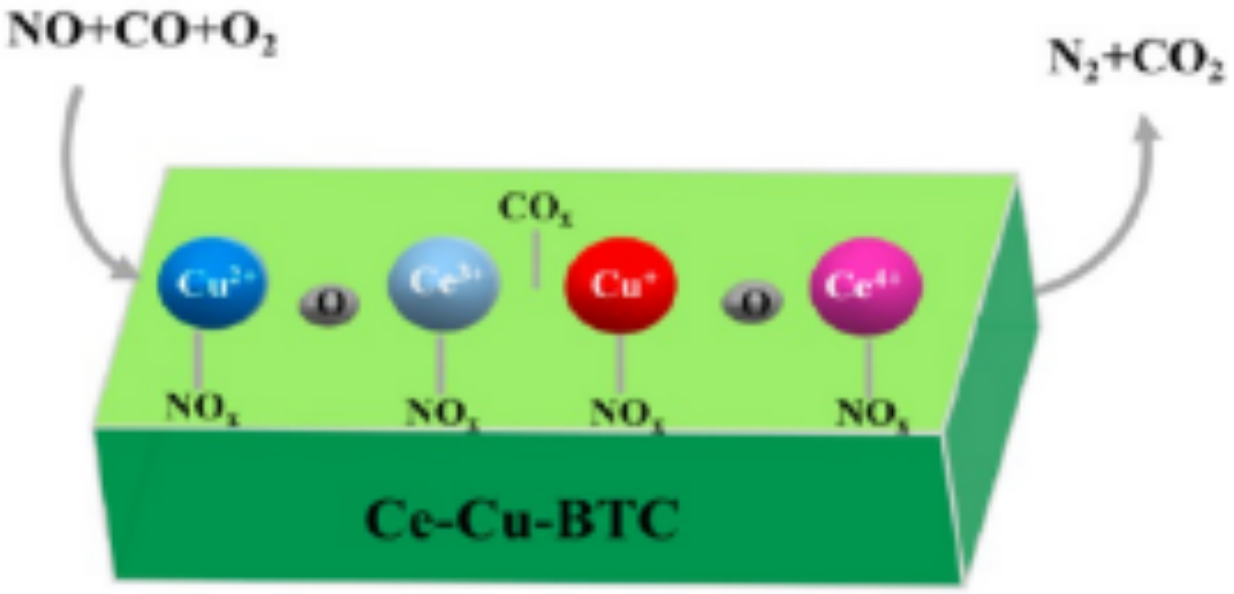

Figure 23.

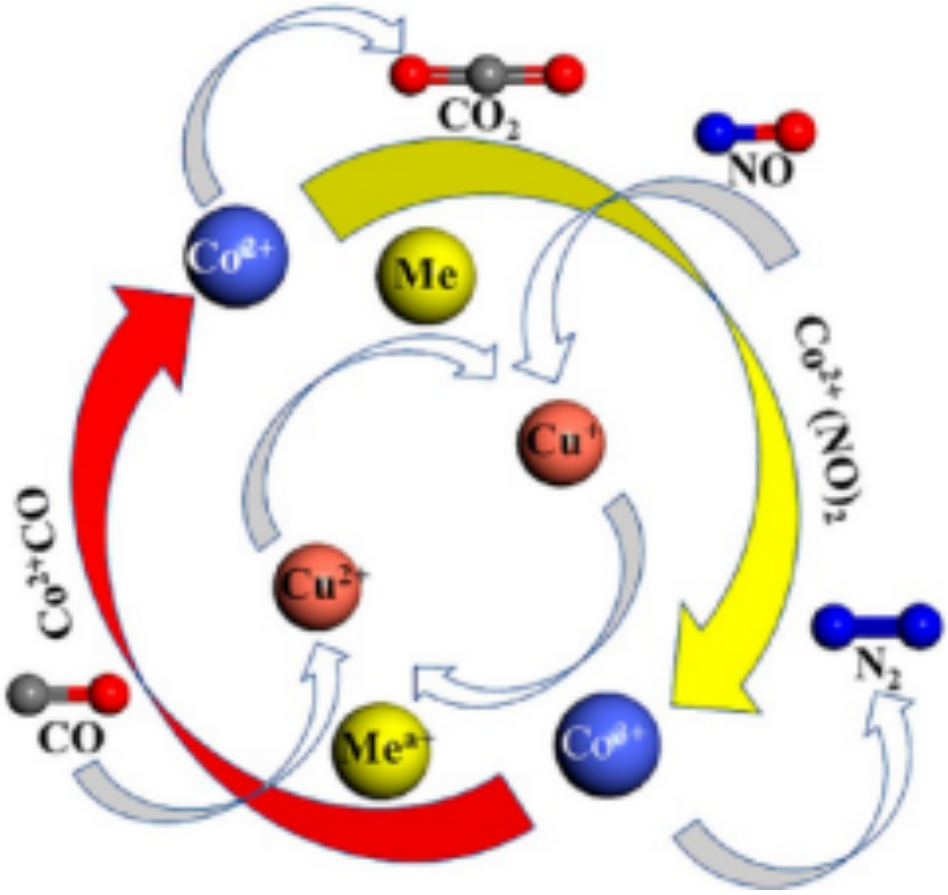

Figure 24

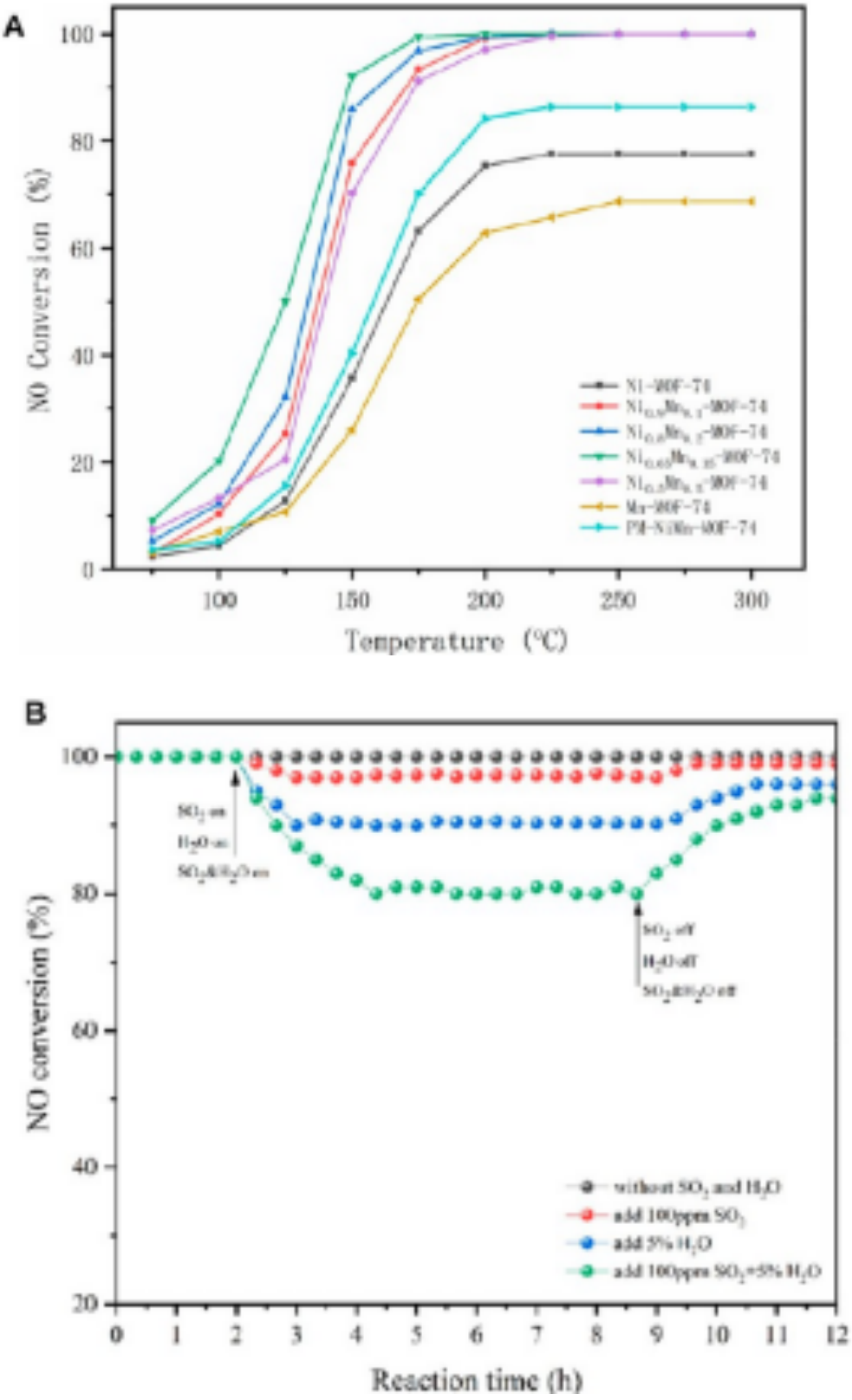
A
NO Conversion (%)
Temperature (℃)
B
NO conversion (%)
Reaction time (h)
without SO2 and H2O
add 100ppm SO2
add 5% H2O
add 100ppm SO2+5% H2O

Figure 25.

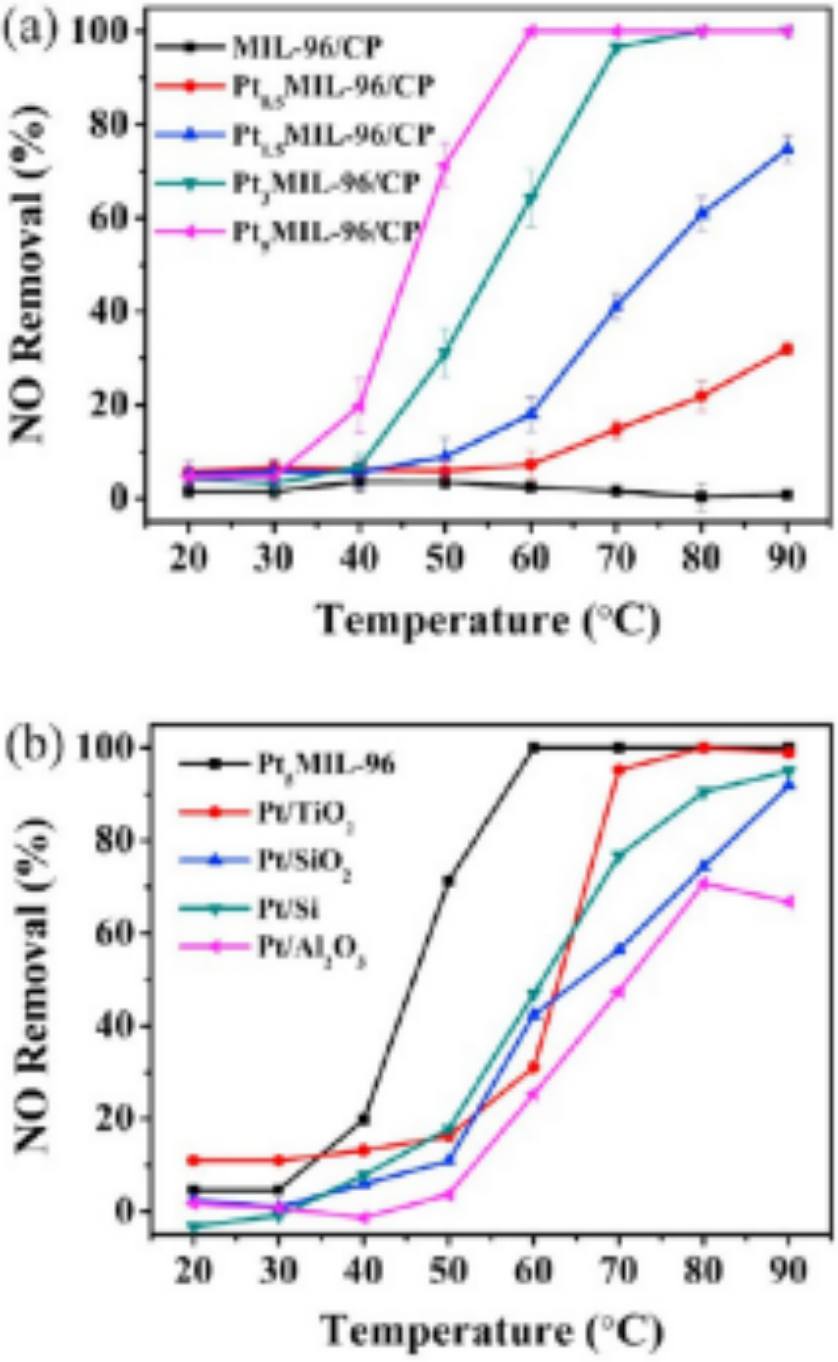
(a)
NO Removal (%)
Temperature (°C)
MIL-96/CP
Pt0.5MIL-96/CP
Pt1.5MIL-96/CP
Pt3MIL-96/CP
Pt9MIL-96/CP
(b)
NO Removal (%)
Temperature (°C)
Pt9MIL-96
Pt/TiO2
Pt/SiO2
Pt/Si
Pt/Al2O3

Figure 26.

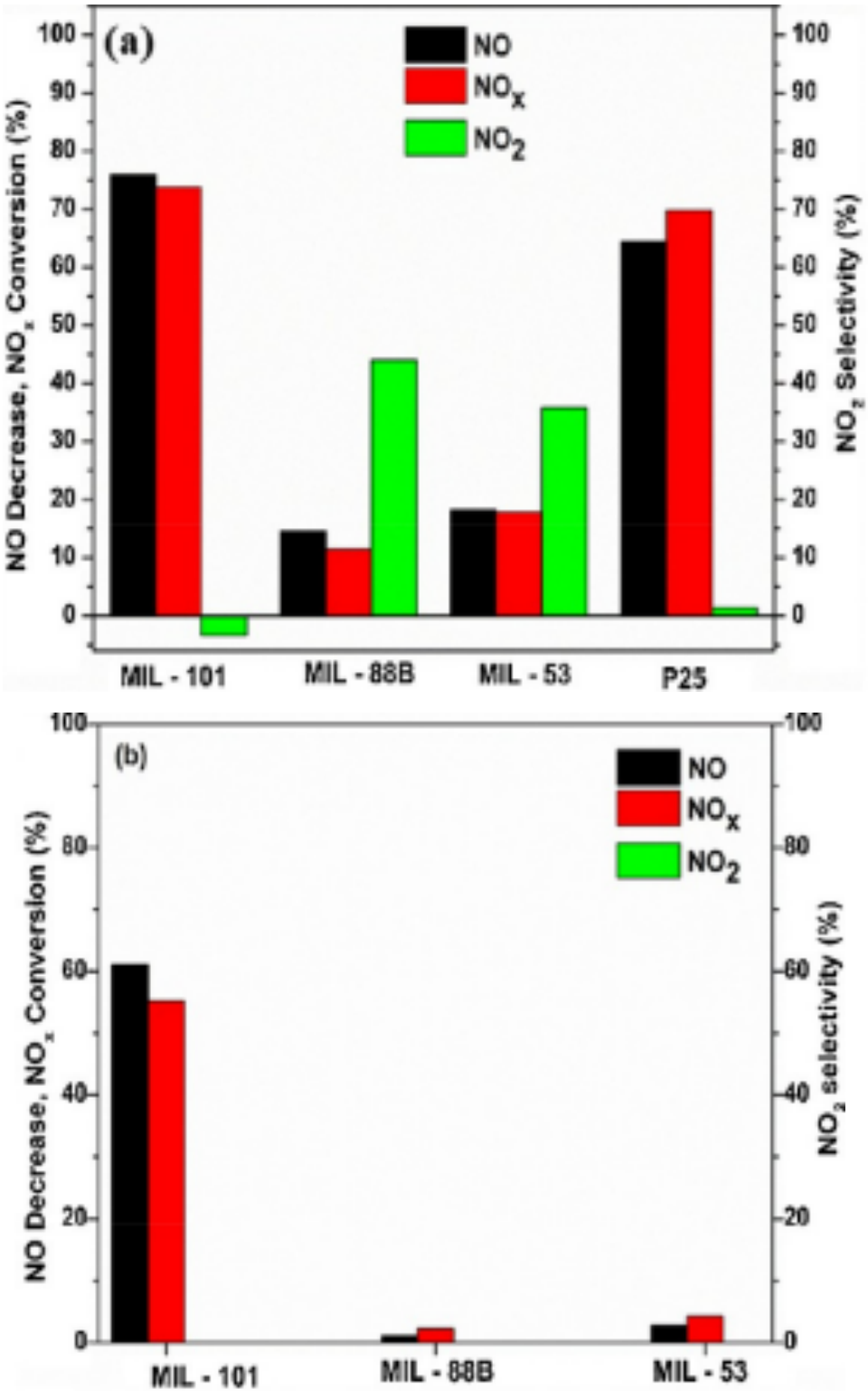
(a)
NO
NO$_x$
NO$_2$
NO Decrease, NO$_x$ Conversion (%)
NO$_2$ Selectivity (%)
MIL - 101
MIL - 88B
MIL - 53
P25
(b)
NO
NO$_x$
NO$_2$
NO Decrease, NO$_x$ Conversion (%)
NO$_2$ selectivity (%)
MIL - 101
MIL - 88B
MIL - 53

Figure 27.

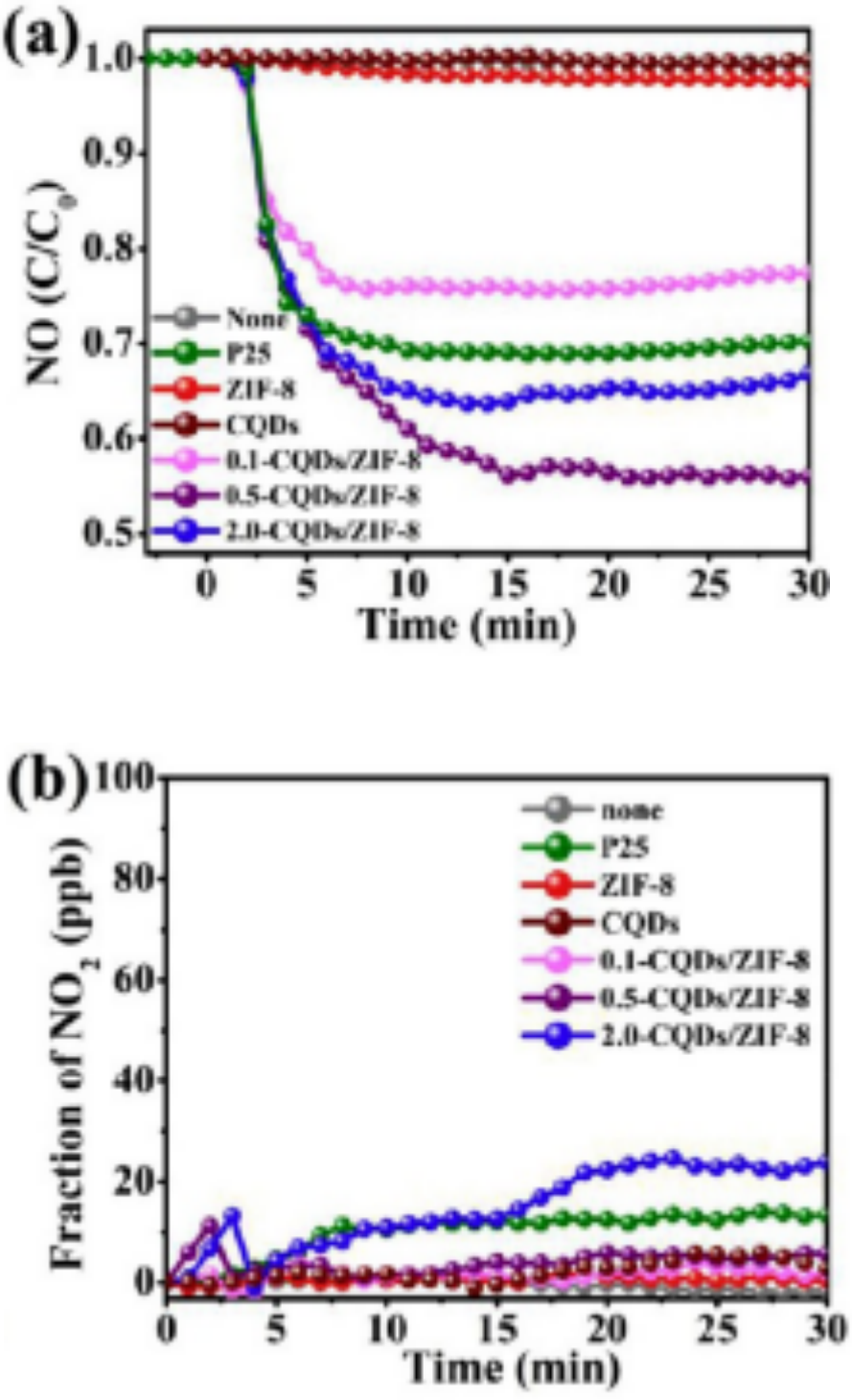
(a)
NO (C/C0)
1.0
0.9
0.8
0.7
0.6
0.5
None
P25
ZIF-8
CQDs
0.1-CQDs/ZIF-8
0.5-CQDs/ZIF-8
2.0-CQDs/ZIF-8
0
5
10
15
20
25
30
Time (min)
(b)
Fraction of NO2 (ppb)
100
80
60
40
20
0
none
P25
ZIF-8
CQDs
0.1-CQDs/ZIF-8
0.5-CQDs/ZIF-8
2.0-CQDs/ZIF-8
0
5
10
15
20
25
30
Time (min)

Figure 28.

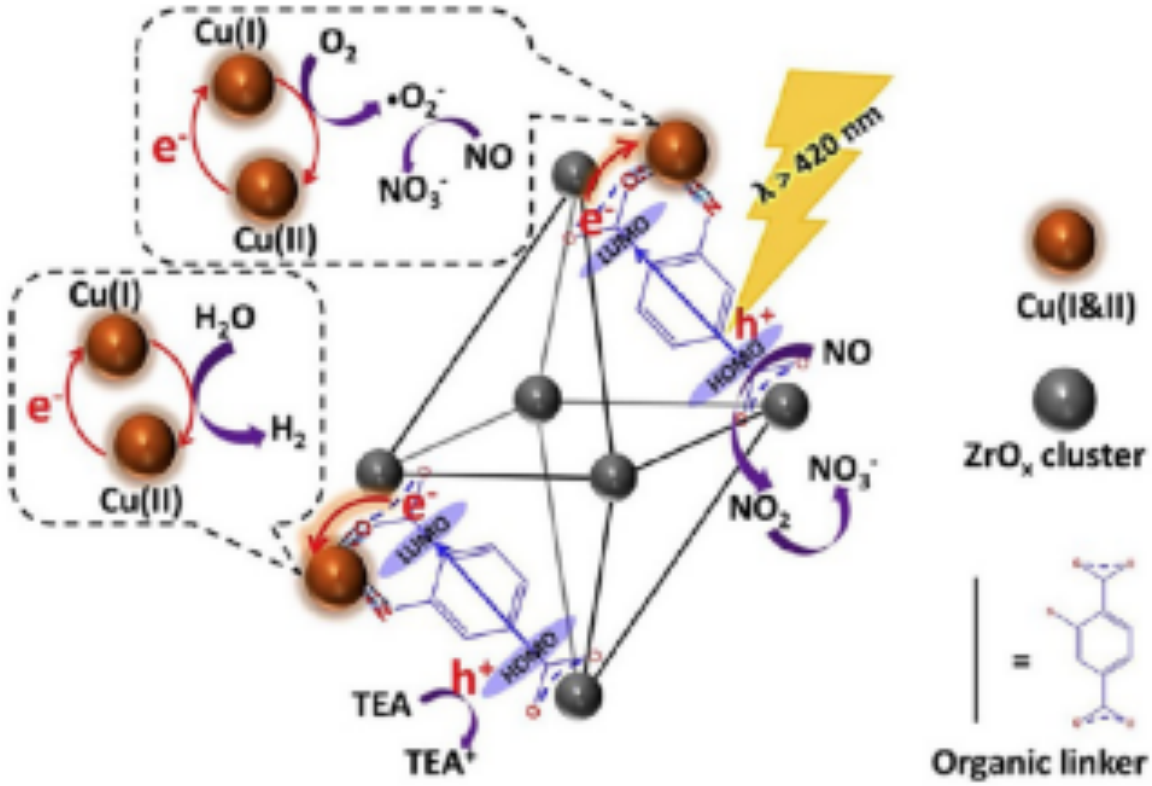
Cu(I)
O2
•O2-
NO
NO3-
e-
Cu(II)
Cu(I)
H2O
e-
H2
Cu(II)
λ > 420 nm
e-
LUMO
h+
HOMO
NO
NO3-
NO2
e-
LUMO
h+
HOMO
TEA
TEA+
Cu(I&II)
ZrOx cluster
=
Organic linker

Figure 29.